

# Behavior of the AB-type compounds at high pressures and high temperatures

Cite as: Journal of Physical and Chemical Reference Data **6**, 1205 (1977); <https://doi.org/10.1063/1.555565>  
Published Online: 15 October 2009

Leo Merrill



View Online



Export Citation

## ARTICLES YOU MAY BE INTERESTED IN

[Behavior of the AB<sub>2</sub>-Type Compounds at High Pressures and High Temperatures](#)

Journal of Physical and Chemical Reference Data **11**, 1005 (1982); <https://doi.org/10.1063/1.555670>

[Perspective: Crystal structure prediction at high pressures](#)

The Journal of Chemical Physics **140**, 040901 (2014); <https://doi.org/10.1063/1.4861966>

[Crystal structure prediction using ab initio evolutionary techniques: Principles and applications](#)

The Journal of Chemical Physics **124**, 244704 (2006); <https://doi.org/10.1063/1.2210932>



Where in the **world** is AIP Publishing?  
*Find out where we are exhibiting next*

# Behavior of the AB-Type Compounds at High Pressures and High Temperatures

Leo Merrill

*High Pressure Data Center, 5093 HBL, Brigham Young University, Provo, Utah 84602*

The results of the published work on the high pressure-high temperature properties of the AB-type compounds have been compiled and evaluated. All pressure studies above the range of 1 kilobar have been included with an emphasis on the accurate characterization of the solid-solid phase boundaries and the experimental melting curves. Whenever x-ray diffraction data are available for the high pressure phases, they have also been reviewed. Phase diagrams are included for all compounds in which measurement of more than one point along the phase boundary was made. This review discusses a total of 87 compounds and 212 distinct high pressure-high temperature phases.

Key words: AB-type compounds; calibration; critically evaluated data; crystallographic data; experimental melting curves; high pressure; solid-solid phase boundaries.

## Contents

	Page		Page
1. Introduction .....	1206	10.4. Thallium Iodide .....	1235
2. Lithium Halides .....	1224	11. Cyanides .....	1235
2.1. Lithium Chloride .....	1224	11.1. Cesium Cyanide .....	1236
3. Sodium Halides .....	1224	11.2. Gold Cyanide .....	1236
3.1. Sodium Fluoride .....	1224	11.3. Potassium Cyanide .....	1236
3.2. Sodium Chloride .....	1224	11.4. Potassium Thiocyanate .....	1237
3.3. Sodium Bromide .....	1224	11.5. Rubidium Cyanide .....	1237
3.4. Sodium Iodide .....	1224	11.6. Silver Cyanide .....	1237
4. Potassium Halides .....	1226	11.7. Sodium Cyanide .....	1237
4.1. Potassium Fluoride .....	1226	11.8. Sodium Thiocyanate .....	1237
4.2. Potassium Chloride .....	1226	12. Platinum Boride .....	1237
4.3. Potassium Bromide .....	1226	13. Carbides .....	1237
4.4. Potassium Iodide .....	1226	13.1. Molybdenum Carbide .....	1237
5. Rubidium Halides .....	1227	13.2. Rhenium Carbide .....	1239
6. Cesium Halides .....	1228	14. Boron Nitride .....	1239
6.1. Cesium Fluoride .....	1228	15. Phosphides .....	1239
6.2. Cesium Chloride .....	1228	15.1. Boron Phosphide .....	1239
7. Ammonium Halides .....	1228	15.2. Gallium Phosphide .....	1240
7.1. Ammonium Fluoride .....	1229	15.3. Germanium Phosphide .....	1240
7.2. Ammonium Chloride .....	1229	15.4. Indium Phosphide .....	1240
7.3. Ammonium Bromide .....	1230	15.5. Silicon Phosphide .....	1240
7.4. Ammonium Iodide .....	1230	15.6. Tin Phosphide .....	1240
8. Copper Halides .....	1230	16. Oxides .....	1241
8.1. Copper Chloride .....	1230	16.1. Barium Oxide .....	1241
8.2. Copper Bromide .....	1230	16.2. Europium Oxide .....	1241
8.3. Copper Iodide .....	1231	16.3. Iron Oxide .....	1241
9. Silver Halides .....	1232	16.4. Sodium Hydroxide .....	1241
9.1. Silver Fluoride .....	1233	16.5. Strontium Oxide .....	1241
9.2. Silver Chloride .....	1233	16.6. Tin Oxide .....	1242
9.3. Silver Bromide .....	1233	16.7. Zinc Oxide .....	1242
9.4. Silver Iodide .....	1233	17. Sulfides .....	1242
10. Thallium Halides .....	1234	17.1. Cadmium Sulfide .....	1242
10.1. Thallium Fluoride .....	1234	17.2. Iron Sulfide .....	1243
10.2. Thallium Chloride .....	1234	17.3. Lead Sulfide .....	1243
10.3. Thallium Bromide .....	1235	17.4. Mercury Sulfide .....	1243
		17.5. Nickel Sulfide .....	1243
		17.6. Samarium Sulfide .....	1244
		17.7. Zinc Sulfide .....	1244

	Page
18. Antimonides . . . . .	1244
18.1. Gallium Antimonide/Aluminum Antimonide . . . . .	1244
18.2. Indium Antimonide . . . . .	1244
19. Arsenides . . . . .	1245
19.1. Boron Arsenide . . . . .	1245
19.2. Gallium Arsenide/Indium Arsenide . . . . .	1245
19.3. Germanium Arsenide . . . . .	1245
19.4. Manganese Arsenide . . . . .	1245
20. Selenides . . . . .	1245
20.1. Cadmium Selenide . . . . .	1245
20.2. Indium Selenide . . . . .	1246
20.3. Lead Selenide . . . . .	1246
20.4. Manganese Selenide . . . . .	1246
20.5. Mercury Selenide . . . . .	1247
20.6. Zinc Selenide . . . . .	1247
21. Tellurides . . . . .	1247
21.1. Cadmium Telluride . . . . .	1247
21.2. Europium Telluride . . . . .	1247
21.3. Germanium Telluride . . . . .	1248
21.4. Indium Telluride . . . . .	1248
21.5. Lead Telluride . . . . .	1249
21.6. Mercury Telluride . . . . .	1249
21.7. Praseodymium Telluride . . . . .	1249
21.8. Samarium Telluride . . . . .	1249
21.9. Tin Telluride . . . . .	1249
21.10. Ytterbium Telluride . . . . .	1249
21.11. Zinc Telluride . . . . .	1250
22. References . . . . .	1250

### List of Tables and Figures

	Page
Tables	
1. Pressure Fixed Points . . . . .	1207
2. Crystallographic Data . . . . .	1209
Figures	
1. Melting Curve for Lithium Chloride . . . . .	1224
2. Melting Curve for Sodium Fluoride . . . . .	1225
3. Partial Phase Diagram for Sodium Chloride . . . . .	1225

### Figures

	Page
4. Melting Curve for Sodium Bromide . . . . .	1225
5. Melting Curve for Sodium Iodide . . . . .	1225
6. Phase Diagram for Potassium Chloride . . . . .	1226
7. Partial Phase Diagram for Potassium Iodide . . . . .	1226
8. Phase Diagram for Rubidium Fluoride . . . . .	1227
9. Phase Diagram for Rubidium Chloride . . . . .	1227
10. Phase Diagram for Rubidium Bromide . . . . .	1227
11. Phase Diagram for Rubidium Iodide . . . . .	1228
12. Phase Diagram for Ammonium Fluoride . . . . .	1229
13. Phase Diagram for Ammonium Chloride . . . . .	1229
14. Phase Diagram for Ammonium Bromide . . . . .	1230
15. Phase Diagram for Ammonium Iodide . . . . .	1230
16. Phase Diagram for Copper Chloride . . . . .	1231
17. Phase Diagram for Copper Bromide . . . . .	1231
18. Phase Diagram for Copper Iodide . . . . .	1232
19. Melting Curve for Silver Chloride . . . . .	1233
20. Melting Curve for Silver Bromide . . . . .	1234
21. Phase Diagram for Silver Iodide . . . . .	1234
22. Phase Diagram for Thallium Fluoride . . . . .	1235
23. Melting Curve for Thallium Chloride . . . . .	1235
24. Melting Curve for Thallium Bromide . . . . .	1235
25. Phase Diagram for Thallium Iodide . . . . .	1236
26. Phase Diagram for Potassium Cyanide . . . . .	1236
27. Phase Diagram for Potassium Thiocyanate . . . . .	1237
28. Partial Phase Diagram for Rubidium Cyanide . . . . .	1238
29. Phase Diagram for Silver Cyanide . . . . .	1238
30. Phase Diagram for Sodium Cyanide . . . . .	1238
31. Phase Diagram for Sodium Thiocyanate . . . . .	1238
32. Phase Diagram for Boron Nitride . . . . .	1239
33. Phase Diagram for Sodium Hydroxide . . . . .	1242
34. Partial Phase Diagram for Zinc Oxide . . . . .	1242
35. Partial Phase Diagram for Iron Sulfide . . . . .	1243
36. Partial Phase Diagram for Nickel Sulfide . . . . .	1243
37. Phase Diagram for Indium Antimonide . . . . .	1244
38. Partial Phase Diagram for Manganese Arsenide . . . . .	1246
39. Partial Phase Diagram for Cadmium Selenide . . . . .	1246
40. Partial Phase Diagram for Mercury Selenide and Mercury Telluride . . . . .	1247
41. Partial Phase Diagram for Cadmium Telluride . . . . .	1248
42. Phase Diagram for Indium Telluride . . . . .	1248

## 1. Introduction

This is the second in a series of papers on the subject of the behavior of materials at high pressure. In a previous paper [41]<sup>1</sup>, data on polymorphic phase changes and melting curves have been compiled and evaluated for the elements. This review is a continuation of that effort, and deals with the AB-type compounds. The types of data included are mainly the thermodynamic parameters of the solid-solid phase boundaries and melting curves. In most of the studies of the high pressure phases of the AB-type compounds, x-ray diffraction experiments have been conducted. The results of these investigations are tabulated and discussed.

<sup>1</sup> Figures in brackets indicate literature references.

Since all measurements of material properties are ultimately tied to a pressure scale, it is necessary to review the status of pressure calibration in terms of techniques and the uncertainties associated with each technique. In any branch of metrology, calibration techniques are always based upon a primary scale which is defined in terms of first principles. Generally, it is not convenient to use the primary scale in actual measurement situations. For example, in the development of the temperature scale, it was decided to represent the primary thermodynamic scale as closely as possible, on the basis of reproducible equilibrium temperature fixed points [54]. The fixed points on the temperature scale are now designated as defining fixed points, and are considered exact by definition. In order to have a continuous scale, it is necessary to specify means for interpolating between fixed points.

Often, it is necessary to make measurements beyond the operational range of the primary scale, so it is also useful to specify extrapolation techniques, and justify their validity [55].

In pressure measurements, a primary scale can be defined on the basis of force/unit area. Since pressure comparisons require uniformity of pressure throughout the system, the primary scale must be based on a truly hydrostatic system. Two basic measuring systems with a variety of modifications have been used rather widely as a basis for a primary pressure scale: (a) the mercury manometer, and (b) the free piston gage. In a practical sense, the use of the mercury manometer has been limited to pressures of a few hundred bars while the free piston gage is commonly used to 10 kilobars, and has been used successfully to 26 kilobars [55], but corrections are much more severe in this latter range.

The pressure dependence of the electrical resistivity of manganin wire has been calibrated against the free piston gage for use as a secondary standard, and both a calibration and extrapolation device. Fixed calibration points such as the freezing point of mercury at 0 °C and the Bi I-II transition pressure have also been calibrated against the free piston gage. The upper limit of this scale is 26 kilobars.

The use of a piston-cylinder system with a solid medium pressure environment represents the best approximation to a primary pressure scale above 25 kilobars. Two dominant effects are of significance, first friction between the piston and cylinder, and second, the internal friction associated with the solid medium environment. Another source of error in calculating the pressure is the determination of the effective area of the piston face, which changes with pressure. Using the piston cylinder apparatus, the Ba I-II [79] and Bi III-IV [80] transition pressures have been determined at 55 and 77 kilobars, respectively. Uncertainties in pressures in this range are about one to two percent, and are comparable with that of extrapolation techniques. The present limit of this technique is approximately 80 kilobars.

Table 1 includes the presently accepted best values for the fixed transition points [54] for the various calibration materials up to the 130 kbar region. All of these points have been tied to the empirical NaCl equation of state. There are additional points in the literature [63], but it is felt that there are still insufficient intercomparisons to warrant their acceptance as fixed points, at the present time.

TABLE 1. Pressure fixed points

Transition	Pressure at RT	Ref.
Hg (L-I)	7.57 (0 °C)	55
Hg(L-I)	12.55 (25 °C)	54
Bi(I-II)	25.5	55
Tl(I-II)	36.7	55
Ba(I-II)	55.3	55
Bi(III-V)	76.7	55

Since most of the high pressure work above 10 kilobars involves a solid pressure transmitting medium, it would be desirable to define a primary pressure scale applicable to this method and pressure range. This can be accomplished by use of the thermodynamic definition of pressure

$$P = -\frac{\partial F}{\partial V_T}$$

In this definition, it is assumed that the deviatoric stress is zero and the deformation is pure dilation. The problem with this method, however, is that we don't know enough about the forces between the atoms of any substance to analytically define the Helmholtz Energy  $F = E - TS$ . As a consequence, we are able to define an equation of state by fitting it to experimental data, but we do not have a primary scale. This technique has been very successful, especially in its use with NaCl [54] to define an empirical equation of state. The NaCl equation of state serves as a convenient interpolation and extrapolation equation where pressure is defined as a continuous function of the lattice parameter  $a_{NaCl}$ . This empirical equation of state is tied to the free piston calibration at the mercury point and the Bi I-II point. Its accuracy is approximately one percent up to 50 kilobars and two percent above. The NaCl equation of state has been widely used with various types of multi-anvil and uniaxial devices, such as the tetrahedral press and Bridgman or diamond anvil, which have been adapted for x-ray or neutron diffraction analysis. It has served as an important unifying factor in high pressure calibration, making possible intercomparisons of different scales.

One of the early problems with pressure calibration procedures was that the pressure scale and fixed points above 60 kilobars were defined by extrapolation techniques with very large uncertainties. This suggests that there should be some criteria for selecting a good extrapolation technique, and also a stated range of validity. As a general rule, extrapolation equations should be based upon some physical or thermodynamic parameter which is continuously measurable as a function of pressure.

Since we are discussing calibration techniques applicable to solid pressure transmitting systems, it is necessary that the measured parameter not be sensitive to physical deformation of the sample on a macroscopic level or nonhydrostatic stresses on a microscopic level. This rules out all parameters related to transport properties, including electrical resistance. The acceptable parameters for extrapolation equations are those which are independent of the size and shape of the system being studied, i.e. the intensive parameters of the system. This would include measurements of molar volume, chemical potential, the lattice constant of NaCl, and the wavelength of the ruby R-line.

The NaCl equation of state was the first such extrapolation scale and has played an important role in defining a working

scale up to 300 kilobars. Another very useful scale is the ruby R-line-fluorescence method [13], which is of very recent development. The frequency shift of the ruby R-line has been calibrated to the NaCl equation of state and serves as a very quick and convenient calibration technique which is apparently linear with pressure up to 290 kbars.

In this region the  $P$  vs.  $\Delta\lambda$  relation is given by  $P_{NaCl} = 1.328(\Delta\lambda) + 0.0003(\Delta\lambda)^2$ . Due to the magnitude of the uncertainties in the coefficient of the linear term, the small quadratic coefficient is undetectable and nonlinearity is masked because of the errors involved [151,152].

The accepted SI unit of pressure is the Pascal (Newton/meter<sup>2</sup>). Since the bar (10<sup>5</sup> Pascal) has been used almost ex-

clusively in the high pressure literature as the unit of pressure, the units 'bar' and 'kbar' have been used in this report. For ease of converting to GPa (giga Pascal) from kbar use the following relation:

$$1 \text{ GPa} = 10 \text{ kbar.}$$

#### Explanation of Symbols in Table II

- \* Crystal structure not known.
- \*\* X-ray diffraction pattern could not be indexed.
- N Atmospheric pressure.
- R Room temperature.

Table II

## CRYSTALLOGRAPHIC DATA

COMPOUND	Pressure (kbar)	Temperature (°C)	Crystal System	Structure Type	a (Å)	b (Å)	c (Å)	Angle (°)	Z	Space Group	Density (g/cm <sup>3</sup> )	Ref.
<u>Halides</u>												
AgBr(I)	N	R	Cubic	NaCl	5.7745				4	Fm3m	6.48	61
AgBr(II)	70	R	Hexagonal		4.0		7.15		3	P3 <sub>1</sub> 21	9.44	183
AgCl(I)	N	R	Cubic	NaCl	5.547				4	Fm3m	5.77	61
AgCl(II)	74	R	Hexagonal	B9	4.06		7.02		3	P3 <sub>1</sub> 21	7.12	183
AgCl(II)	74	R	Orthorhombic		6.90	5.08	4.05		4	Pnma	6.70	97
AgF(I)	N	R	Cubic	NaCl	4.932				4	Fm3m	7.02	61
AgF(II)	25	R	Cubic	CsCl	2.945				1	Pm3m	8.25	97
AgF(III)		R	Hexagonal		3.246		6.226		2		7.40	86
AgI(I)	N	145.8	Cubic		5.044				2	Im3m	6.07	61
AgI(II)	N	R	Hexagonal	Wurtzite	4.58		7.494		2	P6 <sub>3</sub> mc	5.73	61
AgI(II')	N	R	Cubic	ZnS	6.486				4	F43m	5.71	61
AgI(III)	4	R	Cubic	NaCl	6.07				4	Fm3m	6.97	123
	95	R	Cubic	NaCl	5.67				4	Fm3m	8.55	123
AgI(IV)	3	R	Tetragonal		4.58		6.00		2		6.19	123
AgI(V)	100	R	Tetragonal		4.615		5.020		4		9.85	123
CsF(I)	N	R	Cubic	NaCl	6.008				4	Fm3m	5.16	61
CsF(II)	48	R	Cubic	CsCl	3.39				1	Pm3m	7.18	205

## CRYSTALLOGRAPHIC DATA

Table II -Continued

COMPOUND	Pressure (kbar)	Temperature (°C)	Crystal System	Structure Type	a (Å)	b (Å)	c (Å)	Angle (°)	Z	Space Group	Density (g/cm <sup>3</sup> )	Ref.
<u>Halides cont'd.</u>												
CuBr(I)	N	480	Cubic	αAgI	4.56				2	Im3n	5.02	61
CuBr(II)	N	430	Hexagonal	Wurtzite	4.06		6.66		2	P6 <sub>3</sub> nc	5.01	61
CuBr(III)	N	R	Cubic	ZnS	5.691				4	F43n	5.17	61
CuBr(IV)	50	R	*									123
CuBr(V)	55	R	Tetragonal		5.40		4.75		4		6.88	123
CuBr(VI)	75	R	Cubic	NaCl	5.14				4	Fm3n	7.02	123
CuCl(I)	N	410	Hexagonal	Wurtzite	3.91		6.42		2	P6 <sub>3</sub> nc	3.35	61
CuCl(II)	N	25	Cubic	ZnS	5.416				4	F43n	4.138	61
CuCl(III)	10	450	*									123
CuCl(IV)	55	R	Tetragonal		5.21		4.61		4		5.25	123
CuCl(V)	70	R	Cubic	NaCl	4.93				4	Fm3n	5.49	123
CuI(I)	N	440	Cubic	Disordered	6.14				4	F43n	5.44	61
CuI(II)	N	390	Hexagonal	Wurtzite	4.31		7.09		2	P6 <sub>3</sub> nc	5.54	61
CuI(III)	N	R	Cubic	ZnS	6.059				4	F43n	5.69	61
CuI(IV)	16	R	Rhombohedral		4.164		20.41		6		6.19	123

Table II -Continued

## CRYSTALLOGRAPHIC DATA

COMPOUND	Pressure (kbar)	Temperature (°C)	Crystal System	Structure Type	a (Å)	b (Å)	c (Å)	Angle (°)	Z	Space Group	Density (g/cm <sup>3</sup> )	Ref.
<u>Halides cont'd.</u>												
CuI(V)	65	R	Tetragonal	Red PbO	4.02		5.70		2	P4/mmm	6.87	123
CuI(VI')	77	120	Cubic	S. C.	5.627				4		7.10	123
CuI(VII)	20	800	*									
CuI(VIII)	120	R	Cubic	NaCl	5.15				4	Fm3m	9.26	123
CsCl(I)	N	R	Cubic	CsCl	4.123				1	Pm3m	3.99	61
CsCl(II)	N	500	Cubic	NaCl	7.09				4	Fm3m	3.14	61
KBr(I)	N	R	Cubic	NaCl	6.599				4	Fm3m	2.75	61
KBr(II)	22		Cubic	CsCl	3.74				1	Pm3m	3.78	205
KCl(I)	N	R	Cubic	NaCl	6.2929				4	Fm3m	1.98	61
KCl(II)	22	R	Cubic	CsCl	3.58				1	Pm3m	2.69	205
KF(I)	N	R	Cubic	NaCl	5.344				4	Fm3m	2.53	61
KF(II)	35		Cubic	CsCl	3.06				1	Pm3m	3.36	205
KI(I)	N	R	Cubic	NaCl	6.0655				4	Fm3m	3.13	61
KI(II)	19	R	Cubic	CsCl	3.94				1	Pm3m	4.51	205
LiCl(I)	N	R	Cubic	NaCl	5.1399				4	Fm3m	2.07	61
NaBr(I)			Cubic		5.974				4	Fm3m	3.20	61

## CRYSTALLOGRAPHIC DATA

Table II -Continued

COMPOUND	Pressure (kbar)	Temperature (°C)	Crystal System	Structure Type	a (Å)	b (Å)	c (Å)	Angle (°)	Z	Space Group	Density (g/cm <sup>3</sup> )	Ref.
<u>Halides cont'd.</u>												
NaCl(I)	N	R	Cubic	NaCl	5.6402				4	Fm3m	2.16	61
NaCl(II)	290	R	Cubic	CsCl	2.997				1	Pm3m	3.60	15
NaF(I)	N	R	Cubic	NaCl	4.628				4	Fm3m	2.81	61
NaI(I)	N	R	Cubic	NaCl	6.475				4	Fm3m	3.67	61
NH <sub>4</sub> Br(I)	N	250	Cubic	NaCl	6.90				4	Fm3m	1.98	210
NH <sub>4</sub> Br(II)	N	26	Cubic	CsCl	4.059				1	Pm3m	2.43	61
NH <sub>4</sub> Br(III)	N	-73	Tetragonal		5.713		4.055		2	P4/mmm	2.44	61
NH <sub>4</sub> Br(IV)	N	-170	*									
NH <sub>4</sub> Cl(I)	N	250	Cubic	NaCl	6.52				4	Fm3m	1.28	210
NH <sub>4</sub> Cl(II)	N	26	Cubic	CsCl	3.8758				1	Pm3m	1.52	61
NH <sub>4</sub> Cl(III)	N	-185	Cubic		3.8200				1	P43m	1.59	210
NH <sub>4</sub> F(I)	N	23	Hexagonal	Wurtzite	4.4385		7.1635		2	P6 <sub>3</sub> mc	1.01	61
NH <sub>4</sub> F(II)	4	23	Tetragonal		10.2		3.37		8		1.40	133,134
NH <sub>4</sub> F(III)	11.5	23										196
NH <sub>4</sub> F(IV)	4	178	Cubic	NaCl	5.77				4	Fm3m	1.28	40

Table II -Continued

## CRYSTALLOGRAPHIC DATA

COMPOUND	Pressure (kbar)	Temperature (°C)	Crystal System	Structure Type	a (Å)	b (Å)	c (Å)	Angle (°)	Z	Space Group	Density (g/cm <sup>3</sup> )	Ref.
<u>Halides cont'd.</u>												
NH <sub>4</sub> I(I)	N	R	Cubic	NaCl	7.259				4	Fm3m	2.52	61
NH <sub>4</sub> I(II)	N	-17	Cubic	CsCl	4.38				1	Pm3m	2.86	61
NH <sub>4</sub> I(III)	N	-100	Tetragonal		6.18		4.37		2	P4/nmm	2.87	61
NH <sub>4</sub> I(IV)	10	-100	*									
ND <sub>4</sub> Br(I)	N	-30	Cubic	CsCl	4.034				1	Pm3m	2.53	61
ND <sub>4</sub> Br(II)	N	-71.5	Tetragonal		5.713		4.055		2	P4/nmm	2.44	61
ND <sub>4</sub> Br(III)	N	-140	Cubic		4.010				1	P43m	2.63	61
ND <sub>4</sub> F(I)	N	23	Hexagonal	Wurtzite	4.4378		7.1635		2	P6 <sub>3</sub> mc	1.12	61
ND <sub>4</sub> F(II)	4	23	Tetragonal		10.2		3.37		8		1.56	133
EbBr(I)	N	R	Cubic	NaCl	6.868				4	Fm3m	3.39	61
EbBr(II)	5	R	Cubic	CsCl	4.09				1	Pm3m	3.01	205
EbCl(I)	N	R	Cubic	NaCl	6.590				4	Fm3m	2.80	61
EbCl(II)	5	R	Cubic	CsCl	3.91				1	Pm3m	3.35	205
EbF(I)	N	R	Cubic	NaCl	5.64				4	Fm3m	3.87	61
EbF(II)	5	R	Cubic	CsCl	3.29				1	Pm3m	4.87	205
EbI(I)	N	R	Cubic	NaCl	7.34				4	Fm3m	3.57	61

Table II -Continued

## CRYSTALLOGRAPHIC DATA

COMPOUND	Pressure (kbar)	Temperature (°C)	Crystal System	Structure Type	a (Å)	b (Å)	c (Å)	Angle (°)	Z	Space Group	Density (g/cm <sup>3</sup> )	Ref.
<u>Halides cont'd.</u>												
TlBr	N	R	Cubic	CsCl	3.838				1	Pm3m	7.032	61
TlCl	N	R	Cubic	CsCl	3.9846				1	Pm3m	7.46	61
TlF(I)	N	82	Tetragonal	Distorted NaCl	3.771		6.115		2	I4/mmm	8.53	61
TlF(II)	N	R	Orthorhombic		5.180	5.495	6.080		4	Fmmm	8.57	49
TlF(III)	12	R	*									
TlI(I)	N	R	Orthorhombic		5.24	4.57	12.92		4	Cmcm	7.11	61
TlI(II)	5	R	Cubic	CsCl	4.10				1	Pm3m	7.98	24

Table II -Continued

## CRYSTALLOGRAPHIC DATA

COMPOUND	Pressure (kbar)	Temperature (°C)	Crystal System	Structure Type	a (Å)	b (Å)	c (Å)	Angle (°)	Z	Space Group	Density (g/cm <sup>3</sup> )	Ref.
<u>Cyanides</u>												
AgCN(I)	N	R	Rhombohedral		3.99		5.26		3	R3c	4.05	61
AgCN(II)	12	R	*									
AuCN(I)	N	25	Hexagonal		3.40		5.09		1	P6mm	7.30	61
AuCN(II)			*									
CsCN(I)	N	20	Cubic	CsCl	4.29				1	Pm3m	3.34	61
CsCN(II)	N	-80	Rhombohedral		5.79		7.78		3	R $\bar{3}$ m	3.50	61
KCN(I)	N	25	Cubic	NaCl	6.527				4	Fm3m	1.555	61
KCN(III)	30	100	Cubic	CsCl	3.808				1	Pm3m	1.96	171.56
KCN(IV)	25	23	Monoclinic		5.530	5.209	3.743	95	2	Cm	1.66	56
KCN(V)	N	-80	Monoclinic		8.04	4.53	7.47	109.4	4	Cc	1.69	61
KSCN(I)	N	160	Tetragonal		6.70		7.73		4	I4/mcm	1.86	61
KSCN(II)	N	20	Orthorhombic		6.66	7.58	6.635		4	Pcmb	1.89	61
KSCN(III)	20	450	*									
KSCN(IV)	28	500	*									
KSCN(V)	42	525	*									
NaCN(I)	N	20	Cubic	NaCl	5.88				4	Fm3m	1.60	61
NaCN(II)	N	-10	Orthorhombic		4.71	5.61	3.74		2	Immm	1.64	61

Table II -Continued

## CRYSTALLOGRAPHIC DATA

COMPOUND	Pressure (kbar)	Temperature (°C)	Crystal System	Structure Type	a (Å)	b (Å)	c (Å)	Angle (°)	Z	Space Group	Density (g/cm <sup>3</sup> )	Ref.
<u>Cyanides cont'd.</u>												
NaSCN	N	R	Orthorhombic		13.45	4.10	5.66		8	Pnma or Pn2 <sub>1</sub> a	1.735	164
RbCN(I)	N	R	Cubic		6.83 <sup>4</sup>				4	P2 <sub>1</sub> 3	2.32	61
RbCN(II)	N	-182	Monoclinic		6.66	4.87	4.77	94.3	2		2.37	61
<u>Borides</u>												
PtB	N	R	Hexagonal		3.36		4.06		1	P6 <sub>3</sub> /mmc	17.2	5,208
<u>Carbides</u>												
MoC(I)	N	R	Hexagonal		2.898		2.809		1		8.77	47
MoC(I)	N	R	Hexagonal		3.00		14.58		6		9.46	47
MoC(I)	N	R	Hexagonal		2.932		10.97		4	P6 <sub>3</sub> /mmc	8.78	47
MoC(II)	N	R	Cubic	NaCl	4.27				4	Fm3m	9.29	47
ReC	60	800	Hexagonal	γ-MoC	2.840		9.85		4	P6 <sub>3</sub> /mmc	19.12	168

Table II -Continued

## CRYSTALLOGRAPHIC DATA

COMPOUND	Pressure (kbar)	Temperature (°C)	Crystal System	Structure Type	a (Å)	b (Å)	c (Å)	Angle (°)	Z	Space Group	Density (g/cm <sup>3</sup> )	Ref.
<u>Nitrides</u>												
BN(I)	N	35	Hexagonal	BN	2.502		6.661		6	P6 <sub>3</sub> /mmc	2.29	61
BN(II)	N	R	Cubic	ZnS	3.62				4	F43m	3.48	38
BN(III)	N	R	Hexagonal	Wurtzite	2.55		4.20		2	P6 <sub>3</sub> nc	3.49	38
<u>Oxides</u>												
BaO(I)	N	R	Cubic	NaCl	5.542				4	Fm3m	5.98	61
BaO(II)	100	R	Tetragonal		4.549		3.606		2		6.82	116
BaO(III)	180	R	Tetragonal	PbO	4.397		3.196		2	P4/mmm	8.24	114
EuO(I)	N	R	Cubic	NaCl	5.143				4	Fm3m	8.20	61
EuO(II)	310	R	Cubic	NaCl	4.743				4	Fm3m	10.45	88
EuO(III)	400	R	Cubic	CsCl	2.92				1	Pm3m	11.21	88
FeO	N	R	Cubic	NaCl	4.312				4	Fm3m	6.76	104
SnO(I)	N	R	Tetragonal	PbO	3.796		4.816		2	P4/mmm	6.40	61
SnO(II)	60	R	Hexagonal	Wurtzite	3.42		5.62		2	P6 <sub>3</sub> nc	6.80	204
SrO(I)	N	R	Cubic	NaCl	5.142				4	Fm3m	5.07	61
SrO(II)	175	R	Tetragonal		4.912		4.949		4		5.76	117
ZnO(I)	N	R	Hexagonal	Wurtzite	3.242		5.176		2	P6 <sub>3</sub> nc	5.70	61
ZnO(II)	N	R	Cubic	NaCl	4.28				4	Fm3m	6.92	16

## CRYSTALLOGRAPHIC DATA

Table II -Continued

COMPOUND	Pressure (kbar)	Temperature (°C)	Crystal System	Structure Type	a (Å)	b (Å)	c (Å)	Angle (°)	Z	Space Group	Density (g/cm <sup>3</sup> )	Ref.
<u>Oxides cont'd.</u>												
NaOH(II)	N	R	Orthorhombic	TII	3.397	11.32	3.397		4	Amam	2.02	61
NaOH(I)	N	300	Monoclinic		3.434	3.428	6.068	109.8	2	P2 <sub>1</sub> /m	1.98	162
NaOH(III)			*									162
NaOH(IV)			*									162
NaOH(V)			*									162
<u>Phosphides</u>												
BP	N	R	Cubic	ZnS	4.54				4	F $\bar{4}$ 3m	2.97	209
GaP(I)	N	18	Cubic	ZnS	5.447				4	F $\bar{4}$ 3m	4.138	61
GaP(II)	220	R	*									120,142
GeP(I)	N	R	Tetragonal		3.544		5.581		2	I4mm	4.90	60
InP(I)	N	18	Cubic	ZnS	5.868				4	F $\bar{4}$ 3m	4.79	61
InP(II)	N	R	Cubic	NaCl	5.71				4	Fm $\bar{3}$ m	5.20	85
SiP(I)	N	R	Orthorhombic		6.90	9.40	7.68		12		2.36	143
SiP(II)	N	R	Cubic	ZnS	5.241				4	F $\bar{4}$ 3m	2.73	143

Table II -Continued

## CRYSTALLOGRAPHIC DATA

COMPOUND	Pressure (kbar)	Temperature (°C)	Crystal System	Structure Type	a (Å)	b (Å)	c (Å)	Angle (°)	Z	Space Group	Density (g/cm <sup>3</sup> )	Ref.
<u>Phosphides cont'd</u>												
SnP(I)	N	R	Hexagonal		8.78		5.98		8		4.98	105
SnP(II)	N	R	Tetragonal		3.831		5.963		2		5.68	59
SnP(III)	N	R	Cubic		5.536				4	Fm $\bar{3}$ m	5.86	59
<u>Sulfides</u>												
CdS(I)	N	R	Hexagonal	Wurtzite	4.134		6.713		2	P6 $\bar{3}$ mc	4.83	61
CdS(I)	N	R	Cubic	ZnS	5.835				4	F $\bar{4}$ 3m	4.83	61
CdS(II)	77	R	Cubic	NaCl	5.27				4	Fm $\bar{3}$ m	6.44	119
FeS(I)	N	R	Hexagonal	Triolite	5.946		11.72		<u>12</u>	P $\bar{6}$ 2c	4.85	61
FeS(II)	100	22	**									
FeS(III)	N	R	Hexagonal	NiAs	3.426		5.687		2	P6 $\bar{3}$ /mmc	4.60	61
HgS(I)	N	R	Cubic	ZnS	5.858				4	F $\bar{4}$ 3m	7.69	16
HgS(II)		R	Hexagonal	HgS	4.149		9.149		3	Pe $\bar{1}$ 21	8.19	119
NiS(I)	N	R	Hexagonal	NiAs	3.428		5.340		2	P6 $\bar{3}$ /mmc	5.55	61
NiS(II)	20	R	Hexagonal		**				2	P6 $\bar{3}$ mc		122
SmS(I)	N	R	Cubic	NaCl	5.863				4	Fm $\bar{3}$ m	6.01	61
SmS(II)	6.5	R	Cubic	NaCl	5.70				4	Fm $\bar{3}$ m	6.54	89

Table II -Continued

## CRYSTALLOGRAPHIC DATA

COMPOUND	Pressure (kbar)	Temperature (°C)	Crystal System	Structure Type	a (Å)	b (Å)	c (Å)	Angle (°)	Z	Space Group	Density (g/cm <sup>3</sup> )	Ref.
<u>Sulfides cont'd.</u>												
ZnS(I)	N	R	Cubic	ZnS	5.406				4	F $\bar{4}3$ ,	4.10	61
ZnS(II)	N	R	Hexagonal	Wurtzite	3.811		6.234		2	P6 <sub>3</sub> mc	4.10	61
ZnS(III)	190	R	*									110
ZnS(IV)	420	R	*									110
<u>Arsenides</u>												
BAs	N	R	Cubic	ZnS	4.777				4	F $\bar{4}3$ m	5.22	207
GaAs(I)	N	R	Cubic	ZnS	5.654				4	F $\bar{4}3$ m	5.32	208
GaAs(II)	190	R	*									126
GaAs(III)	200	R	*									126
GeAs(I)	N	R	Tetragonal		3.715		5.832		2		6.10	60
InAs(I)	N	R	Cubic	ZnS	6.036				4	F $\bar{4}3$ m	5.73	210
InAs(II)	100	R	Cubic	NaCl	5.514				4	Fm $\bar{3}$ m	7.52	85
MnAs(I)	N	R	Hexagonal	NiAs	3.710		5.691		2	P6 <sub>3</sub> mc	6.54	210
MnAs(II)	N	50	Orthorhombic	MnP	6.39	5.64	3.63		4	Pbnm	6.78	210

Table II -Continued

## CRYSTALLOGRAPHIC DATA

COMPOUND	Pressure (kbar)	Temperature (°C)	Crystal System	Structure Type	a (Å)	b (Å)	c (Å)	Angle (°)	Z	Space Group	Density (g/cm <sup>3</sup> )	Ref.
<u>Antimonides</u>												
AlSb(I)	N	R	Cubic	ZnS	5.985				4	F $\bar{4}$ 3m	4.61	61
AlSb(II)	120	R	Tetragonal	$\beta$ -Sn	5.375		5.911		2	I4 <sub>1</sub> /amd	5.91	85
GaSb(I)	N	R	Cubic	ZnS	6.135				4	F $\bar{4}$ 3m	5.51	61
GaSb(II)	90	R	Tetragonal	$\beta$ -Sn	5.348		2.973		2	I4 <sub>1</sub> /amd	7.39	85
	1 atm.	90 K			5.47		3.06		2			
InSb(I)	N	R	Cubic	ZnS	6.474				4	F $\bar{4}$ 3m	5.79	61
InSb(II)	26	R	Tetragonal	$\beta$ -Sn	5.862		3.105		2	I4 <sub>1</sub> /amd	7.40	11
InSb(III)	125	R	Hexagonal		6.099		5.708		2		8.50	11
InSb(IV)	70	R	Orthorhombic		2.921	5.56	3.06		1		7.90	11
<u>Selenides</u>												
CdSe(I)	N	R	Hexagonal	Wurtzite	4.30		6.02		2	P6 <sub>3</sub> mc	5.65	119
CdSe(II)	32	R	Cubic	NaCl	5.49				4	Fm3m	7.68	119
HgSe(I)	N	R	Cubic	ZnS	6.09				4	F $\bar{4}$ 3m	8.41	119
HgSe(II)	15	R	Hexagonal	HgS	4.32		9.62		3	P3 <sub>1</sub> 21	8.10	119
InSe(I)	N	R	Hexagonal		4.05		16.93		4	P6 <sub>3</sub> /mmc	5.351	61
InSe(II)	40	520	*									202
PbSe(I)	N	R	Cubic	NaCl	6.122				4	Fm3m	8.28	61
PbSe(II)	42	R	Orthorhombic		11.71	4.36	4.42		4	Fmna	8.42	118

Table II -Continued

## CRYSTALLOGRAPHIC DATA

COMPOUND	Pressure (kbar)	Temperature (°C)	Crystal System	Structure Type	a (Å)	b (Å)	c (Å)	Angle (°)	Z	Space Group	Density (g/cm <sup>3</sup> )	Ref.
<u>Tellurides</u>												
CdTe(I)	N	R	Cubic	ZnS	6.478				4	F $\bar{4}$ 3m	5.87	61
CdTe(II)	30	R	Cubic	NaCl	5.92				4	Fm3m	6.13	146
CdTe(III)	100	R	Tetragonal		5.86		2.94		2	I4 <sub>1</sub> /amd	6.29	146
CdTe(III)	200	R	Tetragonal		5.62		2.96		2	I4 <sub>1</sub> /amd	6.80	146
EuTe(I)	N	R	Cubic	NaCl	6.591				4	Fm3m	6.50	186
EuTe(II)	100	R	Cubic	CsCl	3.755				1	Pm3m	2.68	186
GeTe(I)	N	R	Rhombohedral	As	4.171		10.661		3		6.29	61
GeTe(II)	40	R	Cubic	NaCl	5.80				4	Fm3m	6.82	61
GeTe(II)	N	60	Cubic	NaCl	5.998				4	Fm3m	6.16	61
HgTe(I)	N	R	Cubic	ZnS	6.37				4	F $\bar{4}$ 3m	8.42	61
HgTe(II)	20	R	Hexagonal	HgS	4.51		10.13		3	P3 <sub>1</sub> 21	9.16	90
InTe(I)	N	R	Tetragonal	TlSe	8.437		7.139		8	I4/mcm	6.34	61
InTe(II)	30	R	Cubic	NaCl	6.160				4	Fm3m	6.89	9
InTe(II')	N	R	Tetragonal		6.06		6.55		4		6.69	9
MnTe(I)	N	R	Hexagonal		4.148		6.710		2	P6 <sub>3</sub> /mmc	6.06	61
MnTe(II)		R	Cubic		6.003				4	Fm3m	5.60	

Table II - Continued

## CRYSTALLOGRAPHIC DATA

COMPOUND	Pressure (kbar)	Temperature (°C)	Crystal System	Structure Type	a (Å)	b (Å)	c (Å)	Angle (°)	Z	Space Group	Density (g/cm <sup>3</sup> )	Ref.
<u>Tellurides cont'd.</u>												
PbTe(I)	N	R	Cubic	NaCl	6.36				4	Fm3m	8.64	61
PbTe(II)	43	R	Orthorhombic		11.61	4.00	4.39		4	Pnma	10.91	118
PrTe(I)	N	R	Cubic	NaCl	6.315				4	Fm3m	7.08	186
PrTe(II)	90	R	Cubic	CsCl	3.761				1	Pm3m	8.38	186
SmTe(I)	N	R	Cubic	NaCl	6.595				4	Fm3m	6.44	186
SmTe(II)	110	R	Cubic	CsCl	3.656				1	Pm3m	9.44	186
SnTe(I)	N	R	Cubic	NaCl	6.2956				4	Fm3m	6.56	118
SnTe(II)	20	R	Orthorhombic		11.59	4.37	4.48		4	Pnma	7.21	118
YbTe(I)	N	R	Cubic	NaCl	6.353				4	Fm3m	7.79	61
ZnTe(I)	N	R	Cubic	ZnS	6.101				4	F43m	5.64	61
ZnTe(II)			*									

## 2. Lithium Halides

### 2.1. Lithium Chloride

Lithium chloride which has the NaCl type structure has no known high pressure phase transitions. A determination of the melting curve up to 23 kilobars has been reported in a paper by Clark [45]. The published uncertainties are  $\pm 5^\circ\text{C}$  in temperature and  $\pm 0.10$  kbar in pressure.

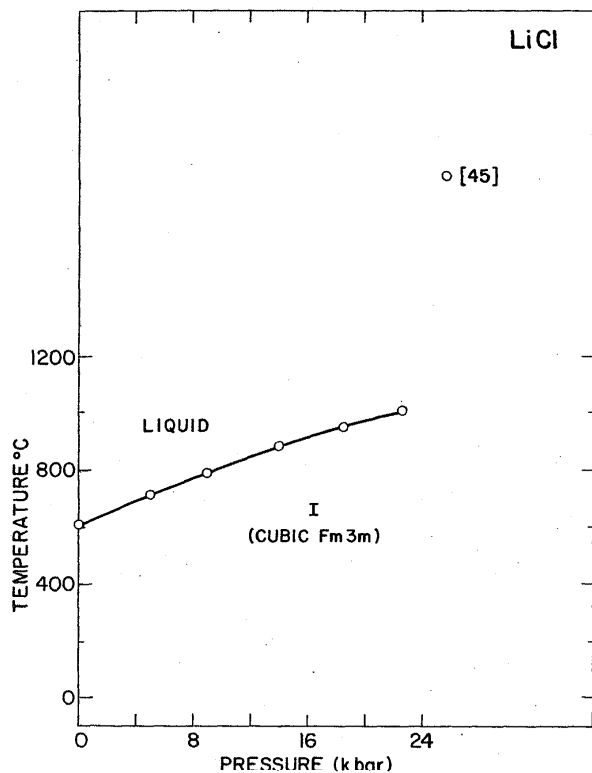


FIGURE 1. Melting curve for lithium chloride

## 3. Sodium Halides

There have been several investigations of the sodium halide room-temperature high-pressure phases by both static and dynamic methods. In sodium chloride, a phase transformation was reported at 17 kilobars [67], 18 kilobars [157], and 29 kilobars [112], but later these were determined to be erroneous [95]. Jamieson [84] has shown by x-ray diffraction studies, that the pressure of the B1-B2 transformation in a series of KCl-NaCl solid-solution samples increases with NaCl content. At 85% NaCl, the transformation occurs at 145 kilobars at room temperature. The B1-B2 phase transition in pure sodium chloride was reported by Bassett et al. [15] to occur at  $300 \pm 10$  kilobars. Piermarini and Block [151] determined the value of this transition as  $291 \pm 10$  kbar based upon Decker's equation of state for sodium chloride [53]. It is assumed that the other sodium halides should also have transformations at approximately this same pressure, since the cation seems to have the dominant effect in determining B1-B2 transition pressure in the alkali halides.

Pistorius has reported phase transitions in three sodium halides at the following pressures and temperatures; sodium fluoride [162, 163] at  $18.3 \pm 1$  kilobar and  $150^\circ\text{C}$  ( $16.8 \pm 2$  kilobars at room temperature), sodium bromide [158] at  $11.5 \pm 2.5$  kilobars and  $175$ – $200^\circ\text{C}$ , and sodium iodide [161] in the range of  $10.2$ – $11.6$  kilobars and  $164$ – $175^\circ\text{C}$ . It is not clear at the present time what these transitions represent, since one would expect the B1-B2 transition at a much higher pressure. Furthermore, if a transition existed in this low pressure range, it would be expected to intersect with either the temperature axis, the pressure axis, or the melting curve in a least one point in the low pressure region. In support of this view, x-ray measurements of sodium fluoride reveal no new phase up to 130 kilobars.

Three different papers have been presented on the experimental determination of the melting curves of the sodium halides. Clark [45] reported melting curve determinations for all the sodium halides, performed in a hydrostatic apparatus, using nitrogen as the pressure transmitting fluid. In this work, the thermocouple correction is very good up to 10 kilobars, but is high above this point. At the highest pressure of 23 kilobars and approximately  $1150^\circ\text{C}$ , the correction to the temperature is  $10^\circ\text{C}$ . With this modification, Clark's [45] stated uncertainties appear to be realistic. His temperature corrections were high, by a factor of approximately 1.8 at the high end of the scale, and not the factor of 2–3, claimed by Pistorius [154].

### 3.1. Sodium Fluoride

Comparison between the two determinations of the melting curve for sodium fluoride [44 and 151] indicate a fair agreement. At about 12 kilobars, the two curves differ by about  $10^\circ\text{C}$ , which is the sum of the combined experimental uncertainties of both studies. In selecting the best fit to the experimental data the two curves should be weighted equally, but since it extends to 40 kilobars, an extrapolation of Clark's [44] data to this point is not justified.

### 3.2. Sodium Chloride

A melting curve for sodium chloride up to 65 kilobars, by Akella et al. [2] is in very good agreement with the determinations of both Clark [44] and Pistorius [151]. The best fit to this data for the entire range to 65 kilobars is well within the experimental uncertainties of each of the experiments.

### 3.3. Sodium Bromide

In Clark's [45] studies on the sodium bromide melting curve, a large uncertainty of  $\pm 10^\circ$  was necessary, due to the difficulty in the determination of the melting point. For this reason, the work of Pistorius [154] will be selected as the best fit.

### 3.4. Sodium Iodide

Of the two studies on the melting behavior of sodium iodide [45, 154] the work of Pistorius is preferred as the best fit for the same reasons discussed above for sodium bromide.

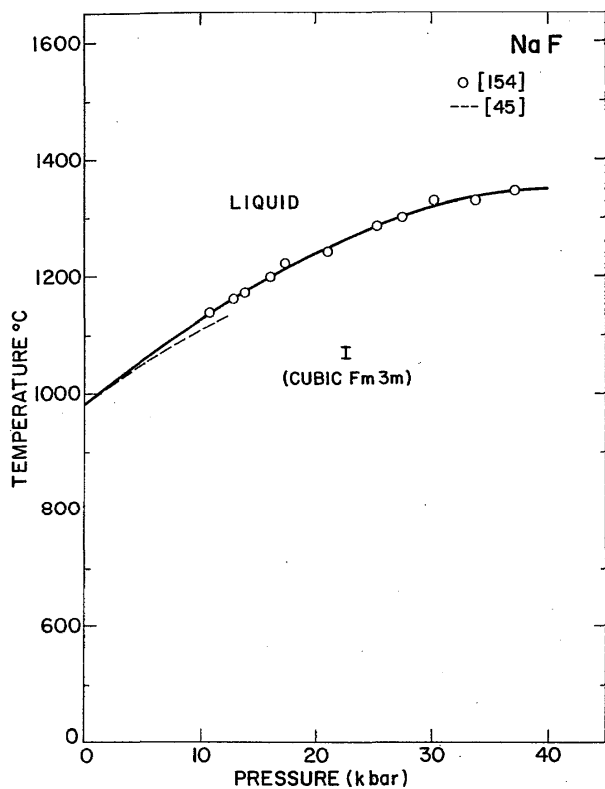


FIGURE 2. Melting curve for sodium fluoride

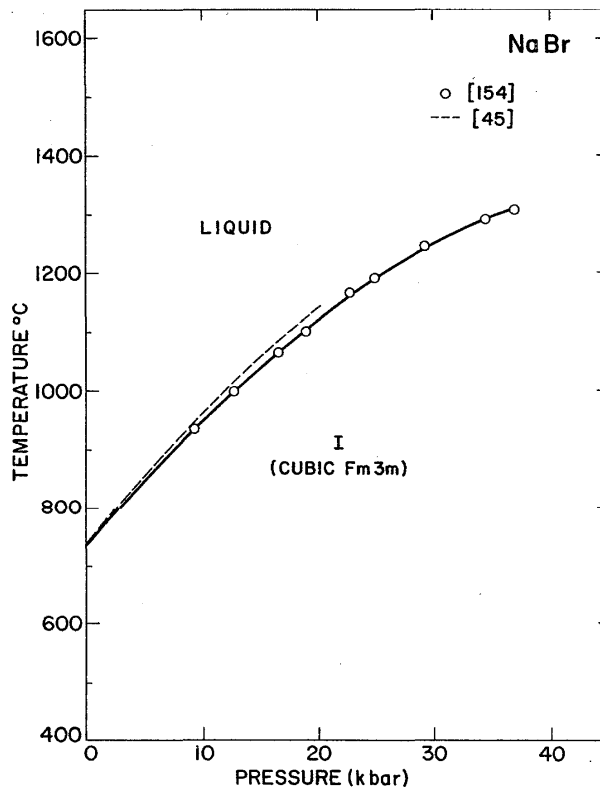


FIGURE 4. Melting curve for sodium bromide

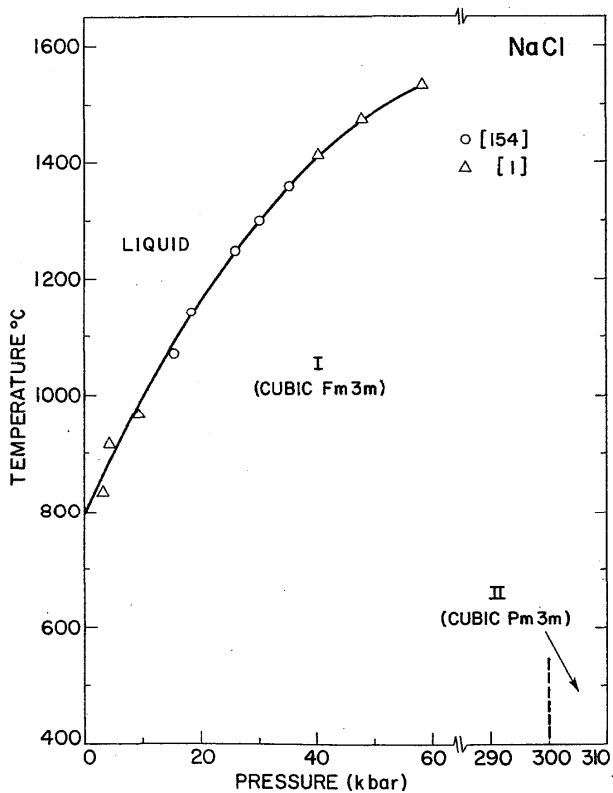


FIGURE 3. Partial phase diagram for sodium chloride

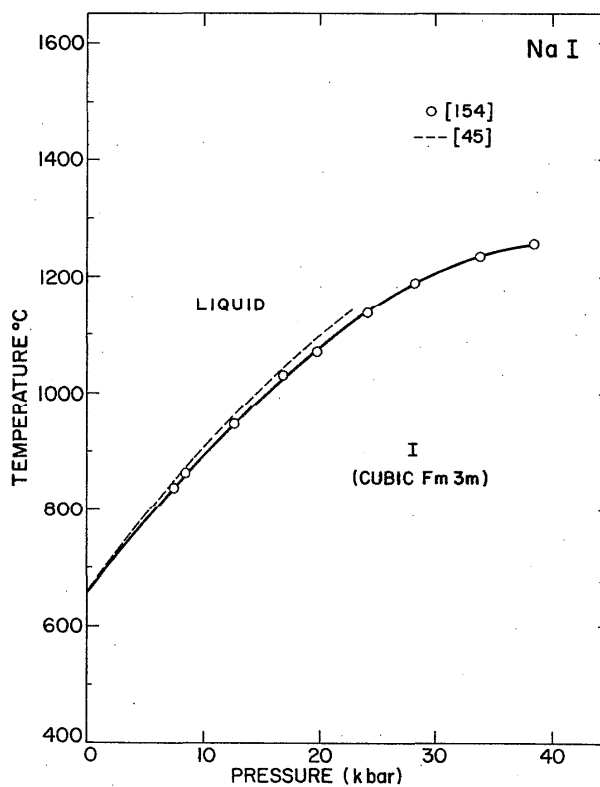


FIGURE 5. Melting curve for sodium iodide

## 4. Potassium Halides

### 4.1. Potassium Fluoride

There are no known high pressure phases in potassium fluoride.

### 4.2. Potassium Chloride

The room temperature high pressure transition point in potassium chloride has been investigated by two different groups. In Bridgman's [29] original work, he placed the transition pressure at 19.52 kilobars, while in later work [34], he revised this to 19.67 kilobars at 25 °C. Kennedy and La Mori [108] arrived at the value of  $19.23 \pm 0.21$  kilobar for the KCl transition pressure. This work was performed in the piston cylinder device, using the piston rotation method to reduce friction. In selecting the best value for the pressure of this transition, two values have been averaged, giving that of Kennedy and La Mori a weight of 4, and obtaining  $19.30 \pm 0.30$  kilobars. High pressure x-ray examination of KCl by Weir and Peiomarine [205] and Nagasaki and Minomura [37] verify the NaCl-CsCl type transition.

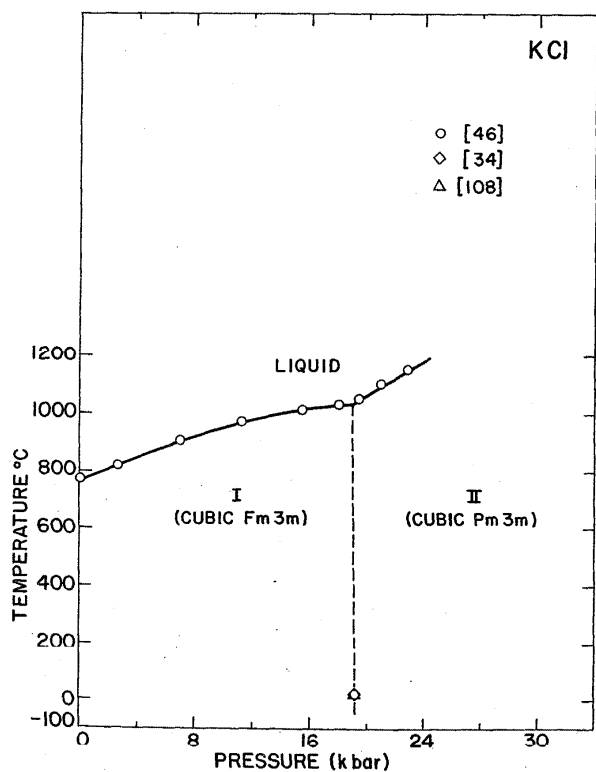


FIGURE 6. Phase Diagram for potassium chloride

### 4.3. Potassium Bromide

High pressure studies of potassium bromide only involve examination of the KBr(I)-KBr(II) phase boundary. No melting studies have been undertaken. Bridgeman's [29] first

measurements of the KBr transition place it at 18.92 kilobars at 25 °C. However, in his later work [34], which he considered more accurate, this value was revised to 18.05 kilobars at 25 °C. No error flags were given in this work. On the basis of three separate experiments in the piston cylinder apparatus, Kennedy and La Mori [118] obtained the value  $17.88 \pm 0.06$  kilobar for the transition pressure.

Weir and Piermarine [205] confirm that KBr(II) has the cesium chloride type structure on the basis of powder x-ray diffraction studies, using the diamond anvil pressure apparatus.

Measurements of the KBr(I)-KBr(II) phase boundary from room temperature to approximately 200 °C have been published by Bridgman [29] and Pistorius [158,159]. It was noted by Pistorius that at low temperatures, the alkali halide transitions are quite sluggish, and consequently, unless one waits for an unreasonably long time between piston advances, the transition pressure may be displaced toward higher pressures. This appears to be evident in the room temperature points of both Pistorius and Bridgman, and is probably also true for Kennedy and La Mori's value. The best values can be found from an extrapolation of the higher temperature points where the sluggishness has diminished. The best fit to the KBr(I)-KBr(II) phase boundary is represented by Pistorius' data, giving a room temperature transition pressure of  $17.43 \pm 0.10$  kilobars.

### 4.4. Potassium Iodide

At room temperature, Bridgeman [34] obtained the value of 17.84 kilobars (18.7 kilobars at -78 °C) for the pressure of

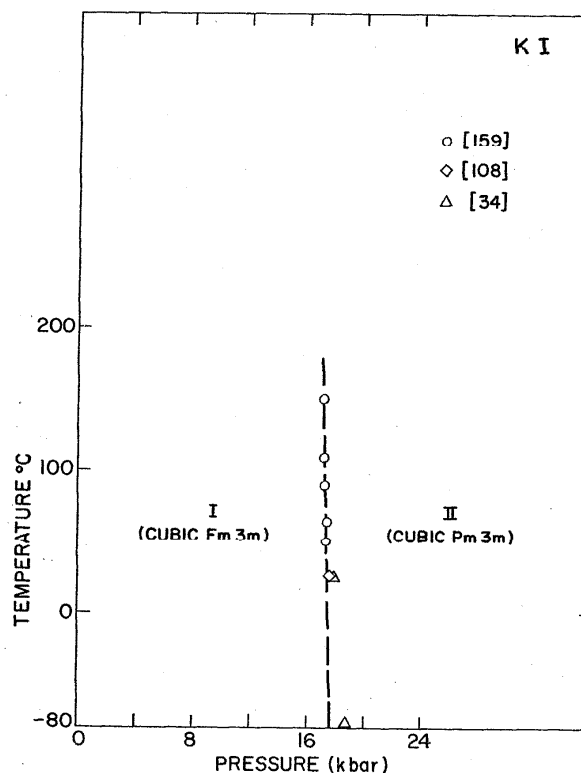


FIGURE 7. Partial phase diagram for potassium iodide

the potassium iodide transition. Kennedy and La Mori [108] obtained a value of  $17.485 \pm 0.240$  kilobars at  $25^\circ\text{C}$ . From high temperature measurements, Pistorius [159] obtained an extrapolated value of  $17.343 \pm 0.045$  kilobars. In this work, it was shown that potassium iodide is sluggish like potassium chloride at room temperature. Above  $50^\circ\text{C}$ , this sluggishness disappeared, permitting greater accuracy in the determination of the phase boundary. On the basis of this work, it is suggested that  $17.35 \pm 0.10$  kilobars be accepted as the best value for this transition pressure. Weir and Piermarini [205] identified the potassium iodide(II) phase as cesium chloride type.

### 5. Rubidium Halides

Polymorphism in the alkali halides at elevated pressures was first discovered by Slater [187] in RbBr and RbI. Bridgman subsequently studied these transitions [29,37], and observed the corresponding transition in RbCl. The transitions for the rubidium halides occur at approximately 5 kbar.

Since the alkali halides crystallize in both the NaCl and CsCl type structures, it was assumed that at high pressure, alkali halide crystals with the NaCl-type would transform to the CsCl type phase. The first confirmation of this assumption was published by Jacobs [82,83] in 1938 for RbI. Employing x-ray diffraction techniques, he studies RbI up to a pressure of  $4500 \text{ kg/cm}^2$  (4.4 kbar), and showed that RbI(II) was simple cubic (CsCl-type), with a lattice constant  $a=4.33 \text{ \AA}$ . Piermarini and Weir [149] discovered RbF was also converted to a CsCl-type structure with a lattice constant  $a=3.27 \text{ \AA}$ . In a later work, Weir and Piermarini [205] published the

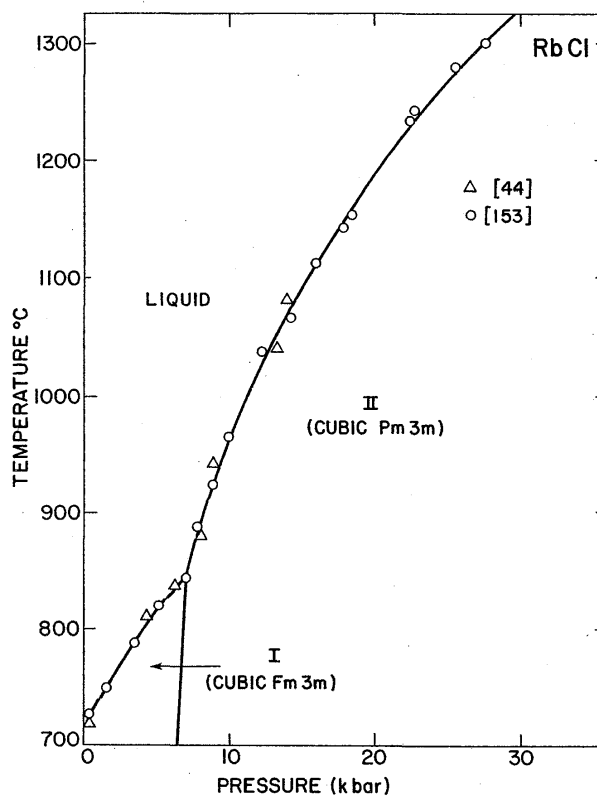


FIGURE 9. Phase diagram for rubidium chloride

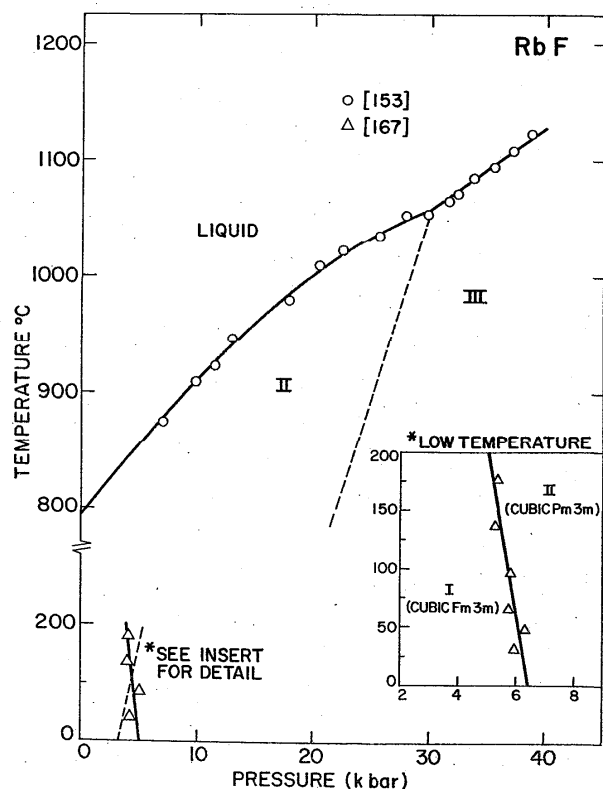


FIGURE 8. Phase diagram for rubidium fluoride

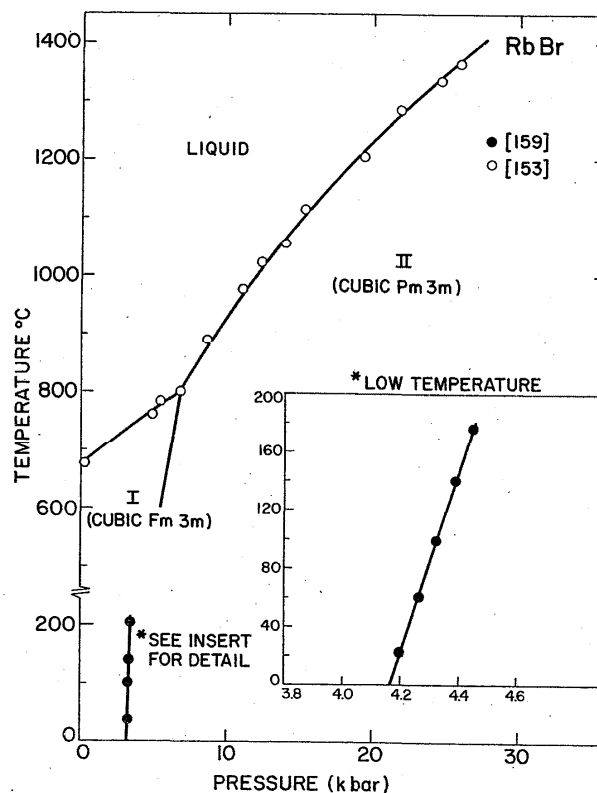


FIGURE 10. Phase diagram for rubidium bromide

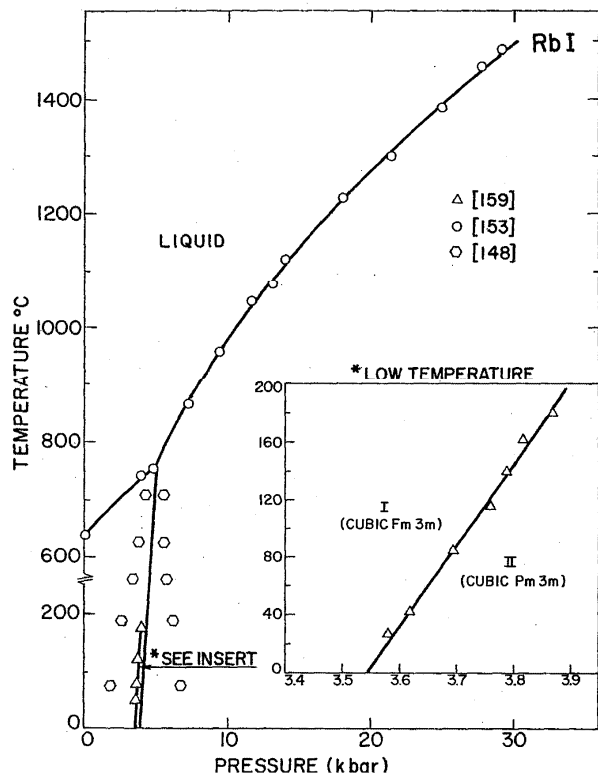


FIGURE 11. Phase diagram for rubidium iodide

results of a study in which all the rubidium halide high pressure phases were examined and shown to be of the CsCl-type.

An experimental determination of the RbI(I)-RbI(II) phase boundary [167] revealed a negative slope. A later study [153] of the melting curve indicates the existence of a triple point at approximately 30 kbar which is interpreted as the coexistent point between RbI(L), RbI(I), and RbI(II). This suggests that the phase boundary has a positive slope.

The melting curve of RbCl was determined by Clark [45] up to approximately 12 kbar. Temperatures were determined with Pt-Pt 10% Rh thermocouples and melting or freezing was detected by changes in the rate of heating or cooling, and also by DTA. The thermocouples were calibrated against the melting points of NaCl (800.5 °C) and KCl (770 °C). The thermocouple correction of Birch [18] was used to correct for the effect of pressure on the emf. The magnitude of this correction at the maximum pressure and temperatures is 8 °C, compared to 6 °C predicted by the more recent calibration of Getting and Kennedy [76].

## 6. Cesium Halides

### 6.1. Cesium Fluoride

Bridgman failed to find any evidence for the polymorphism of CsF at high pressure from either of his compressibility studies in the range to 42 kbar at room temperature and 56 kbar at 137 °C [158]. Weir and Piermarini [205], however, reported a transition at approximately 20 kbar, detected both visually, and by x-ray diffraction techniques, using a diamond

anvil pressure cell. The normal NaCl-type structure transforms to the CsCl-type structure.

The CsF(I)-CsF(II) phase boundary was measured by Pistorius and Snyman [167] up to 173.5 °C in a piston cylinder type apparatus. Pressures were corrected for friction by taking the mean transition pressures on the increasing and decreasing pressure cycle, assuming friction is symmetrical. Temperature was measured by means of a thermocouple in a well outside the pressure chamber near the sample. Temperature measurements were corrected for the thermal gradients by calibrating the reading against a thermocouple in the sample position in a blank run. The pressure effect on the thermocouple junction was not considered in this calibration, nor was it stated what kind of thermocouple was used.

A room temperature transition pressure of  $19.7 \pm 1.5$  kbar was determined in good agreement with Weir and Piermarini [205]. The slope of the phase boundary is

$$\frac{dT}{dP} = 20 \pm 6 \text{ } ^\circ\text{C/kbar.}$$

### 6.2. Cesium Chloride

Compressibility studies of cesium chloride at room temperature indicate that there are no polymorphic transition up to 45 kilobars [196]. The melting curve has been measured at a pressure range up to 15 kilobars at approximately 1150 °C by DTA techniques [45]. A cusp in the melting curve indicates the presence of a new high temperature phase which probably is the NaCl-type structure.

These measurements were made in a pressure cell designed by Birch [19], which utilized nitrogen as the pressure transmitting medium, with sample chamber large enough to contain a furnace. Pressures were determined by a manganin wire manometer, and temperature with a Pt-Pt 10% Rh thermocouple. The temperature was corrected for the effect of pressure on the thermal emf. The temperature was measured with a Pt-Pt 10% Rh thermocouple, and a correction for the effect of pressure on the thermocouple was applied. The correction is given by  $T + 0.7 \times 10^{-6} PT$ , where  $P$  is the pressure in bars,  $T$  is the centigrade temperature, and the maximum  $T$  is approximately 18 °C. The correction was determined by a linear extrapolation of Birch's measurement [18], and gives a correction factor higher than that of Getting and Kennedy [11]. In view of the experimental techniques employed, published uncertainties of  $\pm 5$  °C in temperature are probably good in range up to 10 kilobars, but not reliable above that, due to the temperature correction term, which is approximately 6 °C too high at the upper end of the melting curve. The pressure published in this work are considered to be very accurate.

## 7. Ammonium Halides

The high pressure transformations in the ammonium halides were originally studied by Bridgman [28] and the phase boundaries were experimentally determined by Stevenson [193]. Garland et al. [69, 70, 71, and 72] has made numerous

investigations of both  $\text{NH}_4\text{Cl}$  and  $\text{NH}_4\text{Br}$  by ultrasonic techniques, and has obtained very accurate data for the phase boundaries as a function of temperature and pressure.

### 7.1. Ammonium Fluoride

The phase diagram of ammonium fluoride is fairly complex.  $\text{NH}_4\text{F(I)}$ , the normal room temperature, 1-bar-pressure phase is interesting because of its close structural relation to water. Ammonium fluoride(I) and Ice(I) are iso-structural and their lattice parameters and bond distances differ only by about 4%. Stevenson [193] performed the initial high-pressure studies on  $\text{NH}_4\text{F}$ , and detected the  $\text{NH}_4\text{F(I)}\text{-NH}_4\text{F(II)}$  phase transition at 3.8 kbar and room-temperature from the 28% volume change. Subsequently, Swenson and Tedeschi [196] reported an additional room-temperature transition at 11.5 kbar, with an additional volume change of 11% of the 1 bar volume. This phase is designated  $\text{NH}_4\text{F(III)}$ . In this same study, a high temperature phase designated  $\text{NH}_4\text{F(IV)}$  was also discovered. Melting curves and complete phase diagrams for  $\text{NH}_4\text{F}$  have been reported by Kuriakose and Whalley [112], and Pistorius [155].

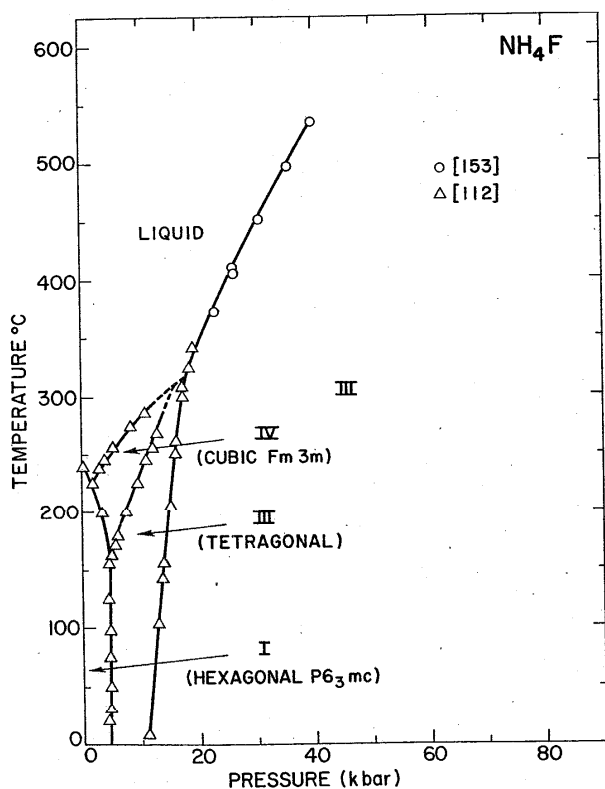


FIGURE 12. Phase diagram for ammonium fluoride

The crystal structure of both  $\text{NH}_4\text{F(II)}$  and  $\text{ND}_4\text{F(II)}$  were indexed by Morosin and Schirber as tetragonal, with nearly identical lattice constants [133]. In a study of the quenched phases of  $\text{NH}_4\text{F(II)}$  and  $\text{NH}_4\text{F(III)}$  [134], several new reflections were obtained in the  $\text{NH}_4\text{F(II)}$  diffraction patterns which were not consistent with the previous tetragonal indexing, and were too complicated to be solved by powdered

methods. The crystal system of  $\text{NH}_4\text{F(III)}$  is cubic with a structure which is described as "essentially, but not exactly of the cesium chloride type." The diffraction pattern of  $\text{NH}_4\text{F(IV)}$  is consistent with a sodium chloride-like structure with  $a = 5.77 \pm 0.04 \text{ \AA}$  at  $180 \pm 20$ , and approximately 4 kbar [40].

In studying the quenched  $\text{NH}_4\text{F}$  phases, three new phases were detected upon heating to room temperature. As the quenched phase of  $\text{NH}_4\text{F(II)}$  was heated from 77 K, a transition to  $\text{NH}_4\text{F(V)}$  was detected between 220 K and 240 K [134]. This phase could be indexed on the basis of a wurtzite-like structure. A study of quenched phase III revealed two new metastable phases  $\text{NH}_4\text{F(VI)}$  and  $\text{NH}_4\text{F(VII)}$ , which appeared at approximately 115 K and 200 K, respectively, upon heating from 77 K to room temperature [134]. Neither of these phases could be unambiguously identified.

### 7.2. Ammonium Chloride

Ammonium chloride undergoes an order-disorder phase transformation involving the relative orientation of the tetrahedral  $\text{NH}_4^+$  ions. In both phases, the crystal has a CsCl cubic structure. However, in the disordered phase, the  $\text{NH}_4^+$  ions are distributed at random, with respect to two equivalent orientations in the cubic unit cell, while in the ordered phase, all  $\text{NH}_4^+$  ions have the same orientation. At 1 bar (241.9 K), a small first order transition is superimposed on a general lambda-like behavior. This first order discontinuity at the transition diminishes as the pressure is increased, and at a tricritical point near 256 K and 1492 bar, the transition becomes continuous.

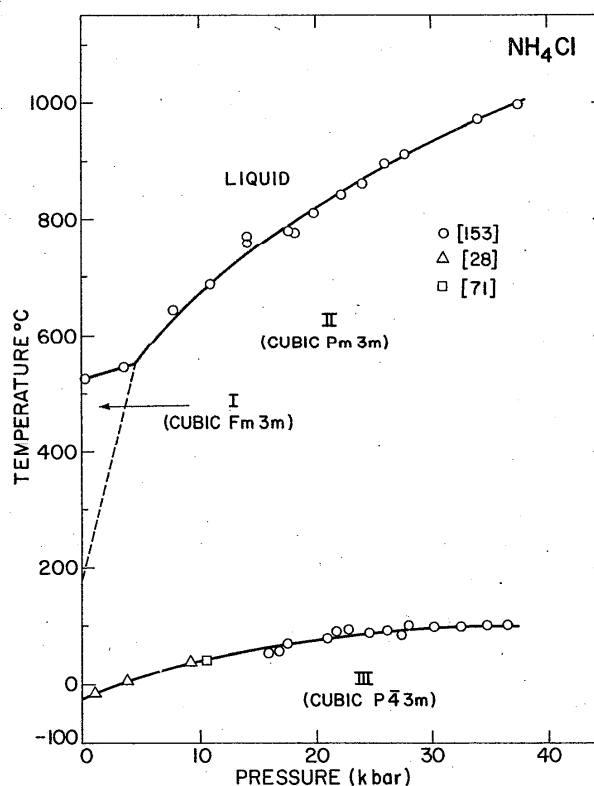


FIGURE 13. Phase diagram for ammonium chloride

### 7.3. Ammonium Bromide

Ammonium bromide has at least four solid phases. The high temperature  $\text{NH}_4\text{Br(IV)}$  has the CsCl type disordered cubic unit cell, and undergoes two different disorder-order transformations of the  $\lambda$ -type to  $\text{NH}_4\text{Br(II)}$  and  $\text{NH}_4\text{Br(III)}$ . The  $\text{NH}_4\text{Br(II)-NH}_4\text{Br(I)}$  is of first order, and  $\text{NH}_4\text{Br(I)}$  has the CsCl-type cubic structure with the ordering of  $\text{NH}_4^+$  almost certainly corresponding to the parallel arrangement which is observed in  $\text{NH}_4\text{Cl}$ . The structure of the ordered phase  $\text{NH}_4\text{Br(II)}$  is cubic  $\text{Pm}3\text{m}$ , and  $\text{NH}_4\text{Br(III)}$  is not known. The phase diagrams of the deuterated ammonium bromide and ammonium iodide [193] are both similar to that of ammonium chloride.

### 7.4. Ammonium Iodide

Ammonium iodide exists in at least 4 solid forms. The low temperature phase diagram contains three phases and is very similar to ammonium bromide and deuterated ammonium bromide [193] in its behavior. The melting curve has been determined from 500–900 °C and up to 40 kbar. Its behavior is analogous to  $\text{NH}_4\text{Cl}$  and  $\text{NH}_4\text{Br}$ . The region from -40 °C to 500 °C has not been investigated at high pressure.

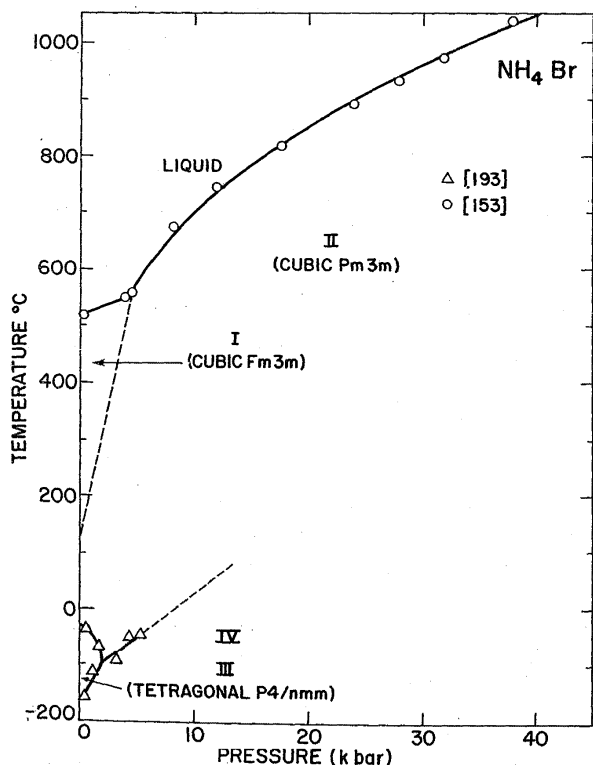


FIGURE 14. Phase diagram for ammonium bromide

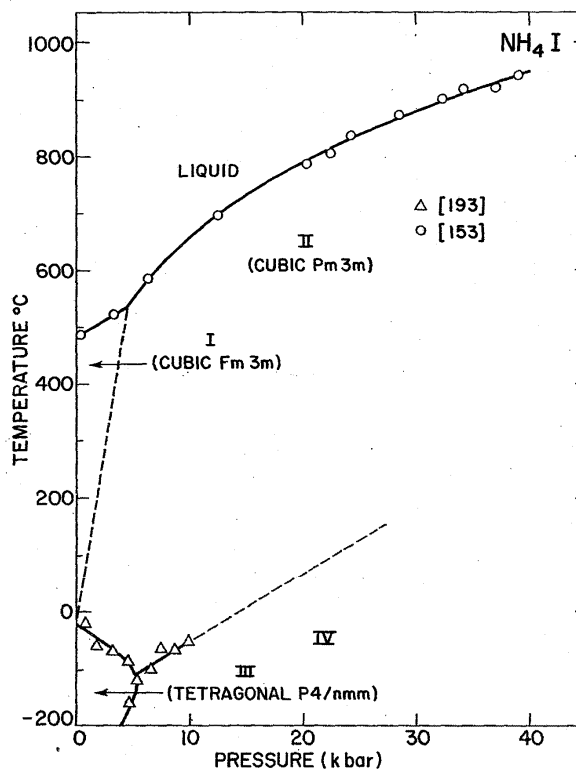


FIGURE 15. Phase diagram for ammonium iodide

## 8. Copper Halides

### 8.1. Copper Chloride

The phase diagram of copper chloride has been determined to 160 kbar by a combination of techniques. The phase boundaries in the region up to 40 kbar and 700 °C was determined by DTA [170] techniques. The phase boundaries up to 400 °C and 160 kbar [64] were determined by shifts of the optical absorption edge. Investigations by Chu et al. [43] indicate the presence of an insulator-metal transition at 40 kbar and room temperature.

### 8.2. Copper Bromide

The phase diagram of  $\text{CuBr}$  has been determined in the region 200–900 °C and 0–40 kbar by Rapoport and Pisorius [170] with DTA techniques, while the region 0–300 °C and 40–80 kbar was determined by Edwards and Drickamer [64], whose work was based upon pressure shifts of the optical absorption edge. The phase diagram of  $\text{CuBr}$  is very similar to that of  $\text{CuCl}$ .

The high pressure x-ray studies of  $\text{CuBr}$  were performed by Meisalo and Kalliomaki [123], who reported that  $\text{CuBr(III)}$  is stable up to 50 kbar. At this pressure, they detected a strongly birefringent phase in agreement with Van Valkenburg, if one takes into account the difference in pressure scales. The stability region of  $\text{CuBr(IV)}$  is so narrow that it was impossible to produce a single phase region or to detect x-ray dif-

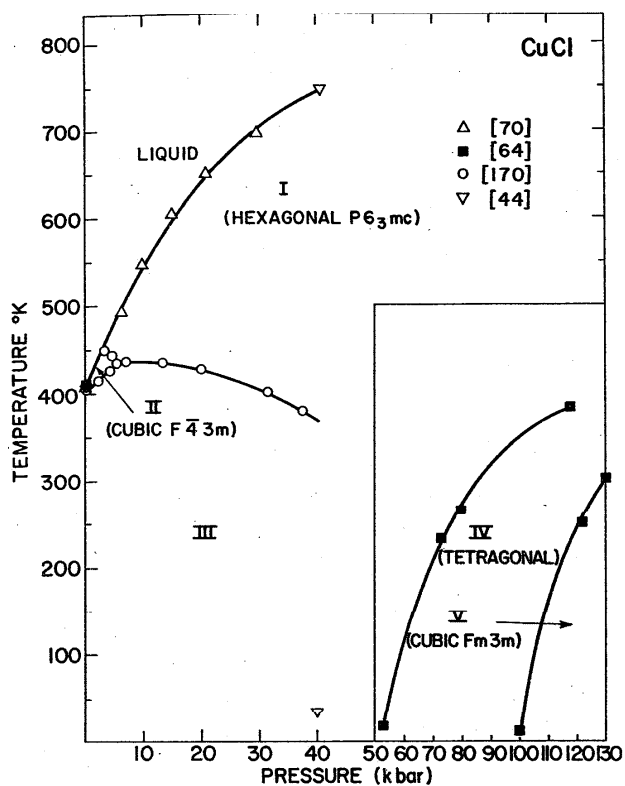


FIGURE 16. Phase diagram for copper chloride

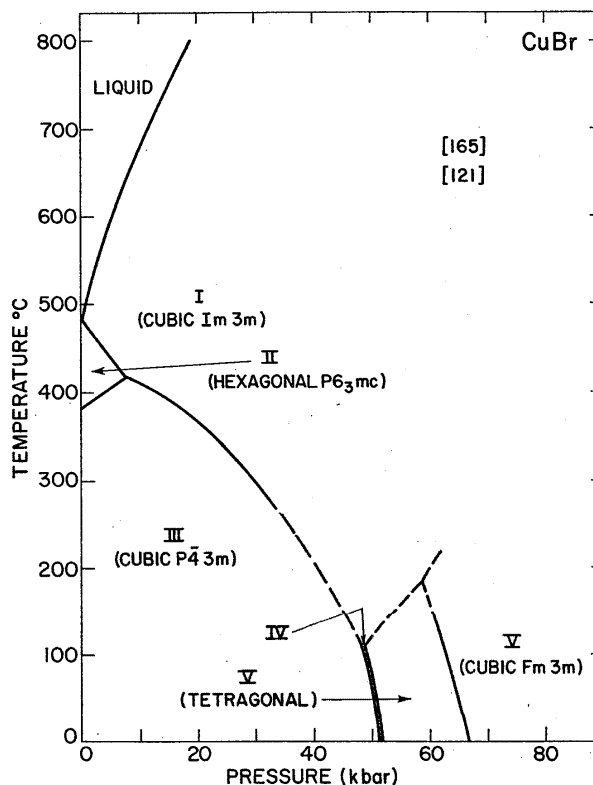


FIGURE 17. Phase diagram for copper bromide

fraction lines assignable to it. Pressure calibration in this work is based upon Decker's [53] NaCl scale.

Very close to the CuBr III-IV boundary, CuBr(V) was detected. It is strongly amber colored, and weakly birefringent. The indexing of this phase was based upon a tetragonal unit cell with lattice parameters  $a=5.40 \text{ \AA}$ ,  $c=4.75 \text{ \AA}$ , and  $Z=4$ .

At room temperature and atmospheric pressure CuBr(III) has the zincblende structure which is stable up to 379–400 °C, depending upon the purity of the sample. CuBr(II) has the wurtzite structure, and is stable up to 470 °C. Between 470 °C and the melting point at 483 °C, CuBr(I) is the stable modification. It has the  $\alpha$ -AgI structure (33.4), which is a defect b.c.c. structure. Meisalo and Kallimaki [121] detected a pale yellow phase at about 48 kbar and 120 °C. At 50 kbar and 140 °C they were able to obtain only one diffraction line with  $d=2.981 \text{ \AA}$ . Assuming this to be the CuBr(I) phase, they tentatively suggest this reflection may correspond to (110) and a cubic lattice parameter a 4.22 Å.

This transition from CuBr(V)-CuBr(VI) is very sluggish, and occurs at approximately 66 kbar. X-ray diffraction patterns taken at 75 kbar and room temperature suggest the NaCl-type structure with  $a=5.140 \text{ \AA}$ .

### 8.3. Copper Iodide

The behavior of copper iodide has been studied extensively under high pressure/high temperature conditions. The very first studies were Bridgman's [33] compressibility studies in 1916, in which he determined the volume discontinuity at

10–15 kbar associated with the CuI(III)-CuI(IV) transition over the temperature range 120–200 °C. In 1937 [32], he extended this measurement to –100 °C. In 1963, Van Valkenburg [200] reported two new phase transitions, on the basis of optical observations up to 125 kbar, one at 4 kbar, and one at 5 kbar. Edwards and Drickamer [64] studied the effect of pressure on the optical absorption edge in CuI, and reported two new phase transitions at 41 kbars and 80 kbars. No evidence for the transitions at 4 and 5 kbars was reported. Neuhaus and Hintze [137] studied CuI up to 20 kbar, using both optical absorption and electrical resistivity measurements. They report detecting the 4, 5, and 14 kilobar transitions. Later results of high pressure high temperature studies on the polymorphism of CuI by Yang, Schwartz, and La Mori (211) also confirm these findings.

When CuI is heated to 100–200 °C at an approximate pressure of 75 kbar, a new phase (VI') can be identified, which has been tentatively indexed as simple cubic with a tetramolecular unit cell (122). X-ray data of CuI(VI') give a lattice constant  $a=5.627 \text{ \AA}$ . CuI(VI') can be retained metastably at room temperature and high pressure for long periods of time. When CuI(VI') was heated to high temperature at a pressure 90–100 kbar, a new phase designated CuI(VIII) is detected. The data are marginal and on the basis of 3 lines it fits the NaCl-type structure with  $a=5.15 \text{ \AA}$  at 120 kbar and room temperature.

The most complete study of the phase boundaries of CuI is that of Rapoport and Pistorius [170]. This work confirms the 14 kbar and 40 kbar room-temperature transitions. This study, based on DTA techniques (chromel-alumel thermo-

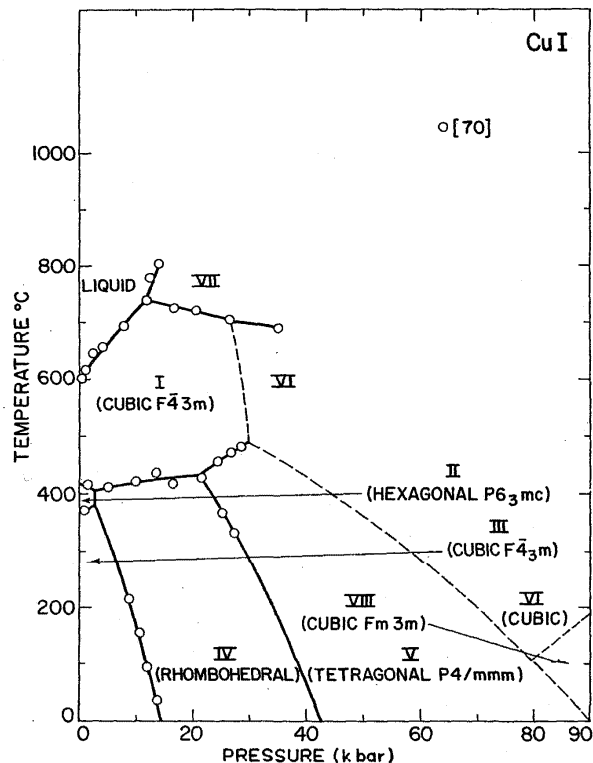


FIGURE 18. Phase diagram for copper iodide

couples) covers the range 0–900 °C and 0–40 kbars. Corrections were made for the effect of pressure on the thermal emf. The phase diagram was the result of six separate runs. Friction corrections were made by averaging the results from the increasing and decreasing pressure cycles. The points plotted along the solid-solid phase boundaries represent the mean value of the heating and cooling cycle, while points along the solid-liquid boundaries are the melting signals. It is felt that the published uncertainty in temperature of  $\pm 2$  °C is realistic, while the uncertainty in pressure of  $\pm 0.5$  kbar probably reflects experimental reproducibility only, since some sources of systematic error were not considered, the principal one being the effect temperature has on pressure.

One of the principal difficulties in drawing conclusions about high pressure phases of the copper halides is the lack of agreement on crystal structure data. At atmospheric pressure CuI(III) has the zincblende structure, and is stable up to 369 °C. CuI(II) has the wurtzite form and is stable between 369 °C and 407 °C. CuI(I), which exists from 407 °C to the melting point at 602 °C, has a disordered zincblende structure [128]. In their x-ray examinations of the room temperature high pressure phases, neither Moore et al. [131] or Meisalo and Kalliomaki [123 and 124] found evidence for the existence of the 4 and 5 kbar phase transitions.

Moore et al. [132] reported the 14 kbar CuI transition to be very sluggish and not completely transformed until a pressure of 30 kbars was attained. In their x-ray patterns, they observed a set of strong zincblende lines, plus a set of new lines which were weak, but reproducible. They further suggest that the strong zincblende lines indicate that the basic

cubic close packing of the iodine atoms is preserved and the structural changes result only from a redistribution of copper atoms. Moore et al. [132] propose a cubic indexing which is based upon a super cell of the zincblende structure, i.e. a doubling of the lattice constant.

Meisalo and Kalliomaki [123, 124] conclude that CuI(IV) is rhombohedral with  $a=7.216$  Å and  $\alpha=33.5^\circ$  ( $a=4.164$  Å and  $C_{hex}=20.41$  Å) at 16 kbars and room temperature. According to their observations, CuI(IV) is definitely birefringent. The observed intensities were approximated by varying the atomic position parameters of I(000, 00 $u$ ) and Cu(00 $v$ , 00 $v+u$ ) yielding the values  $u=0.535$  and  $v=0.14$ . Values of  $u=5/8$  and  $v=1/8$  would describe the original zincblende structure. More reliable intensity data would be necessary for a refinement of the structure. The volume change at the transition is approximately 4 percent.

Moore et al. [132] located the CuI(V) phase at 53 kbar, and also indexed it, on the basis of a supercell of the zincblende phase. Meisalo and Kalliomaki [123] observed this phase at 42 kbar and proposed a tetragonal "anti" litharge (red PbO) structure with lattice constants  $a=4.02$  Å and  $c=5.70$  Å at about 65 kbar and room temperature, and  $u=0.28$ . The tetragonal CuI(V) phase appears to be stable at pressures exceeding 100 kbar at room temperature.

## 9. Silver Halides

There have been two principal experimental investigations of the melting curve of the silver halides up to a pressure of 58 kilobars. The original work by Eaton in 1965 [52] was performed in a tetrahedral anvil device, the phase transitions being monitored by differential thermal conductivity analysis. Chromel-alumel thermocouples were used for temperature measurement, and no correction was made for the effect of pressure of the thermal emf. The author estimated temperature to be accurate to 1.5% and pressure to  $\pm 0.5$  kilobar below 20 kilobars. The sources and purities of the silver halides used were as follows: (1) silver chloride from Baker Chemical Company, stated to be 99.7% pure; (2) silver bromide from Fisher Scientific Company, stated to be purified; (3) silver iodide from Fisher Scientific Company, stated to be chemically pure. The pressure calibration of the tetrahedral press was based upon the following fixed points: Bi(I-II) at 25.4 kbars, Tl(II-III) at 37 kbars, and Ba(I-II) at 59 kbars.

The work by Akella et al. in 1969 [2] was performed in a piston-cylinder apparatus in which the melting curve was detected by differential thermal analysis up to a maximum pressure range of 68 kilobars.

Boron nitride, fired at 480 °C for 48 hours serves as the pressure transmitting medium. The samples were contained in a stainless steel capsule with a silver lining. Chromel-alumel thermocouples were used to measure the melting temperatures. The melting and freezing at every pressure point was measured at least four times and reproducible to  $\pm 1$  °C. The thermocouple correction of Getting and Kennedy [76] was used. Measurements were made on both the compression and decompression cycle. The pressure calibration is based upon force per unit area corrected for friction.

### 9.1. Silver Fluoride

The high pressure region of AgF has been studied by both x-ray diffraction [97, 180] and piston cylinder techniques [2]. AgF(I) is cubic NaCl-type, and undergoes a phase transition at 25 kbar to the CsCl type structure. A determination of the transition pressure has been made by Haleck and Jamieson [97], whose value of  $25.14 \pm 0.04$  kbar represents the average of the transition pressure on the upstroke and downstroke. Vaidya and Kennedy [199] determined a value of 24.8 kbar for the equilibrium transition pressure, but do not present any error flags. The estimated uncertainty for this transition, based upon both equation of state and instrumental consideration is 0.4 kbar. The best value of  $25 \pm 0.4$  kbar is based upon an average of the two published values. The slope  $dT/dP$  of the AgF(I)-AgF(II) phase boundary is  $37$  °C/kbar, and the relative volume change at the transition is 10%.

A new phase formed from AgF(II) on decreasing pressure, found by Vaidya and Kennedy [199] was studied by x-ray diffraction by Jamieson et al. [86]. AgF(III) was indexed as hexagonal with  $c=6.226$  Å,  $a=3.246$  Å, and  $Z=2$ . It is probably an inverted NiAs structure. Its formation pressure is highly dependent upon the history of pressure variation of the sample. All three phases, B1, B2, and hexagonal, gave x-ray patterns with each line split into two lines of equal intensity. This phenomenon has been interpreted as arising from a decomposition into two non-stoichiometric phases, one Ag-rich and the other F-rich [86].

### 9.2. Silver Chloride

The high pressure room temperature transition in silver chloride was first discovered by Bridgman [27] by dilatometry (88 kilobars). In a later work, Montgomery published a value of  $76 \pm 2$  kilobars [130] for this transition. In his work he measured compression of AgCl simultaneously with the electrical resistance of bismuth, and demonstrated that the AgCl transition occurred at lower pressure than the Bismuth III-V transition. In calibration of the pressure, the bismuth I-II and III-V fixed points were used and a linear pressure-load relation used. It is now known that the pressure-load relation is not linear in this region and it is estimated the transition point for AgCl should have been about  $82 \pm 2$  kilobars (bases upon Bi III-V at 88 kbars). A measurement was made in which the molar volume of AgCl was measured as a function of pressure using NaCl as an internal standard. Using this method to correct Bridgman's pressures, a transition pressure of  $74 \pm 3$  kilobars is calculated.

Studies of the melting curve of AgCl have been reported by Akella et al. [2] and Deaton [52]. The results of Akella et al. [2] are recommended, due to the corrections made in experimental data.

### 9.3. Silver Bromide

The melting curve of Akella et al. [2] is preferred for the reasons discussed in the section on silver chloride. The room temperature high pressure phase of AgBr was first detected by Bridgman [27], who placed the transition at 84 kilobars.

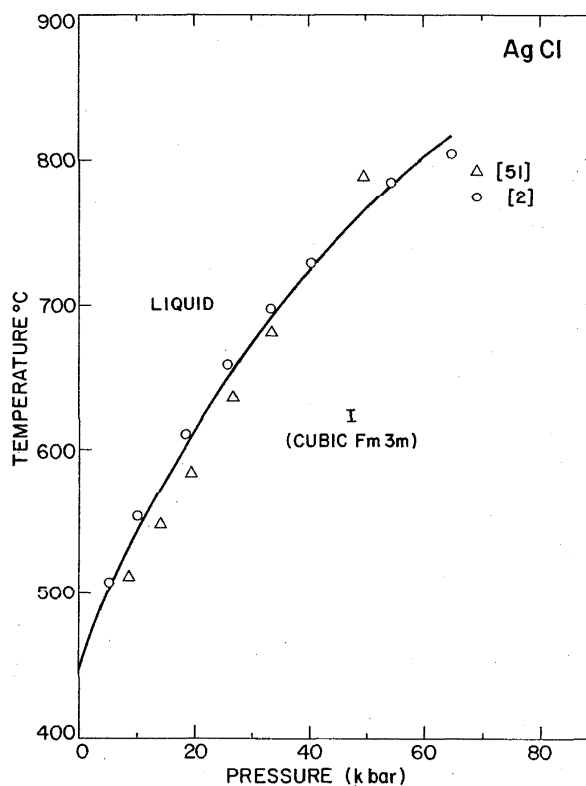


FIGURE 19. Melting curve for silver chloride

According to our presently accepted NaCl pressure calibration, this transition pressure would have to be revised to approximately 70 kilobars.

The structure of AgBr(II) was studied by Schock and Jamieson [183], who described it as an analogue of HgS (cinnabar). The hexagonal lattice constants are  $a=4.0$  Å,  $c=7.51$  Å with  $c/a=1.79$ . This corresponds to a compression at the transition of  $\Delta V_T/V_0=17\%$ , compared to Bridgman's value of 1.1%. In view of the previous discussion of AgCl(II), some doubt exists on the correctness of this result. It is recommended that the AgBr(II) crystal structure be re-examined, and the AgBr(I)-AgBr(II) room temperature transition pressure be calibrated against the NaCl scale [53].

### 9.4. Silver Iodide

Silver iodide can exist in at least six polymorphic modifications. At room temperature and atmospheric pressure the wurtzite phase AgI(II) is the thermodynamically stable form [39]. This phase is readily converted to the metastable sphalerite-type phase AgI(II') by grinding in a mortar or by pressing and above 80 °C (below 146 °C) readily reverts to the wurtzite form. Above 146 °C, the high temperature phase AgI(I) has a disordered body centered cubic structure [194].

The high pressure polymorphism of AgI was first investigated by Bridgman [27], who discovered the 3 kbar transition. The crystal structure of the high-pressure phase, AgI(III), was determined by Jacobs [82] to be NaCl-type by x-ray diffraction under pressure. This determination has also been confirmed by Piermarini and Weir [149]. Van Valken-

burg [200] used the polarizing microscope to study the high pressure phases of silver iodide, and found a new strongly birefringent polymorph at approximately 3 kbar, separating the wurtzite and rock salt phases. This new phase, designated AgI(IV), was examined by Davis and Adams [51], using powder x-ray diffraction techniques, who found their patterns could be indexed as hexagonal, tetragonal, or orthorhombic, each with a large unit cell ( $Z=12$ ). In a later study, Moore and Kasper [131] were able to index AgI(V) as tetragonal with  $a=4.58 \text{ \AA}$ ,  $c=6.00 \text{ \AA}$  and  $Z=2$ . AgI(V), which occurs above 97 kbar, was first detected by Rigglenan and Drickamer [178] by measurements of electrical resistance vs. pressure. Attempts to index powder x-ray diffraction patterns of this phase have not been successful [14]. In addition, Bassett and Takehashi [14] also made a fairly detailed investigation of the phase boundaries and triple points in the low pressure region. The lower triple point occurs at  $3.1 \pm 0.4$  kbar and  $65 \pm 2 \text{ }^\circ\text{C}$ , while the higher triple point occurs at  $3.1 \pm 0.4$  kbar and  $98 \pm 2 \text{ }^\circ\text{C}$ .

Melting curves for AgI have been published by both Deaton [52] and Akella et al. [2]. The experimental technique is identical to that reported for the other silver halides.

## 10. Thallium Halides

### 10.1. Thallium Fluoride

The phase behavior of the thalious halides is much more diverse than observed for the alkali halides. Under normal conditions, TlF(II) crystallizes with an orthorhombic distortion of the NaCl-type structure. The space group is  $Fmmm$  and the unit cell contains four molecules. The TlF(II)-TlF(I) phase transition was reported by Cubicciotti et al. [49] to occur at  $82 \text{ }^\circ\text{C}$  at 1 bar pressure. Pistorius and Clark [165] have proposed this structure belongs to space group  $I4/mmm$  on the basis of powder x-ray diffraction studies.

The melting curve and phase boundaries of TlF were also investigated by Pistorius and Clark [165] in the region up to 40 kbar. Pressures were generated in a piston cylinder device and phase changes were detected by means of differential thermal analysis, using chromel-alumel thermocouples below  $950 \text{ }^\circ\text{C}$  and Pt-Pt 10% Rh thermocouples at higher temperature. Corrections were made for the effect of pressure on the thermocouple emf. Each phase boundary was based on three separate runs. The points plotted represent the mean of heating and cooling in the solid-solid transitions, and melting temperatures for solid-liquid phase changes. Investigation of the melting curve up to 41.5 kbar showed no evidence for further phase transitions. The crystal structure of TlF(III) has not been determined.

### 10.2. Thallium Chloride

Both TlCl and TlBr crystallize in the CsCl-type structure at atmospheric pressure. Since this structure, with a coordination of eight, represents the most stable configuration for ionic crystals, no further pressure induced phase tran-

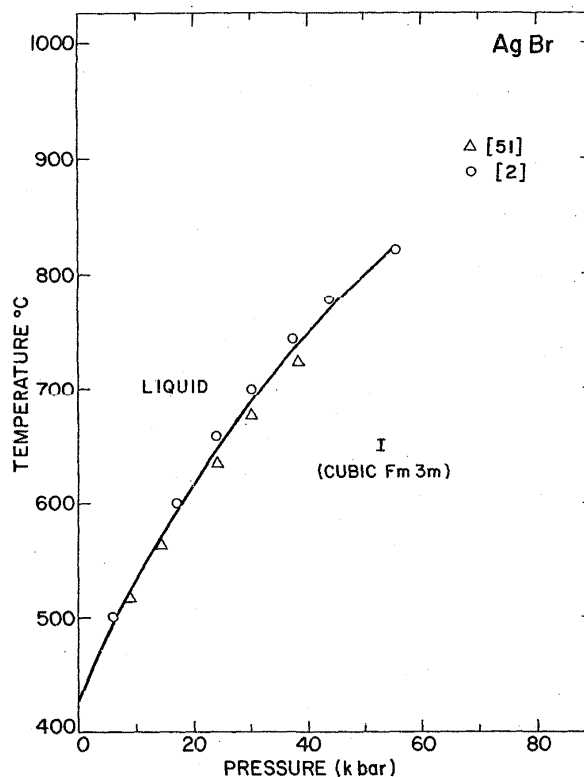


FIGURE 20. Melting curve for silver bromide

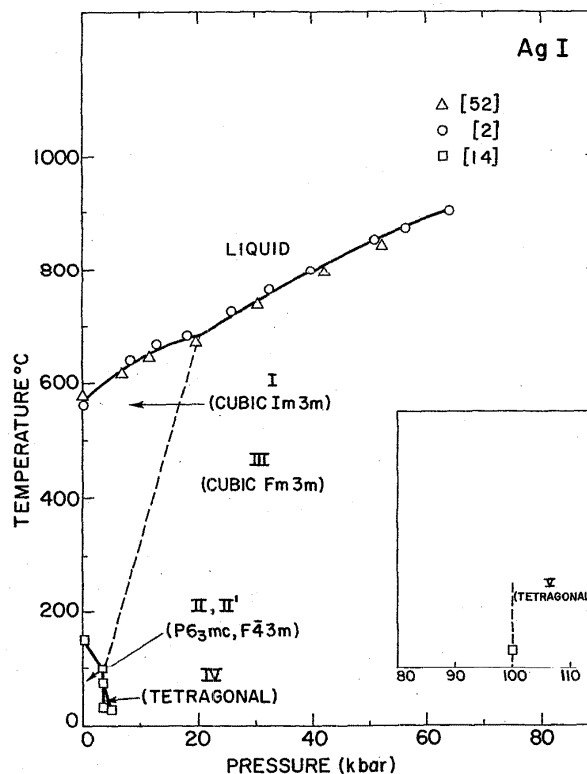


FIGURE 21. Phase diagram for silver iodide

sitions were expected, and none have been observed. The melting curve for TlCl was measured by Pistorius and Clark [165], and the experimental details are identical to those discussed for TlF.

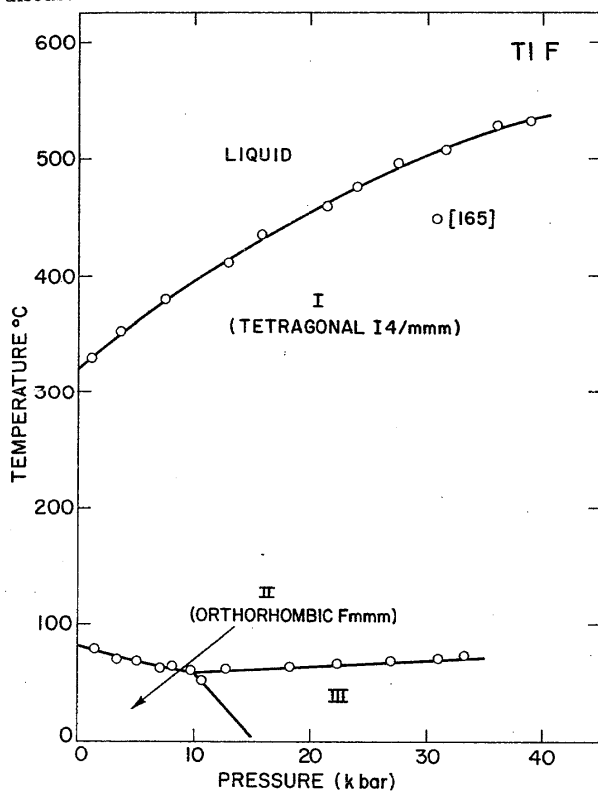


FIGURE 22. Phase diagram for thallium fluoride

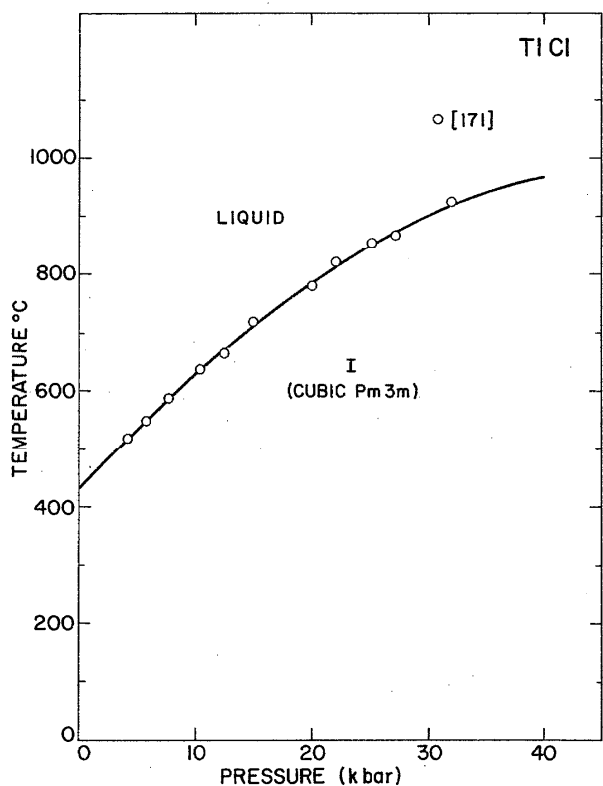


FIGURE 23. Melting curve for thallium chloride

### 10.3. Thallium Bromide

Thallium bromide also crystallizes in the CsCl-type structure and has no known high pressure phases. The melting curve for TlBr was measured by Pistorius and Clark [165]. The experimental details are the same as discussed for TlF.

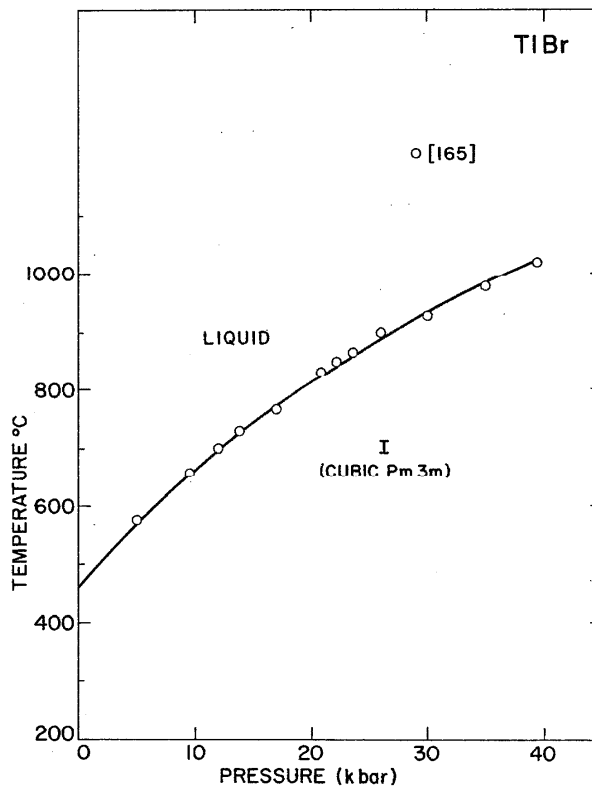


FIGURE 24. Melting curve for thallium bromide

### 10.4. Thallium Iodide

Thallium iodide crystallizes normally in the orthorhombic (*Cmcm*) structure and transforms to a CsCl-type cubic structure, either with increasing pressure or temperature [24]. Measurements of the TII(I)-TII(II) phase boundary were made by monitoring the pressure and temperature dependence of the dielectric constant [179] and the temperature dependence of the isothermal compression [182] curves. The melting curve and phase boundaries of TII were also determined by DTA techniques [165].

## 11. Cyanides

Ionic crystals which consist of spherical cations and rod shaped anions usually undergo phase transitions which involve a change in the orientation of the anions, with one or more phases being disordered. At sufficiently high temperatures, these substances will tend to adopt one of the typically ionic AB-type structures, such as NaCl, due to the large rotational disorder of the anion.

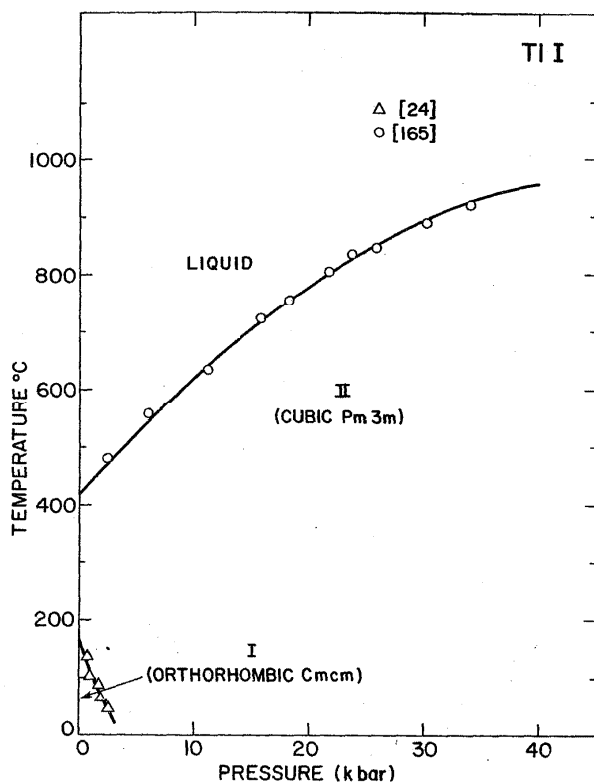


FIGURE 25. Phase diagram for thallium iodide

### 11.1. Cesium Cyanide

The sodium, potassium, and rubidium cyanides are cubic at room temperature 1 bar pressure with space group  $Fm\bar{3}m$ . This structure allows the cyanide ion to be oriented at random along the four body diagonals of the unit cell with a configurational entropy of  $R \ln 8$ .  $CsCN(I)$  at atmospheric pressure and room temperature, belongs to the cubic space group  $Pm\bar{3}m$  and transforms at  $-80^\circ C$  to  $CsCN(II)$  with the rhombohedral space group  $R\bar{3}m$  and has a configurational entropy of  $R \ln 2$ . The  $CsCN(I)$ - $CsCN(II)$  phase boundary was studied up to 35 kbar [168], and the experimental points were fit by the polynomial

$$t(^{\circ}C) = -82.5 + 3.53P - 0.02P^2.$$

### 11.2. Gold Cyanide

The effect of high pressure on the electrical conductivity of  $CuCN$ ,  $AgCN$ , and  $AuCN$  was measured by Bradley et al. [25], using a Bridgman anvil apparatus. The conductivity of  $AuCN$  showed a sharp increase by 5 powers of 10, starting at a pressure of 20 kbar. It is not known whether  $AuCN$  undergoes a polymorphic phase transition or whether it just undergoes a continuous change to the metallic state.

### 11.3. Potassium Cyanide

The polymorphic behavior of  $KCN$  is somewhat similar to  $NaCN$ , although much more complex. There are five known

solid phases up to 40 kilobars. These have been investigated by Pistorius et al. [166], who determined the melting curve and solid-solid phase boundaries by DTA techniques. On the basis of heat capacity measurements [195] at 1 bar, it has been shown that  $KCN$  undergoes two  $\lambda$ -type transitions at low temperature. At 168.3 K, the cubic  $NaCl$  phase transforms to an orthorhombic phase with an entropy change approximately equal to  $R \ln 4$ . By temperature cycling around 168 K, a new monoclinic phase appears, which transforms to orthorhombic by lowering the temperature through 158 K, or transforms directly back to cubic at 166 K. In the region of the  $KCN(I)$ - $KCN(II)$  phase boundary determined by Bridgman [32], the strengths of the DTA signals were weak and erratic, depending upon previous thermal history of the sample [167], consequently, this boundary has not been included in the phase diagram. There are also discrepancies in the literature on the atmospheric pressure  $KCN(I)$ - $KCN(V)$  transition temperature with two values of 212 K [17 and 167] and two others at 168 K [123 and 192], with more recent work favoring the latter point. The second  $\lambda$  transition occurs at 83 K.

The  $KCN(I)$  phase is cubic, of the  $NaCl$ -type, with  $CN$  disorder [64 and 169] which is not yet understood.  $KCN(V)$  is orthorhombic space group  $Imm$ . In this structure, it is suggested that  $CN$  ions lie along a direction closely related to the 110 in the cubic phase [169].

$KCN(III)$  has been investigated by both x-ray diffraction [171] and neutron diffraction studies [56]. It is cubic,  $CsCl$ -type, with disordered  $CN$  orientations randomly distributed over the 8 diagonal configurations [53].

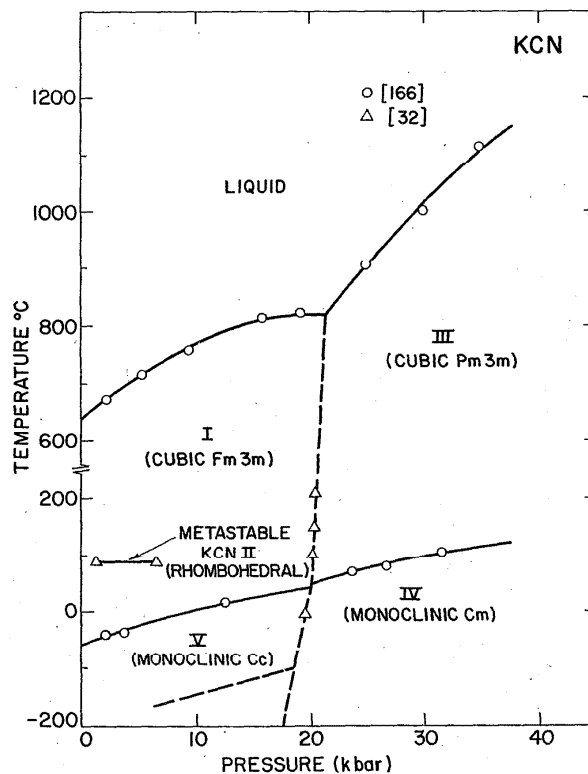


FIGURE 26. Phase diagram for potassium cyanide

KCN(IV) was studied with powder-x-ray-diffraction techniques by Pistorius [79], who assigned it space group  $R\bar{3}m$ , which is a slight distortion of the high temperature KCN(III) CsCl-type phase. A study by Decker et al. [56] using neutron diffraction techniques assigns KCN(IV) as monoclinic space group  $Cm$ . As a result of the greater resolution of the neutron diffraction spectrum, it was shown that the  $d$ -values of several reflections did not fit the rhombohedral structure; also, several intensities did not fit the calculated intensity profile. In KCN(IV), the CN ions are ordered and lie nearly along the body diagonal of a slightly distorted cube of  $K^+$  ions.

#### 11.4. Potassium Thiocyanate

The phase diagram of KSCN has five solid phases up to 40 kbar [166], and is closely analogous to  $KNO_2$ . The original work on this system was by Bridgman [31], who measured the KSCN(I)-KSCN(II) phase boundary up to 4 kbar, and the melting curve to 2 kbar. The results of Bridgman [31] and Pistorius [166] are in excellent agreement.

KSCN(I) is tetragonal space group  $I4/mcm$  ( $d_{4h}^{20}$ ), while KSCN(II) is orthorhombic,  $Pbcm$  ( $D_{2h}^{16}$ ). The structure of the three high temperature high pressure phases have not been determined.

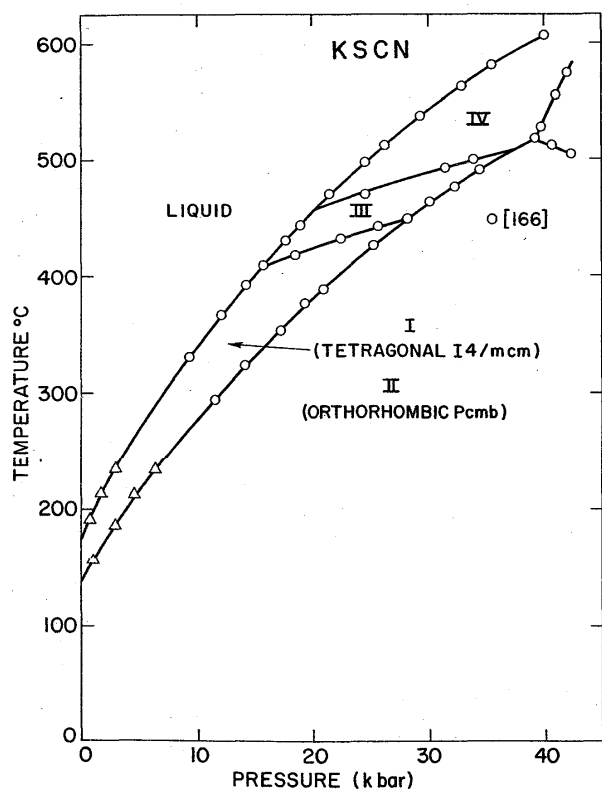


FIGURE 27. Phase diagram for potassium thiocyanate

#### 11.5. Rubidium Cyanide

Rubidium cyanide has a high pressure phase transition at  $5.6 \pm 0.5$  kbar at  $24.5^\circ\text{C}$ , which has been determined by both piston displacement and DTA techniques [44]. The volume

change at the transition is  $2.6 \text{ cm}^3/\text{mol}$  and the slope of the RbCN(I)-RbCN(II) phase boundary is  $dT/dP = 165^\circ\text{C}/\text{kbar}$ . No evidence of an order-disorder transition could be observed in the range of study. RbCN(I) has the NaCl-type structure, and it is assumed RbCN(II) has a CsCl-type structure.

#### 11.6. Silver Cyanide

The high pressure modification of AgCN was discovered by Bridgman [32], who determined three points along the AgCN(I)-AgCN(II) phase boundary, up to  $147^\circ\text{C}$  by dilatometric techniques. A more complete determination of the phase diagram, including the melting curve, was made by Pistorius [156], using a simple piston-cylinder device. Phase transitions were detected by electrical resistance changes. There is no information on the crystal structure of the high pressure phase AgCN(II).

#### 11.7. Sodium Cyanide

At high temperature NaCN adopts a NaCl-type structure, due to the rotational disorder of the anion. At 172.1 K, there is a transition to an orthorhombic form, with space group  $Imm$ ,  $I222$ , or  $Immm$  [164]. The structure below 172.1 K is not known. At 287 K, a first order transition occurs to the NaCl-type cubic structure. Cubic NaCN(I) melts at  $563.7^\circ\text{C}$ . NaSCN has no known polymorphism up to the melting point.

The phase diagrams for NaCN and NaSCN have been studied up to 40 kbar by differential thermal analysis [164]. The melting curves of both substances have been fitted to a Simon curve.

#### 11.8. Sodium Thiocyanate

The crystal structure of NaSCN is orthorhombic [164], with either space group  $Pnma$  ( $D_{2h}^{16}$ ) or its acentric counterpart  $Pn2_1a$  ( $C_{2v}^2$ ). No known high temperature or high pressure solid phases are known to exist for NaSCN.

### 12. Platinum Boride

Platinum boride was first synthesized at atmospheric pressure in alumina crucibles which were inserted in evacuated silica tubes [5]. The powder photograph of PtB suggested the anti-NiAs (B8) type structure space group  $P\bar{6}_3/mmc$ . With this assumption, good agreement between observed and calculated intensities was obtained. The platinum atoms are in special positions  $2(c)$ , while the boron atoms are in  $2(a)$ .

### 13. Carbides

#### 13.1. Molybdenum Carbide

A high pressure polymorph of molybdenum monocarbide [47] was synthesized from an equiatomic mixture of molybdenum and carbon, at pressures and temperatures in the range 40–70 kbar and  $1800^\circ\text{C}$ – $2500^\circ\text{C}$ , respectively.

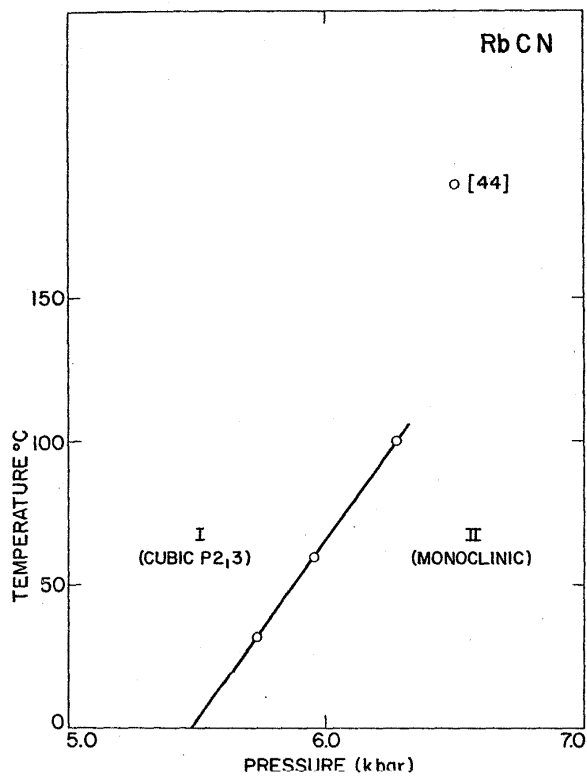


FIGURE 28. Partial phase diagram for rubidium cyanide

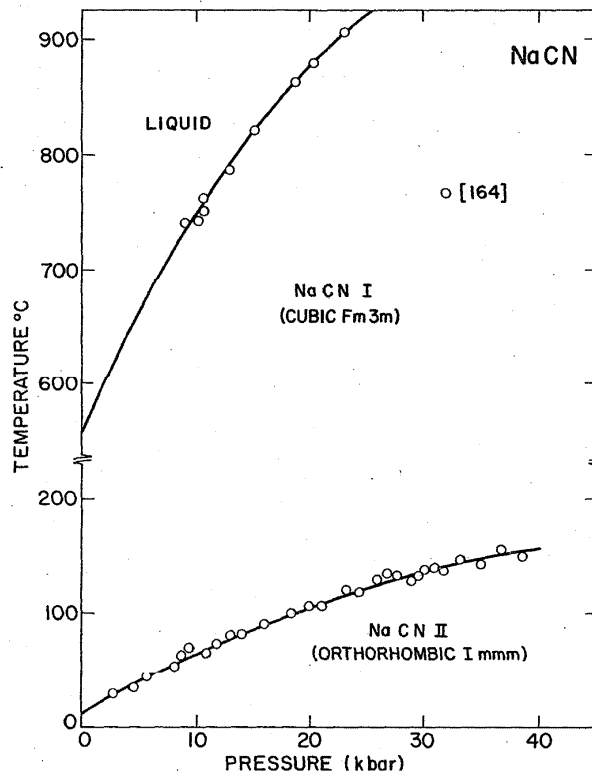


FIGURE 30. Phase diagram for sodium cyanide

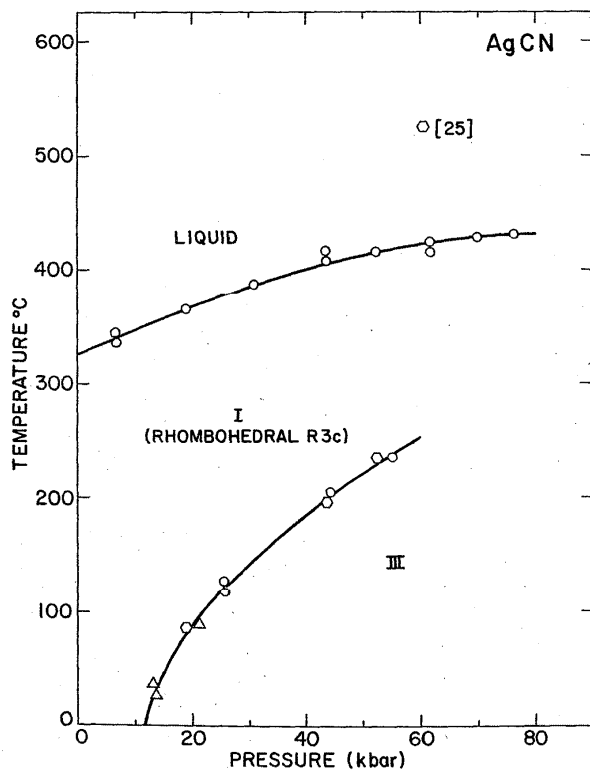


FIGURE 29. Phase diagram for silver cyanide

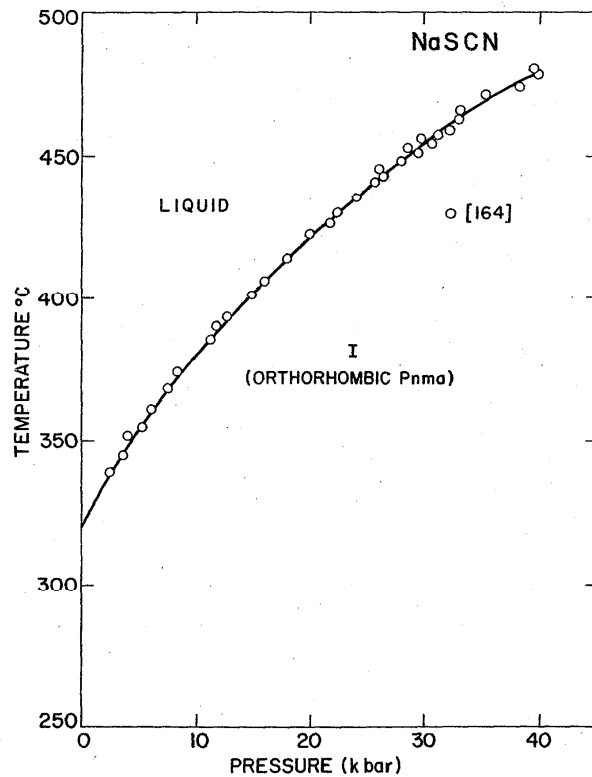


FIGURE 31. Phase diagram for sodium thiocyanate

MoC(II) was retained metastably at atmospheric pressure. An x-ray diffraction examination identified its structure as cubic, space group  $Fm\bar{3}m$  with an average lattice constant  $a=4.27$  Å.

### 13.2. Rhenium Carbide

Rhenium carbide was synthesized at high pressure and high temperature ( $\geq 60$  kbar;  $\geq 800$  °C) by Popova and Boiko [168]. Chemical analysis indicate that it is probably the monocarbide or rhenium. It has the structure of  $\gamma$ -MoC-type, space group  $P6/mmc$  with the following parameters,  $a=2.840$  Å,  $c=9.85$  Å, and  $Z=4$ . At atmospheric pressure, rhenium carbide decomposes at 1500 °C into a rhenium-carbon solution.

## 14. Boron Nitride

The successful synthesis of cubic boron nitride from the hexagonal form was first reported by Wentorf [206]. As a result of the close analogies between the structures of hexagonal BN and graphite, much early work was devoted to the problem of the synthesis of the cubic form, principally along the lines followed for the synthesis of diamond. In the initial attempts, pure boron nitride powder and various mixtures of boron and nitrogen compounds were studied with the diamond forming catalysts. All such experiments produced only the hexagonal form of boron nitride, even at the high temperatures and pressures. The first successful catalyst was magnesium, and further experimental study showed that the alkali metals, and alkaline earth metals and antimony, tin, and lead were successful catalysts [207].

The cubic boron nitride formed with cubic catalysts tended to be black in color with a few clear white crystals occasionally seen. The apparent reason for this was the inclusion of excess boron in the cubic BN, coloring it black. The use of magnesium, lithium, or calcium nitrides as catalysts successfully overcame this problem, while producing high yields of cubic BN at much lower pressures [207].

The behavior of nucleation and growth rates depends primarily on the temperatures and pressures at which the reaction is carried out. For synthesis conditions along the cubic hexagonal equilibrium line, the crystal growth rates are the highest, while at points well away from the equilibrium boundary in the cubic phase, the nucleation rate increases rapidly, resulting in large variations in crystal quality.

The direct conversion of boron nitride was first accomplished by Bundy and Wentorf [38], using a Drickamer type apparatus [6]. When pure boron nitride samples were compressed at room temperature, it was found that a transformation to a more dense phases began at pressures above 125 kbar (106 kbars on NaCl scale). Samples held in this pressure range for several minutes were found to transform to the wurtzite form instead of the zincblende form. At high temperature and high pressures, the region for direct conversion is approximately by  $P > 95$  kbar, and  $T > 2000$  K. In this range, the cubic zincblende phase is formed. There is still insufficient data to establish a phase boundary between the stability regions of the wurtzite and zincblende types. In the direct conversion of these solid phases, the resulting crystallite size is very small, of the order of a micron or less.

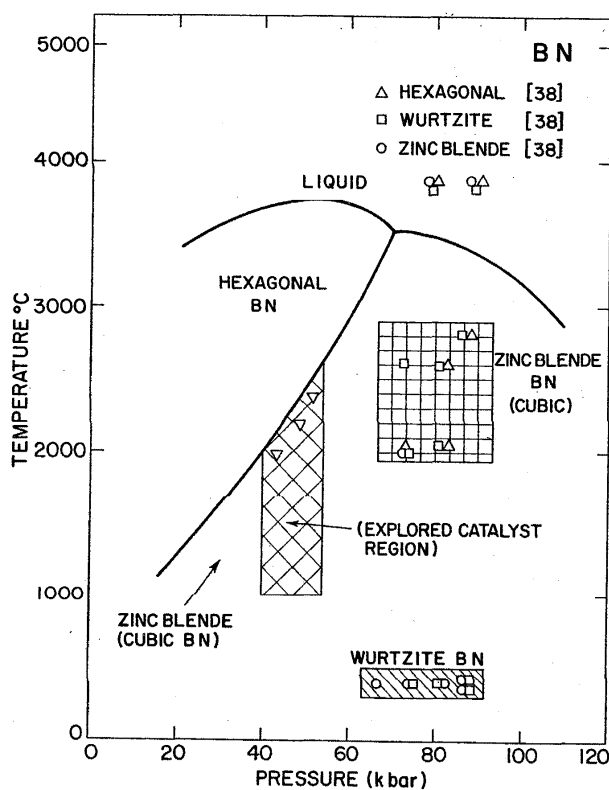


FIGURE 32. Phase diagram for boron nitride

Phase transformation in boron nitride under the action of shock waves was first reported by Al'tshuler et al. [3] and Dremin and Breusov [62]. These two groups obtained very similar shock adiabats with inflections at pressures of 120 and 130 kbar and calculated temperature of approximately 230 °C. The resultant dense phase had the wurtzite like structure.

A critical compilation of the crystallographic, mechanical, optical, electrical, thermal, and thermodynamic properties of BN has been published by De Vries [57]. This review also contains a comprehensive list of references.

In the boron nitride phase diagram, it is not possible to determine equilibrium phase boundaries in the same manner as previously discussed for other systems. Successful synthesis of the high pressure phases occur in the PT regions noted, but the determination of a thermodynamic equilibrium boundary is not possible.

## 15. Phosphides

### 15.1. Boron Phosphide

Boron phosphide is a semiconductor with a band gap of 2eV [4], and high thermal conductivity [23]. The melting point of BP is above 3000 °C, but it decomposes to  $B_6P$  and  $P$  at 1200 °C and 1 bar pressure [98]. As a result, the synthesis of BP is very difficult, since the reaction temperature must be kept below 1200 °C. Successful synthesis of BP crystals can be obtained either from nickel metal solution or from vapor-phase transport reactions, but high purity crystals have not been produced by these methods.

Boron phosphide has been successfully synthesized by high pressure techniques [107] in the pressure-temperature range of 5–25 kbar and 500–2500 °C. The reactants were mixed stoichiometrically, and reacted for 100 minutes. The product was crystalline powder of less than 100  $\mu\text{m}$  diameter. BP, synthesized at 15 kbar and 1500 °C is zincblende-type, with lattice constant  $a=4.54 \text{ \AA}$ , which is the same as reported in the literature [147]. This method results in a significant reduction in impurities over other synthesis techniques.

Van Vechten [201] predicted that BP would undergo a transition to the metallic state at about 400 kbar. Resistivity measurements by Bundy [38a] up to approximately 550 kbar exhibited no unusual behavior.

### 15.2. Gallium Phosphide

In the original studies on GaP, Minomura and Drickamer [126] found no evidence for a phase transition up to a pressure of 420 kbar. Onodera et al. [142] using a double staged split sphere apparatus, were able to detect a discontinuous change in the electrical resistance of GaP by five orders of magnitude. The transition pressure is reported to be in the vicinity of 500 kbar. Masaki et al. [120] adopt the value of 400 kbars, as a temporary value for the transition pressure.

In a study of the Raman scattering in GaP to 128 kbar, Weinstein and Piermarini [203, 203a] found that two of the TA modes were pressure dependent. In extrapolating in frequency of these modes to zero phonon frequency, possible transition pressures of 370 and 400 kbars are obtained. For strong first-order transitions, such as occur in GaP, the frequency of the modes responsible for the phase transition never does go to zero frequency continuously, but becomes unstable at some finite frequency. This would suggest a transition-pressure well below 400 kbar. Piermarini and Block studied the GaP transition pressure using the ruby fluorescence calibration and obtained a value of 220 kbar [151]. Van Vechten [201] calculated a transition pressure of 216 kbar for GaP.

Bundy [38a] noted that the resistance drop of GaP was very sharp and occurs at approximately 240 kbar. Bundy's apparatus is calibrated to the  $\alpha$ - $\epsilon$  transitions points in Fe-V and Fe-Co alloys obtained from shock compression studies by Loree et al. [117a]. Homan et al. [80a] reported a transition pressure "near 220 kbar" for GaP. This value is based upon a calibration which assigns 212 kbar as the transition pressure of Fe-20Co. A better value for the Fe-20Co  $\alpha$ - $\epsilon$  transition is 180 kbar from shock data [117a]. This calibration point would drop Homan's value of the GaP transition from 220 kbar to about 180 kbar. The comparison between the  $\alpha$ - $\epsilon$  transition of the Fe-Co alloys and the NaCl scale has not been determined, so it is not possible to comment on this low value for the GaP transition pressure. It is, however, in poor agreement with the result of Bundy [38a].

### 15.3. Germanium Phosphide

The reaction of germanium and phosphorous yielded a tetragonal phase of GeP [69]. The synthesis was carried out at 800 °C and 65 kbar, followed by 3 hours of cooling to 400

°C and quenched. The product contained four regions. Black crystals on the end showed a  $\text{GeP}_3$ -type pattern. In the center, there was an unidentified, poorly crystallized phase with excess Ge. In between the central and end region, large black crystals were present, which could be indexed on the basis of a tetragonal cell with  $a=3.544 \text{ \AA}$  and  $c=5.581 \text{ \AA}$ . The most probable space group is  $I4mm$  and the measured and calculated density are  $4.73 \text{ g/cm}^3$  and  $4.90 \text{ g/cm}^3$ , respectively.

Electrical measurements on a single crystal show metallic conductivity and Meissner effect measurements show a superconducting transition between 1.5 and 4.2 K.

### 15.4. Indium Phosphide

The high pressure polymorphic transition in indium phosphide InP was first studied by electrical resistance techniques [126]. At approximately 130 kbar, a sharp discontinuity of several orders of magnitude was observed in the electrical resistance trace. The crystal structure of the new high pressure form is NaCl-type with  $a=5.514 \text{ \AA}$  [85], while the atmospheric pressure form has the zincblende structure.

### 15.5. Silicon Phosphide

A form of SiP with the zincblende structure was synthesized in the region 1700–1800 °C and 40 kbar [143]. X-ray analysis at atmospheric pressure and room temperature gives the unit cell dimension  $a=5.241 \text{ \AA}$  and a calculated density  $\rho_c=2.73 \text{ g/cm}^3$ .

### 15.6. Tin Phosphide

Under ordinary atmospheric-pressure room-temperature conditions, tin phosphide crystallizes in a hexagonal structure [105]. Osugi et al. [144] report the formation of a sphalerite phase of SnP at 1600–1800 °C and 40–50 kbar. In a similar study, Donahue [58] reported the synthesis of two high-pressure polymorphs in a reaction at 1200 °C and 65 kbar, as well as 900 °C and 15 kbar. In each case, there were two phases present, a major tetragonal phase and a minor cubic phase. The cubic phase was indexed as NaCl-type on the basis of the intensity data. The unit cell dimension is  $a=5.535 \pm 0.0001 \text{ \AA}$ .

It is not clear which high-pressure phase of SnP is the more stable at 65 kbar. When mixtures of the two phases are heated in air between 100–200 °C, the tetragonal phase reverts to the cubic phase. The calculated density of the cubic phase is  $5.86 \text{ g/cm}^3$ , while that of tetragonal SnP is  $5.68 \text{ g/cm}^3$ . One would expect the more dense cubic phase to have a higher stability region. Part of the cubic phase may revert to tetragonal, upon quenching. The transformation from cubic to tetragonal upon heating at 1 bar is unusual since it involves a transformation to a more dense structure.

Both SnP(II) (Tetragonal phase) and SnP(III) (cubic phase) are metallic conductors. The cubic form SnP(III) is superconducting, with a transition temperature between 2.8 and 4.8 K.

The crystal structure of the tetragonal-phase was shown to be similar to that of high pressure GeP and GeAs. The structure is closely related to the NaCl type by a small displace-

ment of atoms. If the diagonal in the basal plane equalled the  $c$  axis and  $z=0.5$ , the structure would be NaCl-type. The atoms are in a distorted octahedral arrangement. The powder pattern could be indexed with unit cell dimensions  $a=3.831\pm 0.001$  Å and  $c=5.963\pm 0.001$  Å.

## 16. Oxides

### 16.1. Barium Oxide

The physical properties of the alkaline earth oxide, MgO and CaO are of interest to geophysicists, since it has been suggested that the simple oxides may be prevalent in the earth's lower mantle. Since there are no known high pressure phases of MgO and CaO in the static pressure domain, it was thought that a study of BaO under pressure might shed light on the behavior of the other members of this group.

The oxides of the alkaline earth metals (Mg, Ca, Sr, Ba) crystallize in the NaCl-type structure. BaO was selected for this experiment, since it would be expected the member of the series with the greatest cation/anion radius ratio would transform at the lowest pressure.

The first evidence of a high pressure phase was from optical observations of a sample under pressure [114]. Further examination of this phase, BaO(III) by x-ray diffraction indicates that it is tetragonal with the  $PH_4I$ -type structure. The lattice constants are  $a=4.397$  Å and  $c=3.196$  Å at 180 kbar. The intensities are compatible with space group  $P4/nmm$  with oxygen atoms in special positions  $2(a)$  and barium atoms in  $2(c)$ . The  $PH_4I$ -type structure is a distorted CsCl-type structure. The BaO(III) phase persists from 140 kbar up to 290 kbars, which is the maximum pressure of the study.

A study of BaO in the pressure range of 90–180 kbar has revealed an intermediate crystal structure, BaO(II). The x-ray pattern of this phase can be indexed as tetragonal with lattice parameters  $a=4.549$  and  $c=3.606$  at 100 kbar [116]. A structure type for this phase is not known.

The BaO(I)-BaO(II) and BaO(II)-BaO(III) transitions occur at a pressure of  $92\pm 3$  kbar and  $140\pm 5$  kbar, respectively. The transitions are reversible with volume changes of approximately 5 and 7%. Pressures were determined from compression measurements of Ag mixed with BaO as an internal standard. No points in the high temperature region of the BaO phase diagram have been determined.

### 16.2. Europium Oxide

In a study of the pressure-volume relationship of europium oxide, by x-ray diffraction techniques, two pressure induced transitions were detected in the region of 300 kbar and 400 kbar, respectively [88]. The first transition at 300 kbar is a collapse of the NaCl-type structure to NaCl. Within a narrow pressure interval, the pressure drops, rather abruptly, by about 4%, suggesting the transition may be of first order. The transition is attributed to an electronic collapse in the Eu ion, involving the promotion of a  $4f$  electron to the  $5d$  state, resulting in a change in valence to the trivalent state. It is assumed that this transition is from the semiconductor to the metallic state, similar to the pressure transitions in the rare earth monochalcogenides.

Near 400 kbar, the EuO(II) phase transforms to the cesium chloride structure. The volume change at this latter transition is 6.6%. The total compression of EuO, up to 400 kbar, is approximately 31% of the original volume.

Pressure calibration was performed to 400 kbar with silver as an internal standard. Pressures were computed from the data of Liu and Bassett [116], who compared Ag compression with the NaCl scale up to 300 kbar. The bulk modulus  $B_e=1130$  kbar and its pressure derivative  $B_e'=3.75$  were used in the Birch equation to extrapolate the pressure scale above 300 kbar. The uncertainties in pressure are  $\pm 20$  kbar above 300 kbar and  $\pm 10$  kbar below 300 kbar.

### 16.3. Iron Oxide (Wustite)

Stoichiometric  $Fe_{1.0}O$  was synthesized at high pressure above 36 kbar at 770 °C, by a reaction between  $FeO_{.95}$  (Wustite) and metallic iron [104]. The cell dimension of wustite is approximately 4.312 Å, while  $FeO$  is 4.323 Å. Silicon powder was used as a standard in determining the x-ray diffraction line positions.

### 16.4. Sodium Hydroxide

The phase diagram of sodium hydroxide is closely related to the alkali cyanides. At high temperatures, these structures tend to adopt the ionic AB-type structure, due to the large rotational disorder of the anion. The low temperature 1 bar form of NaOH(II) has an unusual structure. It is orthorhombic,  $Cmcm$  with an average coordination of 7, and the structure is a distorted compromise between NaCl and CsCl types.

The phase diagram of NaOH was studied to 40 kbar by means of differential thermal analysis and volume displacement [160]. A new high pressure phase NaOH(IV) appears at 8.4 kbar. The NaOH(II)-NaOH(I) transition splits into two transitions above 0.8 kbar, resulting in phase boundaries with abnormal curvature. The structures of the high-temperature high-pressure phases III, IV, and V are not known.

### 16.5. Strontium Oxide

The x-ray diffraction patterns of SrO are consistent with the NaCl-type structure up to 70 kbar at 23 °C. At pressures from 70 to approximately 307 kbar, there is a splitting of some of the diffraction lines [117], consistent with a tetragonal indexing. Volumes calculated on the basis of this indexing show no discontinuity at the phase boundary within experimental error. The tetragonal lattice parameters of SrO(II) at 175 kbar are  $a=4.912$  Å and  $c=4.949$  Å.

An unusual feature of this experiment was that at a pressure above 307 kbars, the tetragonal splitting disappeared and the cubic symmetry reappeared. The authors stated that a re-examination of BaO powder patterns showed some evidence for this splitting at pressures just below the phase transformation to BaO(II).

As in the case of BaO, all pressures were determined from the compression of Ag, which was mixed with SrO as an internal standard.

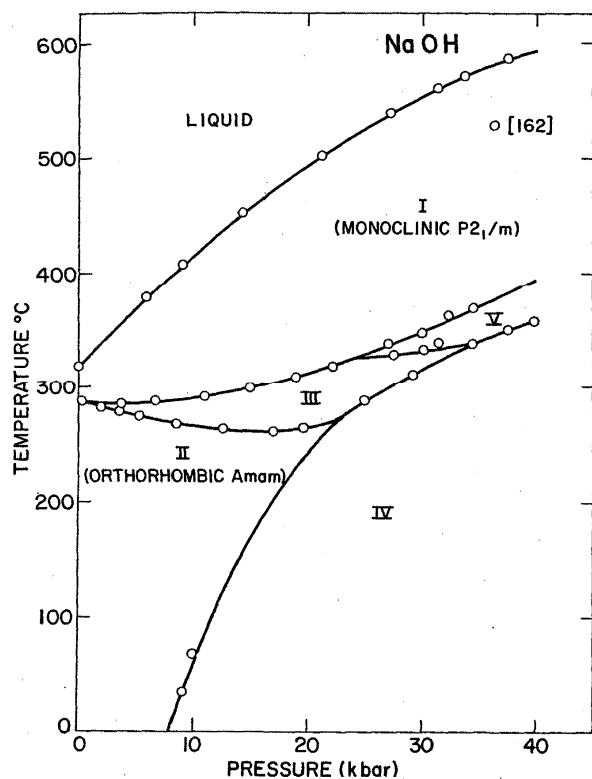


FIGURE 33. Phase diagram for sodium hydroxide

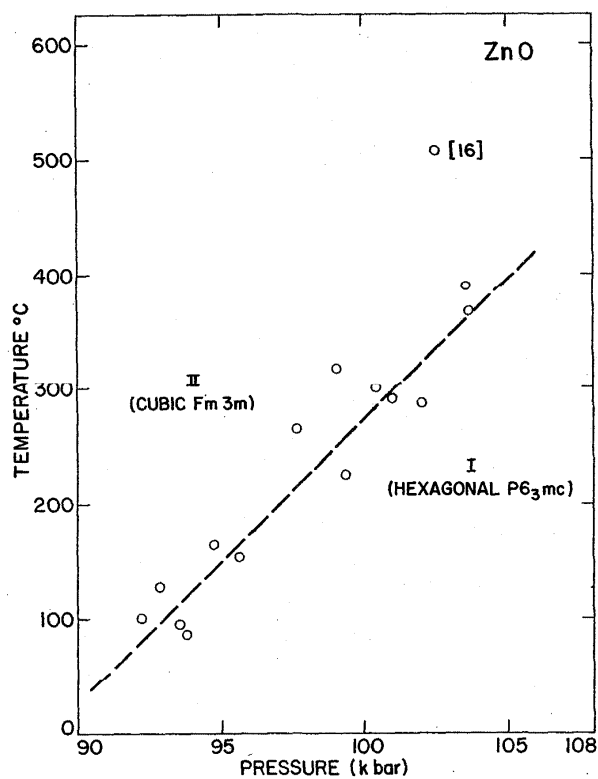


FIGURE 34. Partial phase diagram for zinc oxide

### 16.6. Tin Oxide

Under ordinary conditions, tin oxide has the tetragonal PbO-type structure, space group  $P4/nmm$ . At approximately 40 kbar, SnO undergoes a reversible polymorphic phase transition with a 7% volume change [204]. X-ray diffraction patterns of SnO(II) taken at 60 kbar can be indexed as wurtzite-type with  $a=3.42\pm 0.02 \text{ \AA}$ ,  $c=5.62\pm 0.04 \text{ \AA}$ , and  $Z=2$ . The  $c/a$  ratio of SnO(I) decreases with increasing pressure up to the transition.

### 16.7. Zinc Oxide

Zinc oxide, which has the hexagonal wurtzite-type structure at room temperature and pressure, transforms to a NaCl-type phase in the region of 100 kbar and 200 °C [16]. The crystal structure of the high-pressure phase of ZnO was identified by its x-ray powder pattern. Conversion to this phase could be accomplished only with ammonium chloride as a catalyst. The rate of conversion was slow, and usually 36 to 48 hours reaction time was required to produce an appreciable amount of the new phase (30 percent).

ZnO(II) showed no tendency to revert to the wurtzite phase after standing several weeks at room temperature. However, it does revert to the wurtzite form at a temperature of 120 °C in 3 weeks time. There is insufficient experimental data to present a reliable phase boundary.

## 17. Sulfides

### 17.1. Cadmium Sulfide

Cadmium sulfide commonly occurs in two modifications, one having the wurtzite structure, which is the stable form, and the other form has the sphalerite structure. The sphalerite phase can be derived from the wurtzite, by the application of a shear stress, for example, by grinding it in a mortar. In the structure change, the material changes color from yellow to red.

The pressure-induced phase transition in cadmium sulfide was first discovered by Drickamer [64, 65], who noted a shift in absorption-edge spectrum towards the longer wavelength region.

A single determination of the melting curve of CdS up to 50 bars has been reported [136]. At this pressure, CdS melted at 1370 °C measured by W:5Re-W:26Re thermocouples. The pressure medium was Argon.

Numerous x-ray studies of CdS [49, 68, 98, 118, 146] have confirmed the high pressure structure as cubic NaCl-type. Most of these studies were performed in situ, while in two, it was possible to recover the high pressure phases at low temperature and x-ray then at atmospheric pressure [68, 146], confirming the high-pressure results. There is a 24% volume change associated with the CdS wurtzite-to-NaCl phase transition. Lattice parameters have been measured up to 90 kbar.

In most instances, no serious attempt was made to calibrate

the CdS(I)-CdS(II) transition pressure, due to the extreme sluggishness of the transition. Kaminskii et al. [101] measured the hysteresis associated with the transition, and made an approximation of the CdS(I)-CdS(II) phase boundary up to approximately 500 °C, where the width of the hysteresis was only 4 kbar wide. The phase boundary was approximated by selecting the midpoint of the hysteresis interval and extrapolated to atmospheric pressure.

### 17.2. Iron Sulfide

Troilite is the polymorph of FeS stable below the transition that occurs at 140 °C at 1 bar and has the NiAs-type structure. Above 140 °C, hexagonal pyrrhotite with the hexagonal B-8 structure is the stable phase. The original differential thermal analysis data [111] on the boundary of the troilite phase up to pressures of 19 kbars indicated that the transition temperature lowered with pressure by 2.2 °C/kbar. Calculations of the slope on the basis of Taylor's [194] value of the volume change at 1 bar and  $\Delta H$  from Robie and Waldbaum [173] predict a positive value of  $dP/dT=2.3$  °C/kbar. It was suggested that this discrepancy could be explained by the presence of a new high pressure polymorph of FeS [197].

X-ray diffraction patterns and optical observations by Taylor and Mao [198] indicate that there is a new high temperature high-pressure polymorph between the Troilite and pyrrhotite phases. X-ray diffraction patterns at  $120 \pm 40$  kbar at 22 °C and  $50 \pm 20$  kbar at 30 °C have been published, but could not be indexed [198]. The room-temperature phase transition from Troilite to the new high-pressure form occurs at approximately 55 kbar. This transformation is very rapid, and the high-pressure phase could not be quenched by the techniques employed.

### 17.3. Lead Sulfide

Lead sulfide transforms from the NaCl type structure to an orthorhombic structure with space group  $Pnma$ , at approximately 25 kbar [118]. The PbS(I)-PbS(II) transformation is very sluggish, and no further attempt has been made to determine its transition pressure.

### 17.4. Mercury Sulfide

A phase transition in HgS, from the zincblende structure to the cinnabar [119] structure was induced by high pressure, using a diamond anvil pressure cell. The high pressure phase was characterized by x-ray diffraction techniques. No attempt was made to accurately determine the transition pressure.

### 17.5. Nickel Sulfide

NiS [79] is metallic above its Neel temperature ( $T_N=230$ K) and antiferromagnetic below, as opposed to NiO, which is an insulator, both above and below  $T_N$  [188]. At the transition, there is a discontinuous increase in both the lattice parameters of the hexagonal NiAs structure [190] and an increase in the electrical resistance by a factor of 50. The temperature coefficient of resistivity is negative, just below  $T_N$ .

The crystal structure of the antiferromagnetic phase is not

known. It is assumed that in the phase transition the NiAs structure  $P6_3/mmc$  ( $D_{6h}^4$ ) loses its center of symmetry, transforming to  $P6_3mc$  ( $C_{6v}^3$ ). Low temperature x-ray diffraction experiments, however, cannot distinguish between the centric and acentric models.

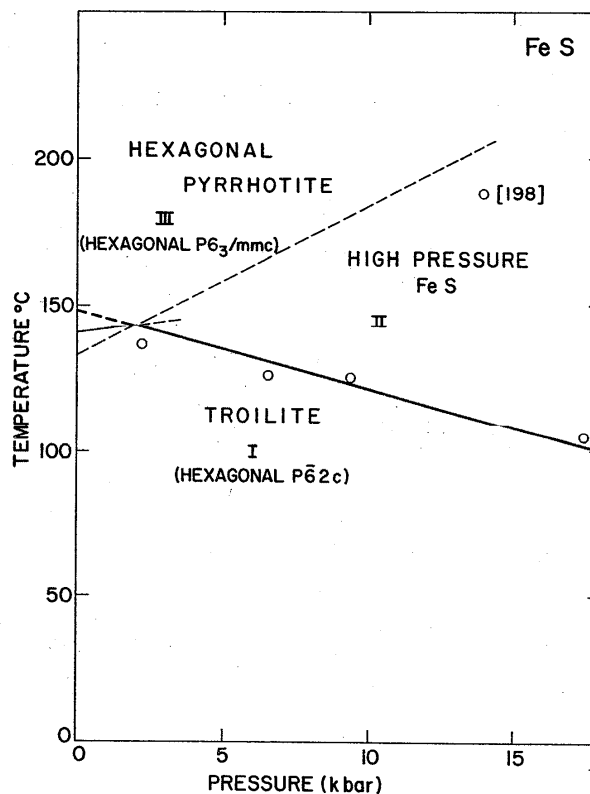


FIGURE 35. Partial phase diagram for iron sulfide

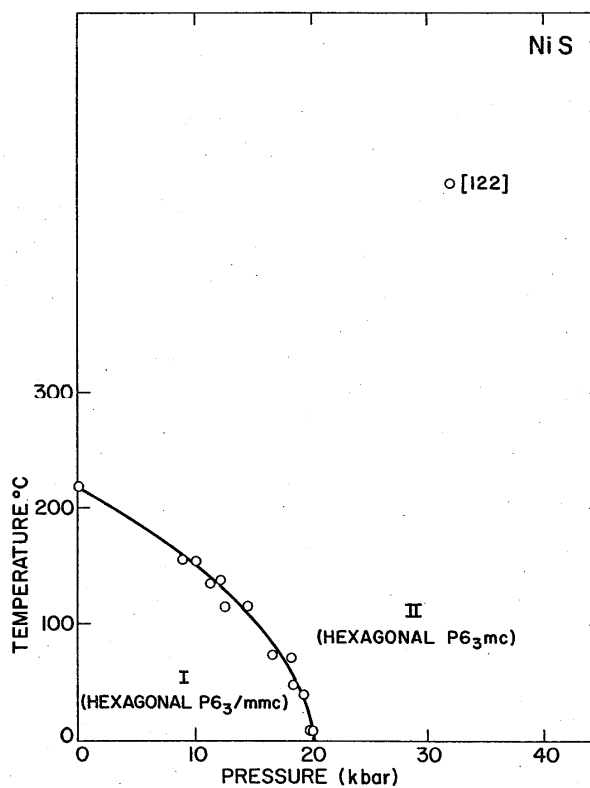


FIGURE 36. Partial phase diagram for nickel sulfide

### 17.6. Samarium Sulfide

Samarium sulfide undergoes a discontinuous semiconductor-metal transition at approximate pressure of 6.5 kbar [91]. Both the resistivity and the lattice constant abruptly decrease at the transition pressure without any change in crystal structure. The transition is associated with the promotion of a 4*f* electron in the 5*d* band, changing the valence from Sm<sup>2+</sup> to Sm<sup>3+</sup> [89]. The crystal structure is NaCl type on both sides of the transition, and the volume change is approximately 24%. Measurements of the slope of the phase boundary indicates a high negative *dT/dP*. At the transition, the lattice constant changes from *a*=5.97 Å to *a*=5.70 Å in the high pressure collapsed phase.

Since the lattice constant of GdS (5.563 Å) is substantially smaller than that of SmS (5.97 Å), Gd substitution may be expected to have the same effect as applying pressure. Jayaraman et al. [89] found that Gd substitution lowers the transition pressure and that concentrations in excess of 15 atomic percent Gd stabilizes the collapsed metallic phase at atmospheric pressure. The lattice parameter decreases abruptly to 5.68 Å near this concentration.

Samples which have Gd concentrations greater than 15 atomic percent, exhibit a golden-yellow metallic reflectivity. Samples whose concentration lies between 15 and 22 atomic percent undergo a temperature induced first order transition at low temperatures.

### 17.7. Zinc Sulfide

On the basis of room-temperature high-pressure electrical-resistance measurements, ZnS undergoes two pressure-induced polymorphic phase transitions [120, 181]. The reported pressures of these transitions based upon Drickamer's revised values are 185 kbar and 420 kbar [120]. On the basis of the ruby fluorescence technique Piermarini and Block [151] obtained a value of 150±5 kbar for the lower ZnS transition. The transition was detected visually by the appearance of an opaque phase. Yagi and Akimoto [210a] determined a transition pressure of 162±4 kbar for the ZnS transition. The pressure was detected by measurement of the electrical resistance of the sample. At the transition point, the pressure was calculated from the x-ray powder patterns of NaCl based on Decker's equation of state. In order to compare these two values it would be necessary to also know the transition pressure at which ZnS(II) reverts to its normal phase. The transition pressure in ZnS may be affected significantly by nonhydrostatic stresses.

## 18. Antimonides

### 18.1. Gallium Antimonide and Aluminum Antimonide

Pressure-induced phase transformations were first detected in GaSb and AlSb by discontinuities in the electrical resistance [126], and were reported to occur in the pressure range 80–100 kbar and 115–125 kbar, respectively. The large discontinuity in electrical resistance is suggestive of a change from semiconductor to metallic behavior. Both of these compounds have the zincblende structure at 1 bar which changes

to the tetragonal white tin type structure at high pressure [102]. These results are based upon an x-ray examination of the samples under pressure. The original determinations of the transition pressure are upstroke values and the pressures are high, since these materials are very sluggish. In a later work, Drickamer [63] has revised his original scale downward, which would correct the reported values for GaSb to 60–80 kbar and AlSb to 90–105 kbar. The equilibrium values may be even lower.

### 18.2. Indium Antimonide

Considerable attention has been given to the nature of the high pressure phases of indium antimonide, and it has required fairly extensive investigation to arrive at a characterization which is consistent with the varied experimental results. The transition under pressure to a phase showing metallic conductivity was first found to Gebbie et al. [73], employing electrical resistance measurements. The observation of a resistance drops of several order of magnitude led Drickamer [63] to assume that the transition was one from the semiconducting to the metallic state.

A phase diagram was initially worked out by Jayaraman et al. [92], which illustrated the details of the melting curve and InSb(I)-InSb(II) phase boundary. It was also suggested in this work that the high pressure phase of InSb possessed the tetragonal white tin structure, since tin lies between indium and antimony in the periodic table, and InSb at atmospheric pressure has the zincblende structure analogous to the diamond structure of grey tin. This assumption was later confirmed by Smith and Martin [183], who performed an x-ray analysis of InSb at high pressure.

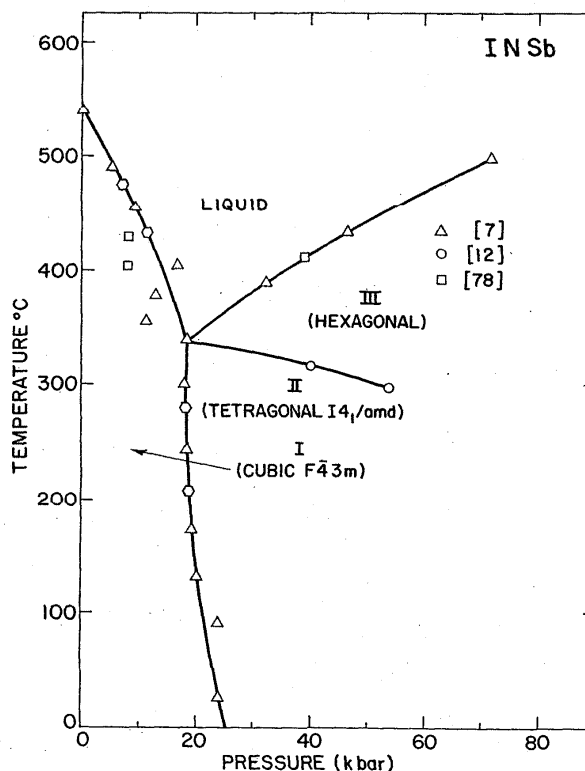


FIGURE 37. Phase diagram for indium antimonide

Several subsequent x-ray examinations of InSb at high pressure gave results which indicated that the high pressure region was much more complex than a single phase. Rooymans [176] proposed that InSb(II) had the rock salt structure [7, 11, 85, 103, 183]. This structure is also retained in quenching experiments at low temperature upon the release of pressure.

The first evidence for additional phases in the InSb system was presented in the work of Kasper and Brandhorst [103]. In most of their experiments at 30 kbar and room temperature, they observed a pattern consistent with an orthorhombic unit cell with only two atoms placed at 000 and  $0\frac{1}{2}\frac{1}{2}$ . Occasionally, they obtained a few lines of a pattern analogous to the Beta-Sn phase. In a later work, Banus and Levine [10, 11] found evidence of a high-temperature high-pressure transformation in the neighborhood of 37 kbar and 300 °C designated InSb(III), giving evidence for at least for at least three distinct high-pressure phases.

The results of superconductivity measurements, x-ray diffraction experiments, and electrical resistance measurements were used to obtain an overall picture of the phase diagram.

Minomura et al. [128] observed a phase transition by electrical resistance at 80 kbar, and McWhan et al. [121] detected a change from the Beta-tin phase to the orthorhombic phase at 60 kbar. Geller et al. [75] reported a superconducting temperature of  $T=2.1$  K for the Beta-tin phase, InSb(II) and McWhan et al. [135] reported a  $T=3.4$  K for the orthorhombic phase, InSb(IV). They also found that the average  $T_c$  for InSb samples was 4.1 K.

The kinetics of the InSb(I) InSb(II) phase boundary was studied by Omel'chenko et al. [139] in a hydrostatic system and the phase-transition pressure at 23 °C is 24.6 kbar. This figure is based upon an extrapolation of the mean of the upstroke and downstroke transition pressure in the range 100–300 °C.

## 19. Arsenides

### 19.1. Boron Arsenide

Boron arsenide BAs is very difficult to synthesize in the pure form at atmospheric pressure [209]. Under high temperature high-pressure conditions, however, both BAs and  $B_{13}As_2$  are formed. The crystals of BAs have the cubic zincblende structure with a lattice constant of 4.777 Å, while  $B_{13}As$  has a rhombohedral structure with lattice constant 5.319 Å and  $\alpha=70.5^\circ$ . The optimum conditions for the formation of BAs are a pressure of 2–3 kbar and 1300 °C [143]. BAs, which is the dense form, was produced under a lower pressure than the  $B_{13}As$  product. It is expected that at some pressure, probably above 50 kbar, the transformation to BAs will predominate.

### 19.2. Gallium Arsenide and Indium Arsenide

The polymorphic transitions in GaAs and InAs were first detected by electrical resistance measurements [126]. In GaAs the transition occurs in the range 185–190 kbar, and is associated with a large decrease in the resistance by a factor

of  $10^4$ – $10^5$ . The resistance levels off for about 10 kbar beyond this point, and then again drops sharply by a factor of about 10–20. In indium arsenide, there is a single discontinuity in the electrical resistance with a decrease in resistance by a factor of  $10^6$ . In both of these arsenides, the transformation is undoubtedly from the semiconducting to the metallic state.

X-ray examination [85] has been successfully carried out for InAs. It transforms from the zincblende structure at atmospheric pressure to the NaCl-type structure above 100 kbar. The NaCl phase has a lattice constant  $a=5.514$  Å, but the pressure is not known accurately. The GaAs semiconductor metal transition was studied by Yagi and Akimoto [210a] using X-ray diffraction techniques. The transition was determined by electrical resistance measurements and pressure determined by the lattice spacing of NaCl. The transition pressure was determined at  $193\pm 5$  kbar. Van Vechten [201] calculated a value of 153 kbar for this transformation.

### 19.3. Germanium Arsenide

Germanium arsenide, GeAs, was synthesized from the reaction of Ge+3As at 900 °C and 65 kbar [60]. The product was a multiphase sample of which x-ray powder patterns of the central region could be indexed on the basis of a tetragonal cell similar to that of GeP. The unit cell dimensions of tetragonal GeAs are  $a=3.712$  Å and  $c=5.832$  Å with  $Z=2$ . The measured and calculated densities are 6.06 g/cm<sup>3</sup> and 6.10 g/cm<sup>3</sup>, respectively.

Crystals of GeAs show metallic conductivity and Meissner-effect measurements show a superconducting transition between 3 and 3.5K.

### 19.4. Manganese Arsenide

At atmospheric pressure, hexagonal NiAs-type (B8) MnAs undergoes a first-order transition at the ferromagnetic Curie temperature  $T=44$  °C to the orthorhombic MnP-type (B31) structure. At 127 °C, there is a second order B31–B8 transition. The B31 structure is derived from the B8 structure by a displacement of the manganese atoms out of the center of symmetry of the arsenide interstices [77].

The pressure dependence of  $T_c$  has a negative slope for increasing pressures up to 4.6 kbar above which the B31 phase is stable at all temperatures down to absolute zero. There is a very large hysteresis associated with the first order B31–B8 transition which obscures the true thermodynamic equilibrium transition pressure. Below  $-134$  °C, the B31 phase can be retained metastably at atmospheric pressure.

## 20. Selenides

### 20.1. Cadmium Selenide

Cadmium selenide occurs under normal conditions in two modifications, one having the hexagonal wurtzite structure, and the other having the cubic zincblende structure, the former being the more commonly observed structure. It has been shown by optical absorption spectra [64], electrical resistance [128, 175], and volume measurements [46, 90], that

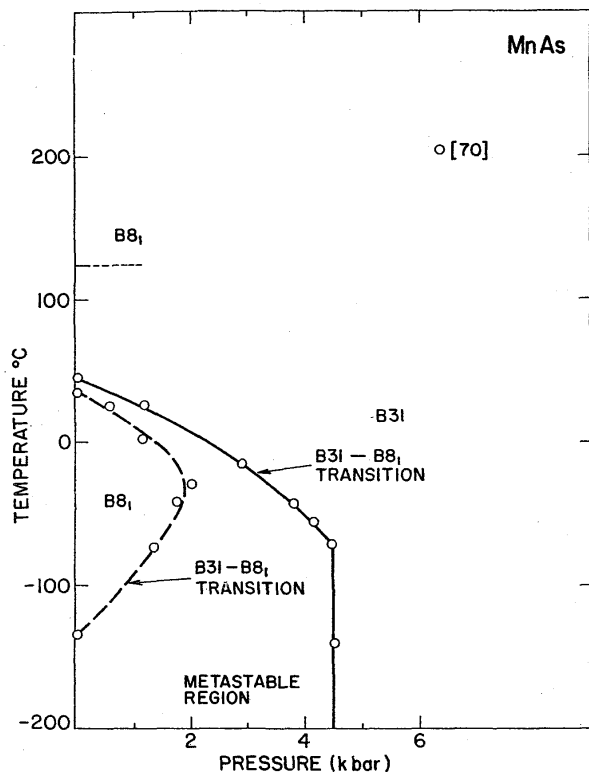


FIGURE 38. Partial phase diagram for manganese arsenide

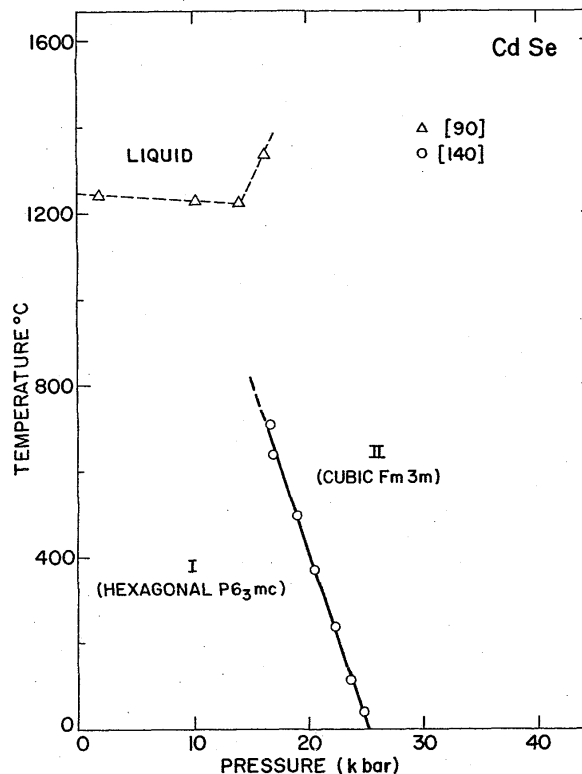


FIGURE 39. Partial phase diagram for cadmium selenide

CdSe undergoes a phase transition in the region 20–30 kbar. There is a large discontinuous red shift in the optical-absorption edge, and a corresponding decrease by several orders of magnitude in the electrical conductivity. Jayaraman et al. [90] reported a volume decrease of about 9% at the transition, while Cline and Stevens [46] reported about 16% on a single-crystal sample.

Melting experiments were carried out by Jayaraman et al. [90], and the melting curve is nearly flat up to the triple point at  $13 \pm 1$  kbar and 1252 °C. Melting was detected by DTA and temperatures were measured with chromel-alumel thermocouples. Due to problems of deterioration of the thermocouples, only a few data were successfully obtained above 1100–1200 °C.

The CdSe(I)-CdSe(II) solid-solid phase boundary was investigated by the volume discontinuity method [140], and by the electrical resistance behavior [90], giving room temperature transition pressures of 24.7 and 23 kbars, respectively. Other reported values of the transition are 34 kbar by Mimomura et al. [128], 23 kbar by Rooymans [175], 21.3 kbar by Cline and Stevens [46], and 27 kbar by Edwards and Drickamer [64]. The best value for this transition is taken as 25.4 kbar, the average of the above values.

X-ray examination of the CdSe(II) has been reported by Rooymans [175] and Mariano et al. [118]. The transition is from the wurtzite B4 type structure to the NaCl-B1 type structure with a lattice constant of 5.49 Å at approximately 32 kbar.

## 20.2. Indium Selenide

The normal form of InSe is hexagonal  $P6_1/mmc$  ( $D_{6h}^{2d}$ ) with lattice constants  $a=4.05$  Å and  $c=16.93$  Å. InSe(II) has been synthesized at about 40 kbar and 520 °C, producing a polycrystalline product [202]. The diffraction patterns have been published, but could not be indexed. This may suggest a mixture of phases present.

## 20.3. Lead Selenide

Lead selenide, which crystallizes in the NaCl-type structure, transforms sluggishly to the orthorhombic  $Pnma$  structure at approximately 42 kbar. This transition has been studied by volumetric methods [140] and electrical resistivity measurements. The volume change at the transition is from one to two percent. The determination of the crystal structure of PbSe(II) was from powder x-ray diffraction studies [118] employing a diamond-anvil pressure device.

## 20.4. Manganese Selenide

MnS and MnSe both crystallize in the NaCl-type structure at room temperature and atmospheric pressure, while MnTe has the NiAs-type structure. X-ray-diffraction experiments at high pressure [42] confirm a high-pressure modification of MnSe to the NiAs type modification. X-ray data at 90 kbar and room temperature give the hexagonal unit cell dimensions  $a=3.63$  Å and  $c=5.9$  Å.

### 20.5. Mercury Selenide

The HgSe(I)-HgSe(II) transition was first studied by Bridgman [34], who detected a sharp change in the compressibility near 7.5 kbar. He suggested that this transition corresponded to a change in crystal structure from the cubic zincblende form to the hexagonal form of HgS.

The transition was also studied by the measurement of electrical resistance which was observed to increase discontinuously by 6 orders of magnitude [100] in the region above 7.5 kbar. When the high-pressure phase was cooled below 170 K it could be retained metastably upon release of the pressure. X-ray examination of this phase confirmed that HgSe(II) adopts the hexagonal cinnabar-type structure. This structure is further confirmed by Mariano and Warekois, who performed an x-ray analysis of HgSe(II) while under pressure. This study was made using a diamond anvil pressure cell giving hexagonal lattice constants  $a=4.32 \text{ \AA}$  and  $c=9.68 \text{ \AA}$ , which are in good agreement with the values  $a=4.32 \text{ \AA}$  and  $c=9.62 \text{ \AA}$ , obtained by Kafalas et al. [119]. The volume change at the transition is approximately 8.6%.

### 20.6. Zinc Selenide

The metallic high-pressure phase of zinc selenide was first reported to occur at 165 kbar [181] indicated by a large drop in electrical resistance. On the ruby (NaCl) fluorescence scale this phase transition occurs at  $137 \pm 3$  kbar on the compression cycle [151].

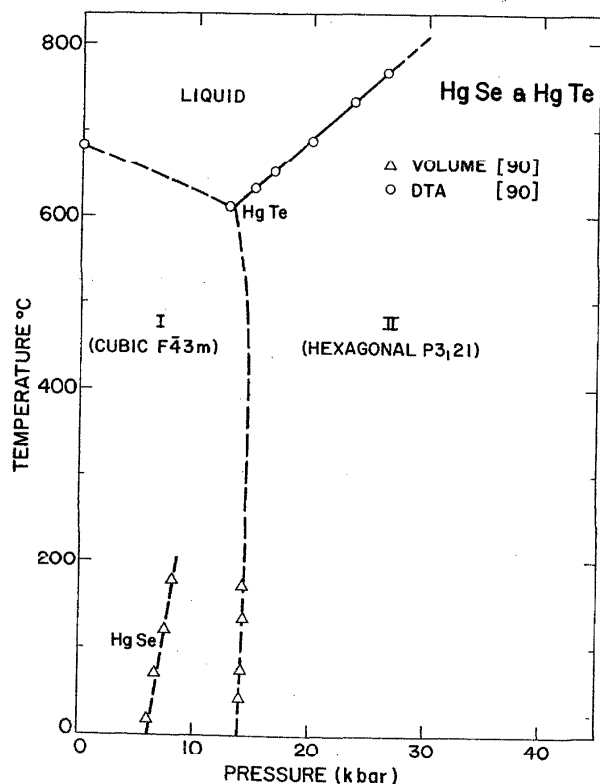


FIGURE 40. Partial phase diagram for mercury selenide and mercury telluride

## 21. Tellurides

### 21.1. Cadmium Telluride

Cadmium telluride crystallizes under normal conditions in the cubic zincblende structure represented by space group  $F43m$ . It has been shown by optical absorption measurements [64], relative volume determination [90], x-ray diffraction [22, 119, 146, 189], and electrical resistance measurements [181], that CdTe undergoes a phase transition from the zincblende to the NaCl structure under a pressure of 30–35 kbar. A second polymorphic transition was reported to occur at approximately 90 kbar on the basis of an abrupt drop of the electrical resistance by several orders of magnitude [181] and x-ray diffraction results [146].

The CdTe(I)-CdTe(II) transition has been published by several different researchers and their transition pressures are listed below:

Pressures of the zincblende to NaCl transition in CdTe

	Pressure (kbar)	Method	Ref.
Onodera	$33.3 \pm 1.8$	el. res.	141
Samara and Drickamer	30	31. res.	181
Jayaraman et al.	33	vol.	90
Cline and Stephens	$31.8 \pm 0.5$	vol.	46
Edwards and Drickamer	35	opt. abs.	64
Owen et al.	30	x-ray diffr.	146
Borg and Smith	32	x-ray diffr.	22
Average	$32.2 \pm 1.8$		

The above average is probably a fair approximation to the equilibrium pressure and agrees well with the work of Jayaraman et al. [90], who took compression and decompression values and corrected for friction. It is also in good agreement with the work of Onodera [141], who determined points along the CdTe(I)-CdTe(II) boundary up to 800 °C. A linear fit to these high temperature points gives  $P=33.3$  kbar at 25 °C.

The melting curve for CdTe was studied by Jayaraman et al. [90] to a maximum pressure of 30 kbar. From a melting point of 1092 °C, the slope of the melting curve is  $-5 \text{ °C/kbar}$  up to the triple point at about 19.2 kbar and 996 °C. The slope of the melting curve above the triple point is about  $10 \text{ °C/kbar}$ . The melting curve was detected by DTA. Temperatures were measured with chrome alumel thermocouples, and melting temperatures were determined to  $\pm 3 \text{ °C}$ . The CdTe(I)-CdTe(II) phase boundary [141] extrapolates to the triple point in the high temperature region.

### 21.2. Europium Telluride

The compression data for europium telluride obtained from high-pressure x-ray-diffraction studies represents a normal compression curve up to 100 kbar, showing decreasing compression with pressure [87]. The discontinuity at 100

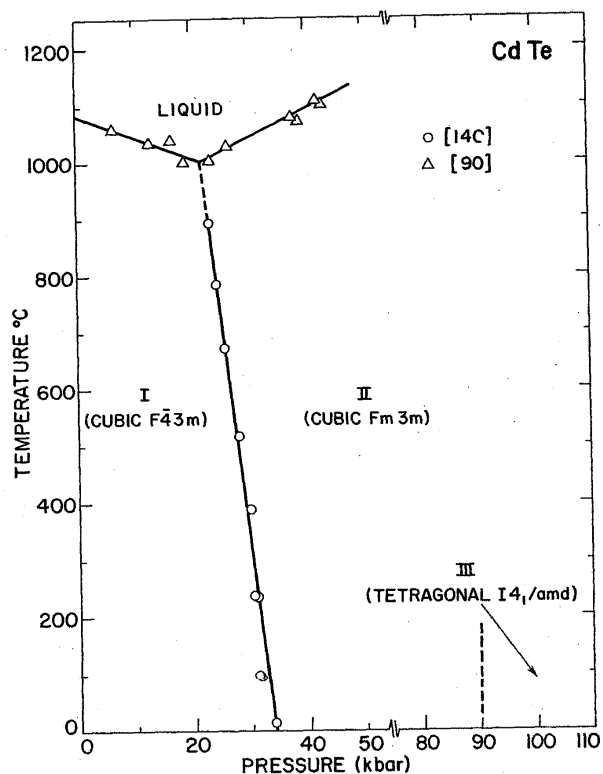


FIGURE 41. Partial phase diagram for cadmium telluride

kbar is due to a phase transition from the NaCl to the CsCl structure. The associated volume decrease in EuTe at this transition is about 16% in contrast to 24% observed in SmTe.

### 21.3. Germanium Telluride

At atmospheric pressure and  $T=400$  °C GeTe undergoes a first-order phase transition from the As-type (A7) to the NaCl-type structure. At room temperature this transition occurs at a pressure of 35 kbar [99]. GeTe and SnTe form a solid-solution series, which, depending upon composition, has either the A7 or NaCl-type structure. At atmospheric pressure, alloys having less than 65% SnTe have the rhombohedral structure, while those in excess of 65% SnTe have the cubic structure [96].

Rooymans [177] also investigated EuTe by high-pressure x-ray-diffraction techniques, and reported a discontinuous isostructural transition at about 10 kbar, which was attributed to a change in the valence state of the europium ion. More recent studies [87, 186] do not substantiate this electronic transition.

### 21.4. Indium Telluride

In the InTe system, a pressure-induced NaCl-type phase exists for the range of composition  $\text{In}_{0.80}\text{Te}$  to  $\text{In}_{1.15}\text{Te}$ . Superconductivity exists for the whole range with the maximum transition temperature occurring for the stoichiometric InTe. The high pressure NaCl-type phase of InTe was first

synthesized by Banus et al. [9], and reported to have electrical conductivity in the metallic range. Initially, InTe was synthesized by the fusion of semiconductor elements at 40–50 kbar and about 1000 °C. It has also been obtained at pressures above 28 kbar and temperature above 150 °C from the stoichiometric tetragonal InTe(I) phase prepared at atmospheric pressure [8]. When samples are cooled to room temperature, the high pressure phase is readily recovered at atmospheric pressure, but slowly transforms to InTe(I). In this transformation, however, an intermediate phase InTe(II) appears, which can be indexed as tetragonal.

Darnel et al. [50] proposed a simple cubic structure for InTe(II) with lattice constant  $a=3.07$  Å and a density of 6.69 g/cm<sup>3</sup>, which was later shown to be in error. Actually, the calculated density should have been 13.8 g/cm<sup>3</sup>. Banus et al. [8] proposed the NaCl-type structure for InTe with a calculated density of 6.92 g/cm<sup>3</sup> and a lattice constant  $a=6.54$  Å. The above density agrees well with measured values of 6.82 g/cm<sup>3</sup>. The superconducting transition temperature was reported to be 3.5 K [74] and not 2.18 K, as previously reported by Bommel et al. [21].

The InTe(I)-InTe(II) phase boundary has been determined by electrical resistance methods in the range of 150 °C–700 °C. The melting curve for InTe(II) has been studied by DTA in the region 18 kbar–40 kbar. It is estimated that the triple point occurs at 718 °C and 11 kbar [12].

In studies of the inversion rate of InTe(II)-InTe(I) at room temperature, a new 'transitory' intermediate phase has been discovered which can be indexed on the basis of a tetragonal cell [184]. Within 60 days, the x-ray powder pattern of

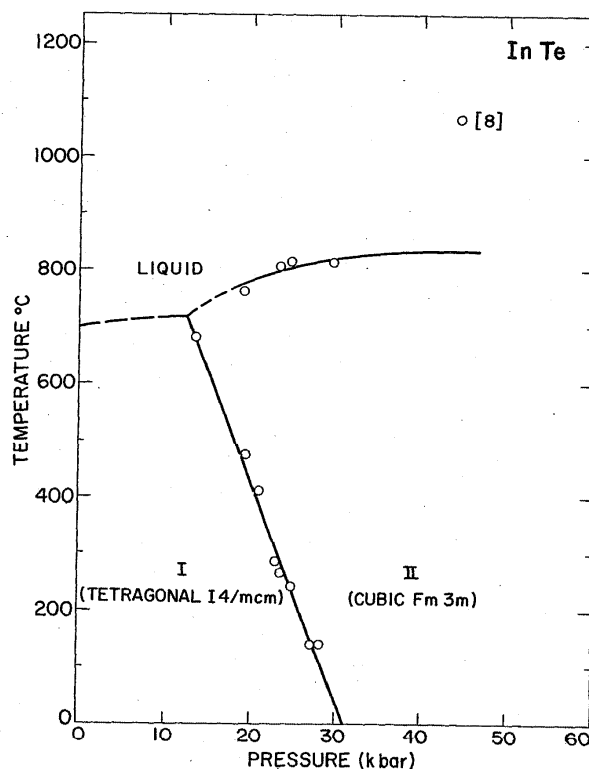


FIGURE 42. Phase diagram for indium telluride.

InTe(II), stored at room temperature, shows a change in which three low angle lines appear that are not correlated to InTe(I). Within 140 days, the InTe(II) has completely transformed to the new phase designated InTe(II').

### 21.5. Lead Telluride

A polymorphic transition in lead telluride has been studied by Bridgman [30, 34, and 36], Samara and Drickamer [180], and Minomura et al. [127]. Bridgman reported the transition to occur at 40.4 kbar with about a 1% volume decrease. Studies of the behavior of the electrical resistance with pressure show an initial rapid drop, followed by a sharp increase by a factor of 6–8 in the region around 50 kbar. The resistance of the high-pressure phase drops by a factor of 10 between 90 and 200 kbar.

Minomura et al. [127] measured the lattice parameters in PbTe up to 90 kbar by x-ray-diffraction techniques. Pressures were determined with a NaCl internal standard, which was scaled to Bridgman's  $P$ - $V$  data. The phase transition occurred near 50 kbar, with approximately a 2% volume change, and appears to be displacive in nature.

### 21.6. Mercury Telluride

The polymorphism of mercury telluride was first studied by Bridgman [34], who reported a volume discontinuity of 8.4% at 12.5 kbar and room temperature. This transition was also studied by Blair and Smith [20], who studied the behavior of electrical resistance vs. pressure. At a pressure of about 15.5 kbar, an abrupt increase in the resistivity was observed. The resistance changed by a factor of  $10^4$ – $10^5$  and was essentially reversible. On the down cycle, the reverse transition occurs at about 11.6 kbar, so the equilibrium value lies somewhere in between. Using volumetric methods, Jayaraman et al. [90] determined four points along the HgTe(I)-HgTe(II) phase boundary from room temperature up to 160 °C. The transition pressure for all four points was 14 kbar, which is an average of the up and downstroke values.

The crystal structure of HgTe(I) is of the zincblende-type, while HgTe(II) has the cinnabar (B9) structure [90]. The lattice constants for HgTe(II) at a pressure of approximately 20 kbar is  $a=4.51$  Å and  $c=10.13$  Å.

The fusion curve for HgTe has been determined by Jayaraman et al. [90] over the pressure interval 0–27 kbar by DTA. The melting studies were carried out using molybdenum and tantalum containers. The DTA signals were of poor quality and the data were taken from the best out of 5 runs. For a normal melting point of 670 °C, the melting slope of the zincblende polymorph is about  $-4.6$  °C/kbar up to the triple point near 615 °C and 12 kbar. The melting slope of the cinnabar phase is about 11.5 °C/kbar up to about 27 kbar.

### 21.7. Praseodymium Telluride

In the case of praseodymium telluride, where the praseodymium ion is in the trivalent state, the NaCl phase has a much smaller compressibility, compared to the NaCl phases of SmTe and EuTe. The compression for PrTe up to 90 kbar is 4.5%, compared to 11–15% for EuTe and SmTe [93, 186].

Praseodymium telluride undergoes a first order transition [186] at about 90 kbar, from the NaCl to the CsCl-type structure. The volume change associated with the transition is 11.5%.

### 21.8. Samarium Telluride

Rooymans has studied samarium telluride by high-pressure x-ray diffraction techniques [168], and reported an isostructural transition which was attributed to a change in the valence state of samarium to the trivalent state. Additional experimental evidence by Jayaraman and co-workers [87, 93] shows that the shape of the compression curve is anomalous in the 30–45 kbar region. In this region, the slope of the compression curve increases with increasing pressure. There is not change in crystal structure up to 110 kbar which suggests that the anomalous compression must involve a contraction of the ionic radius with pressure. The anomalous compression is attributed, therefore, to a change in the valence state with pressure due to a  $4f$ - $5d$  electronic transition. There is a volume discontinuity at 110 kbar, due to a phase transition of the electron collapsed NaCl phase to the CsCl structure.

### 21.9. Tin Telluride

Tin telluride is an  $A^IVB^{VI}$  compound analogous to PbS, PbSe, and PbTe. At atmospheric pressure, these four compounds have a cubic crystal structure of the NaCl-type. The electrical resistance of tin telluride was measured up to 50 kbar, showing a gradual decrease below 18 kbar. At 18 kbar, however, there is a rapid 360% increase in resistance, after which the resistance drops smoothly with increasing pressure [101]. This behavior is completely reversible, suggesting the possibility of a polymorphic transition.

The existence of the transition at 18 kbar was confirmed from x-ray diffraction studies. The x-ray patterns were obtained by using a diamond anvil pressure cell [101] to maintain the sample in its high-pressure phase. Powder patterns at 20 kbar show that tin telluride has an orthorhombic structure (space group  $Pnma$ ), analogous to the structure of the atmospheric-pressure phase of SnS and SnSe [138]. The lattice constants of the high-pressure phase are  $a=11.59$  Å, and  $c=4.48$  Å, corresponding to a calculated density of 7.21 g/cm<sup>3</sup> with four molecules to a unit cell. There is a net increase in density of 7% at the NaCl orthorhombic transition.

The pressure calibration for the electrical resistance trace in this study, was based on the following fixed point values; bismuth I-II-25 kbar; thallium II-III-37 kbar; and barium I-II-59 kbar. It is assumed that the stated pressures in the x-ray examination were estimated, since no mention of internal standards was made.

### 21.10. Ytterbium Telluride

Ytterbium telluride has been studied by x-ray diffraction techniques in the pressure range up to 300 kbars. Up to 150 kbar, the compression curve appears to represent normal behavior. Between 150 and 180 kbar, the volume decrease is anomalous [93 and 186], and is similar to the behavior of

SmTe. The anomalously high compression in YbTe is attributed to a  $4f-5d$  electronic transition. There is no indication of a NaCl to CsCl-type transition up to maximum pressure of the study.

### 21.11. Zinc Telluride

Zinc telluride undergoes a polymorphic transition in the region of 125 kbar [181]. Associated with the transition is a drop in the electrical resistance by a factor of about  $10^5$ . No other pressure studies on ZnTe have been reported.

### References

- [1] Akella, J., Vaidya, S. N., and Kennedy, G. C., *Phys. Rev.*, **185**, 1135-1140 (1969).
- [2] Akella, J., Vaidya, S. N., Kennedy, G. C., *J. Appl. Phys.*, **40**, 2800-2805 (1969).
- [3] Al'tshuler, L. V., Pavlovskii, M. N., Drakin, V. P., *Z. Eksperim. i Teor. Fiz.*, **52**, 400 (1967).
- [4] Archer, R. J., Koyama, R. Y., Loebner, E. E., Lucas, R. C., *Phys. Rev. Lett.*, **12**, 538 (1964).
- [5] Aronsson, B., Stenberg, E., Aselius, J., *J. Acta Chem. Scand.*, **14**, 733 (1960).
- [6] Balchan, A. S., Drickamer, H. G., *Rev. Sci. Instrum.*, **32**, 308-311 (1961).
- [7] Banus, M. D., Hannaman, R. E., Mariano, A. N., *Appl. Phys. Lett.*, **2**, 35 (1963).
- [8] Banus, M. D., Hannaman, R. E., Strong, H. M., Cohen, K., *Science*, **142**, 662-663 (1963).
- [9] Banus, M. D., Kafalas, J. A., Hannaman, R. E., Gatos, H. C., *Solid State Research Report, Lincoln Laboratory, MIT No. 3*, 18 (1962).
- [10] Banus, M. D., Lavine, M. C., *J. Appl. Phys.*, **38**, 2042-2046 (1967).
- [11] Banus, M. D., Lavine, M. C., *J. Appl. Phys.*, **40**, 409-413 (1969).
- [12] Banus, M. D., Robinson, P. M., *J. Appl. Phys.*, **37**, 3771-3774 (1966).
- [13] Barnett, J. D., Block S., Piermarini, G. J., *Rev. Sci. Instrum.*, **44**, 1-9 (1973).
- [14] Bassett, W. A., Takahashi, T., *Amer. Mineral.*, **50**, 1576-1594 (1965).
- [15] Bassett, W. A., Takahashi, T., Mao, H. K., Weaver, J. S., *J. Appl. Phys.*, **39**, 319-325 (1968).
- [16] Bates, C. H., White, W. B., Roy, R., *Science*, **137**, 993 (1962).
- [17] Bijvoet, J. M., and Lely, J. A., *Rec. Trav. Chim.*, **59**, 908 (1940).
- [18] Birch, F., *Rev. Sci. Instrum.*, **10**, 137-140 (1939).
- [19] Birch, F., Robertson, E. E., Clark, S. P., *Ind. Eng. Chem.*, **49**, 1965-1966 (1957).
- [20] Blair, J., Smith, A. C., *Phys. Rev. Lett.*, **7**, 124 (1961).
- [21] Bommel, H. E., Darnell, A. J., Libby, W. F., and Tittmann, B. R., *Science*, **139**, 1301-1302 (1963).
- [22] Borg, I. Y., Smith, D. K., *J. Phys. Chem. Solids*, **28**, 49-53 (1967).
- [23] Borom, M. P., Slack, G. A., and Szymasgek, J. W., *Am Ceram. Soc. Bull.*, **51**, 852 (1972).
- [24] Bradley, R. S., Grace, J. D., and Munro, D. C., *Z. Krist.*, **120**, 349-358 (1964).
- [25] Bradley, R. S., Munro, D. C., and Spencer, P. N., *Faraday Soc. Trans.*, **65**, 1920-1926 (1969).
- [26] Bradley, R. S., Munro, D. C., Spencer, P. N., *Phys. Stat. Sol.*, **36**, K51 (1969).
- [27] Bridgman, P. W., *Am. Acad. Arts Sci.*, **76**, 1-7 (1945).
- [28] Bridgman, P. W., *Phys. Rev.*, **38**, 182-191 (1931).
- [29] Bridgman, P. W., *Phys. Rev.*, **48**, 893-906 (1935).
- [30] Bridgman, P. W., *Phys. Rev.*, **57**, 237-239 (1940).
- [31] Bridgman, P. W., *Proc. Am. Acad. Arts Sci.*, **51**, 55-124 (1915).
- [32] Bridgman, P. W., *Proc. Acad. Arts Sci.*, **72**, 45-136 (1937).
- [33] Bridgman, P. W., *Proc. Acad. Arts Sci.*, **52**, 91-187 (1916).
- [34] Bridgman, P. W., *Proc. Acad. Arts Sci.*, **74**, 21-51 (1940).
- [35] Bridgman, P. W., *Proc. Am. Acad. Arts Sci.*, **76**, 1-7 (1945).
- [36] Bridgman, P. W., *Proc. Am. Acad. Arts Sci.*, **76**, 55-70 (1948).
- [37] Bridgman, P. W., *Z. Krist.*, **67**, 363-376 (1928).
- [38] Bundy, F. P., and Wentorf, R. H., *J. Chem. Phys.*, **38**, 1144-1149 (1963).
- [38a] Bundy, F. P., *Rev. Sci. Instrum.*, **46**, 1318-1324 (1975).
- [39] Burley, G., *J. Phys. Chem.*, **68**, 1111-1114 (1964).
- [40] Calvert, L. D., and Whalley, E., *J. Chem. Phys.*, **53**, 2151-2155 (1970).
- [41] Cannon, J. F., *J. Phys. Chem. Ref. Data*, **3**, 781-824 (1974).
- [42] Cermic, L., and Neuhaus, A., *High Temp.-High Press.*, **4**, 97-99 (1972).
- [43] Chu, C. W., Early, A., Geballe, T. H., Rusakov A., and Schwall, R. E., *J. Phys. C: Solid State Phys.*, **8**, L241-L244 (1975).
- [44] Clark, J. B., and Pistorius, C. W. F. T., *Solid State Commun.*, **7**, 787-789 (1969).
- [45] Clark, S. P., *J. Chem. Phys.*, **31**, 1526-1531 (1959).
- [46] Cline, C. F., and Stephens, D. R., *J. Appl. Phys.*, **36**, 2869-2873 (1965).
- [47] Clougherty, E. V., Lothrop, K. H., and Kafalas, J. A., *Nature*, **191**, 1194-1195 (1961).
- [48] Coree, J. A., *J. Appl. Phys.*, **35**, 3032-3033 (1964).
- [49] Cubicciotti, D., and Eding, H., *J. Chem. Eng. Data*, **10**, 343 (1965).
- [50] Darnell, A. J., Yench, A. J., and Libby, W. F., *Science*, **141**, 713-714 (1963).
- [51] Davis, B. L., and Adams, L. H., *Science*, **146**, 519-521 (1964).
- [52] Deaton, B. C., *J. Appl. Phys.*, **36**, 1500-1501 (1965).
- [53] Decker, D. L., *J. Appl. Phys.*, **42**, 3239-3244 (1971).
- [54] Decker, D. L., *Pure and Appl. Chem.*, **2**, 133-146 (1975).
- [55] Decker, D. L., Bassett, W. A., Merrill, L., Hall, H. T., and Barnett, J. D., *J. Phys. Chem. Ref. Data*, **1**, 773-836 (1972).
- [56] Decker, D. L., Beyerlein, R. A., Roult, G., and Worlton, T. G., *Phys. Rev.* **B10**, 3584-3593 (1974).
- [57] DeVries, R. C., Report No. 72CRD178, Avail. Gen. Electric Co., Schenectady, New York 12305 (1972).
- [58] Donohue, P. C., *Inorg. Chem.*, **9**, 430-432 (1970).
- [59] Donohue, P. C., *Inorg. Chem.*, **9**, 335-337 (1970).
- [60] Donohue, P. C., and Young, H. S., *J. Solid State Chem.*, **1**, 143-149 (1970).
- [61] Donnay, J. D. H., and Ondik, H. M., *Crystal Data Determinative Tables, Third Edition, Vol. II, Inorg. Compounds*, Publ. jointly by U.S. Dept. of Commerce, NBS and Joint Committee on Powder Diffraction Stds. (1973).
- [62] Dremin, A. N., and Brensov, O. N., *Usp. Khim.*, **36**, 898 (1968).
- [63] Drickamer, H. G., *Rev. Sci. Instrum.*, **41**, 1667-1668 (1970).
- [64] Edwards, A. L., and Drickamer, H. G., *Phys. Rev.*, **122**, 1149-1157 (1961).
- [65] Edwards, A. L., Slykhouse, T. E., and Drickamer, H. G., *J. Phys. Chem. Solids*, **11**, 140-148 (1959).
- [66] Elliott, N., and Hastings, J., *Acta Cryst.*, **14**, 1018 (1961).
- [67] Evdokimova, V. V., and Vereshchagin, L. F., *Zh. Eksperim. i Teor. Fiz.*, **43**, 1208-1212 (1962), English Trans., *Sov. Phys. JETP*, **16**, 855-859 (1963).
- [68] Gale, K. A., *J. Phys. Chem. Solids*, **28**, 1233 (1967).
- [69] Garland, C., and Choo, K., *Phys. Rev. B*, **8**, 5143-5152 (1973).
- [70] Garland, C., and Pollina, J., *J. Chem. Phys.*, **58**, 5002-5008 (1973).
- [71] Garland, C., and Enard, R., *J. Chem. Phys.*, **45**, 763-766 (1966).
- [72] Garland, C. W., and Young, R. A., *J. Chem. Phys.*, **49**, 5282-5293 (1968).
- [73] Gebbie, H. A., Smith, P. L., Austin, J. G., and King, J. H., *Nature*, **188**, 1095-1096 (1960).
- [74] Geller, S., Jayaraman, A., and Hull, G. W., *J. Phys. Chem. Solids*, **26**, 353-361 (1965).
- [75] Geller, S., McWhan, D. B., and Hull, G. W., Jr., *Science*, **140**, 3562-3563 (1963).
- [76] Getting, I. C., and Kennedy, G. C., *J. Appl. Phys.*, **41**, 4552-4562 (1970).
- [77] Goodenough, J. B., and Kafalas, J. A., *Phys. Rev.*, **157**, 389-395 (1967).
- [78] Hanneman, R. E., and Strong, H. M., *J. Appl. Phys.*, **37**, 612-614 (1966).
- [79] Haygarth, J. C., Getting, I. C., and Kennedy, G. C., *J. Appl. Phys.*, **38**, 4577-4564 (1967).
- [80] Haygarth, J. C., Luedemann, H. D., Getting, I. C., and Kennedy, G. C., *J. Phys. Chem. Solids*, **30**, 1417-1424 (1969).
- [80a] Homan, C. G., Kendall, D. P., Davidson, T. E., Frankel, J., *Solid State Commun.*, **17**, 831-832 (1975).
- [81] International Committee of Weights and Measures, *The International Practical Temperature Scale of 1968*, *Meteorologia*, **5**, 35-44 (1969).
- [82] Jacobs, R. B., *Phys. Rev.*, **54**, 325-331 (1938).
- [83] Jacobs, R. B., *Phys. Rev.*, **54**, 468-474 (1938).

- [84] Jamieson, J. C., *Physics of Solids at High Pressures*, C. T. Tomiguka and R. M. Eurrie, Eds., (Academic Press Inc., New York, 1965), p. 444 (1965).
- [85] Jamieson, J. C., *Science*, **139**, 845-847 (1963).
- [86] Jamieson, J. C., Halleck, P. M., Roof, R. B., and Pistorius, C. W. F. T., *J. Phys. Chem. Solids*, **36**, 939-944 (1975).
- [87] Jayaraman, A., *Ind. J. Pure Appl. Phys.*, **9**, 983-985 (1971).
- [88] Jayaraman, A., *Phys. Rev. Lett.*, **29**, 1674-1676 (1972).
- [89] Jayaraman, A., Butcher, E., Dermier, P. D., and Longinotti, L. D., *Phys. Rev. Lett.*, **31**, 700-703 (1973).
- [90] Jayaraman, A., Klement, W., and Kennedy, G. C., *Phys. Rev.*, **130**, 2277-2283 (1963).
- [91] Jayaraman, A., Narayanamurti, V., Bucher, E., and Maines, R. G., *Phys. Rev. Lett.*, **25**, 1430 (1970).
- [92] Jayaraman, A., Newton, R. C., and Kennedy, G. C., *Nature*, **191**, 1288-1290 (1961).
- [93] Jayaraman, A., Singh, A. K., and Chatterjee, A., *Proc. of the 9th Rare Earth Research Conf.*, Vol. I (1971).
- [94] Johnson, D. P., and Heydemann, P. L. M., *Rev. Sci. Instrum.*, **38**, 1294-1300 (1967).
- [95] Johnson, Q., *Science*, **53**, 419-420 (1966).
- [96] Kabalkina, S. S., Serebryanaya, N. R., and Vereshchagin, L. F., *Sov. Phys., Solid State*, **9**, 2527-2529 (1968).
- [97] Kabalkina, S. S., Shcherbakov, M. O., and Vereshchagin, L. F., *Sov. Phys. Dokl.*, **15**, 751-754 (1971).
- [98] Kabalkina, S. S., and Troitskaya, Z. V., *Sov. Phys. Dokl.*, **8**, 800-802 (1964).
- [99] Kabalkina, S. S., Vereshchagin, L. F., and Serebryanaya, N. R., *Sov. Phys. JETP*, **24**, 917-919 (1967).
- [100] Kafalas, J. A., Gatos, H. C., Lavine, M. C., and Banus, M. D., *J. Phys. Chem. Solids*, **23**, 1541-1544 (1962).
- [101] Kafalas, J. A., and Mariano, A. N., *Science*, **143**, 952 (1964).
- [102] Kaminskii, E. Z., Omel'chenko, A. V., and Estron, E. I., *Sov. Phys. Solid State*, **12**, 2697-2698 (1971).
- [103] Kasper, J. S., and Brandhorst, H., *J. Chem. Phys.*, **41**, 3768-3772 (1964).
- [104] Katsura, T., Iwasaki, B., and Kimura, S., *J. Chem. Phys.*, **47**, 4559-4560 (1967).
- [105] Katz, G., Kohn, J. A., and Broder, J. C., *Acta Cryst.*, **10**, 607 (1957).
- [106] Katz, G., and Broder, J. A., *Acta Cryst.*, **10**, 607 (1957).
- [107] Kelley, K., U. S. Bureau of Mines Bull., **393**, 166 (1936).
- [108] Kennedy, G. C., and La Mori, P. N., *J. Geophys. Res.*, **67**, 851-856 (1962).
- [109] Kabayashi, T., Susa, K., and Taniguchi, S., *Mat. Res. Bull.*, **9**, 625-632 (1974).
- [110] Konyaev, Yu. S., *Prikl. Tekh. Eksp.*, 1961, 107-9 (1961), English translation, *Instrum. Exp. Tech. (USSR)*, **1961**, 728-731 (1961).
- [111] Kullerud, C., Bell, P. M., and England, J. L., *Carnegie Inst. Washington Yearbook*, **64**, 197 (1965).
- [112] Kuriakose, A. K., and Whalley, E., *J. Chem. Phys.*, **48**, 2025-2031 (1968).
- [113] Larson, D. B., Keeler, R. N., Kusubov, A., and Hord, B. L., *J. Phys. Chem. Solids*, **27**, 476-478 (1966).
- [114] Liu, L., *J. Appl. Phys.*, **42**, 3702-3704 (1971).
- [115] Liu, L., and Bassett, W. A., *J. Appl. Phys.*, **44**, 1475-1479 (1973).
- [116] Liu, L., and Bassett, W. A., *J. Geophys. Res.*, **77**, 4934-4937 (1972).
- [117] Liu, L., and Bassett, W. A., *J. Geophys. Res.*, **78**, 8470-8473 (1973).
- [117a] Loree, T. R., Fowler, C. M., Zukas, E. G., Minshall, F. S., *J. Appl. Phys.*, **37**, 1918-1927 (1966).
- [118] Mariano, A. N., and Chopra, K. L., *Appl. Phys. Lett.*, **10**, 282-284 (1967).
- [119] Mariano, A. N., and Warekois, E. P., *Science*, **142**, 672-673 (1963).
- [120] Masaki, K., Sawamoto, H., Ohtami, E., Kumazawa, M., Machida, M., Mizukusa, S., and Nakayama, N., *Rev. Sci. Instrum.*, **46**, 84-88 (1975).
- [121] McWhan, D. B., and Marezio, M., *J. Chem. Phys.*, **45**, 2508-2511 (1966).
- [122] McWhan, D. B., Marezio, M., Remeika, J. P., and Dernier, P. D., *Phys. Rev. B*, **5**, 2552-2555 (1972).
- [123] Meisalo, V., and Kalliomaki, M., *High Temp.-High Pressures*, **5**, 663-673 (1973).
- [124] Meisalo, V., and Kalliomaki, M., *Phys. Stat. Sol. A*, **7**, K95-K97 (1971).
- [125] Messer, C. E., and Stiegler, W. T., *J. Am. Chem. Soc.*, **63**, 2703 (1941).
- [126] Minomura, S., and H. G., Drickamer, J., *Phys. Chem. Solids*, **23**, 451-456 (1962).
- [127] Minomura, S., Nagasaki, H., and Wakabayashi, I., *Symp. on the Accurate Characterization of the High-Pressure Environment*, Oct. 14-18 (1968), U.S. Dept. of Commerce, Nat'l. Bureau of Stand., Gaithersburg, Md., E. C. Lloyd ed., NBS Spec. Publ., **326**, 159 (1971).
- [128] Minomura, S., Samara, G. A., and Drickamer, H. G., *J. Appl. Phys.*, **33**, 3196-3197 (1962).
- [129] Miyake, S., Hoshino, S., and Takenaka, T., *J. Phys. Soc. Japan*, **7**, 19 (1951).
- [130] Montgomery, P. W., ASME Paper #64-WA/PT-18 (1964).
- [131] Moore, M. J., and Kasper, J. S., *J. Chem. Phys.*, **48**, 2446-2450 (1968).
- [132] Moore, M. J., Kasper, J. S., and Bundy, F. P., *J. Solid State Chem.*, **1**, 170-172 (1970).
- [133] Morosin, B., and Schirber, J. E., *J. Chem. Phys.*, **42**, 1389-1390 (1965).
- [134] Nabar, M. A., Calvert, L. D., and Whalley, E., *J. Chem. Phys.*, **51**, 1353-1356 (1969).
- [135] Nagasaki, Hiroshi, and Minomura, Shigeru, *J. Phys. Soc. Japan*, **19**, 1496-1497 (1964).
- [136] Narita, K., Watanabe, H., and Wada, M., *Japan. J. Appl. Phys.*, **9**, 1278 (1970).
- [137] Neuhaus, Von A., and Hintze, E., *Ber. Bunsengesellschaft*, **70**, 1073-1080 (1966).
- [138] Okazaki, A., and Ueda, I., *J. Phys. Soc. Japan*, **11**, 470 (1956).
- [139] Omel'chenko, A. V., and Estrin, E. I., *Sov. Phys. Solid State*, **12**, 2746-2747 (1971).
- [140] Onodera, A., *Rev. Phys. Chem. Jpn.*, **39**, 65-77 (1969).
- [141] Onodera, A., *Rev. Phys. Chem. Jpn.*, **39**, 78-92 (1969).
- [142] Onodera, A., Kawai, N., Ishizaki, K., and Spain, I. L., *Solid State Commun.*, **14**, 803-806 (1974).
- [143] Osugi, J., Namikawa, R., and Tanaka, Y., *Nippon Kagaku Zasshi*, **87**, 1169-1173 (1966).
- [144] Osugi, J., Namikawa, R., and Tanaka, Y., *Rev. Phys. Chem. Jpn.*, **37**, 81 (1967).
- [145] Osugi, J., Shimizu, K., and Tanaka, Y., *Nippon Kagaku Zasshi*, 1032-1035 (1966).
- [146] Owen, N. B., Smith, P. L., Martin, J. E., and Wright, A. J., *J. Phys. Chem. Solids*, **24**, 1519-1524 (1963).
- [147] Perri, J. A., LaPlaca, S., and Post, B., *Acta Cryst.*, **11**, 310 (1958).
- [148] Petrunina, T. I., and Estrin, E. I., *Sov. Phys. Dokl.*, **13**, 1243-1245 (1969).
- [149] Piermarini, G. J., and Weir, C. E., *J. Chem. Phys.*, **37**, 1887-1888 (1962).
- [150] Piermarini, G. J., and Weir, C. E., *J. Res. Nat. Bur. Stand.*, **66A**, 325-331 (1964).
- [151] Piermarini, G. J., and Block, S., *Rev. Sci. Instrum.*, **46**, 973-979 (1975).
- [152] Piermarini, G. J., Block, S., Barnett, J. D., and Formau, R. A., *J. Appl. Phys.*, **46**, 2774-2780 (1975).
- [153] Pistorius, C. W. F. T., *J. Chem. Phys.*, **43**, 1557-1562 (1965).
- [154] Pistorius, C. W. F. T., *J. Chem. Phys.*, **45**, 3513-3519 (1966).
- [155] Pistorius, C. W. F. T., *J. Chem. Phys.*, **50**, 1436-1442 (1969).
- [156] Pistorius, C. W. F. T., *J. Inorg. Nucl. Chem.*, **19**, 367-370 (1961).
- [157] Pistorius, C. W. F. T., *J. Phys. Chem. Solids*, **25**, 1477-1481 (1964).
- [158] Pistorius, C. W. F. T., *J. Phys. Chem. Solids*, **26**, 1543-1548 (1965).
- [159] Pistorius, C. W. F. T., *J. Phys. Chem. Solids*, **26**, 1003-1011 (1965).
- [160] Pistorius, C. W. F. T., *J. Phys. Chem. Solids*, **32**, 2761-2763 (1971).
- [161] Pistorius, C. W. F. T., *Nature*, **204**, 467-468 (1964).
- [162] Pistorius, C. W. F. T., *Z. Phys. Chem. Neue Folge*, **65**, 51-61 (1969).
- [163] Pistorius, C. W. F. T., and Admiraal, L. J., *Nature*, **201**, 1321 (1964).
- [164] Pistorius, C. W. F. T., and Boeyens, J. C. A., *J. Chem. Phys.*, **48**, 1018-1022 (1968).
- [165] Pistorius, C. W. F. T., and Clark, J. B., *Phys. Rev.*, **173**, 692-699 (1968).
- [166] Pistorius, C. W. F. T., Clark, J. B., and Rapoport, Eliezer, *J. Chem. Phys.*, **48**, 5123-5131 (1968).
- [167] Pistorius, C. W. F. T., and Snyman, Hendrik C., *Z. Physik. Chemie Neue Folge*, **43**, 1-10 (1964).
- [168] Popova, S. V., and Boiko, L. G., *High Temp.-High Pressures*, **3**, 238-239 (1971).

- [169] Price, D. L., Rowe, J. M., Rush, J. J., Price, E., Hinks, D. G., and Susman, S., *J. Chem. Phys.*, **56**, 3697-3702 (1972).
- [170] Rapoport, E., and Pistorius, C. W. F. T., *Phys. Rev.*, **172**, 838-847 (1968).
- [171] Richter, P. W., and Pistorius, C. W. F. T., *Acta Cryst.*, **B28**, 3105 (1972).
- [172] Richter, P. W., and Pistorius, C. W. F. T., *J. Chem. Phys.*, **54**, 5436-5437 (1971).
- [173] Robie, R. A., and Waldbaum, D. R., *U. S. Geol. Survey Bull.*, 1259 (1968).
- [174] Rooymans, C. J. M., *Ber. Bunsenges Phys. Chem.*, **70**, 1036-1041 (1966).
- [175] Rooymans, C. J. M., *J. Inorg. Nucl. Chem.*, **25**, 253-155 (1963).
- [176] Rooymans, C. J. M., *Phys. Lett.*, **4**, 186-187 (1963).
- [177] Rooymans, C. J. M., *Solid State Commun.*, **3**, 421-424 (1965).
- [178] Ruggleman, B. M., and Drickamer, H. G., *J. Chem. Phys.*, **38**, 2721-2724 (1963).
- [179] Samara, G. A., *Phys. Rev.*, **165**, 959-969 (1968).
- [180] Samara, G. A., and Drickamer, H. G., *J. Chem. Phys.*, **37**, 1159-1160 (1962).
- [181] Samara, G. A., and Drickamer, H. G., *J. Phys. Chem. Solids*, **23**, 457-461 (1962).
- [182] Samara, G. A., Walters, L. C., and Northrop, D. A., *J. Phys. Chem. Solids*, **28**, 1875-1883 (1967).
- [183] Schock, R. N., and Jamieson, J. C. J. *Phys. Chem. Solids*, **30**, 1527-5133 (1969).
- [184] Sclar, C. B., Carrison, L. C., and Schwartz, C. M., *Science*, **147**, 1569-1571 (1965).
- [185] Sense, K. A., *U. S. Atomic Energy Comm., Batelle Mem. Inst.*, **1199** (1957).
- [186] Singh, A. K., Jayaraman, A., and Chatterjee, A., *Solid State Commun.*, **9**, 1459 (1971).
- [187] Slater, J. C., *Phys. Rev.*, **23**, 488 (1924).
- [188] Smith, P. L., and Martin, J. E., *Nature*, **196**, 762-763 (1962).
- [189] Smith, P. L., and Martin, J. E., *Phys. Lett.*, **6**, 42 (1963).
- [190] Sparks, J. T., and Komoto, T., *J. Appl. Phys.*, **38**, 715 (1968).
- [191] Sparks, J. T., and Komoto, T., *Rev. Mod. Phys.*, **40**, 752 (1968).
- [192] Stevenson, Richard, *J. Chem. Phys.*, **34**, 346-347 (1961).
- [193] Stevenson, R., *J. Chem. Phys.*, **34**, 1757-1762 (1961).
- [194] Strock, L. W., *Z. Physik. Chem.*, **25**, 441-459 (1934).
- [195] Suga, Hiroshi, Matsuo, Takasuke, and Seki, Syuzo, *Bull. Chem. Soc. Japan*, **38**, 1115-1124 (1965).
- [196] Swenson, C. W., and Tredeschi, J. R., *J. Chem. Phys.*, **40**, 1141-1143 (1964).
- [197] Taylor, L. A., *Carnegie Inst. Washington Yearbook*, **68**, 259 (1970).
- [198] Taylor, L. A., and Mao, H. K., *Science*, **170**, 850-851 (1970).
- [199] Vaidya, S. N., and Kennedy, G. C., *J. Phys. Chem. Solids*, **32**, 951-964 (1971).
- [200] Van Valkenburg, A., *J. Res. Nat. Bur. Std.*, **68A**, 97-103 (1964).
- [201] Van Vechten, J. A., *Phys. Rev.*, **B7**, 1479-1507 (1973).
- [202] Vezzoli, G. C., *Materials Res. Bull.*, **6**, 1201-1204 (1971).
- [203] Weinstein, B. A., and Piermarini, G. J., *Phys. Lett.*, **48A**, 14-16 (1974).
- [204] Vereshchagin, L. F., Kabalkina, S. S., and Lityagina, L. M., *Sov. Phys. Dokl.*, **10**, 622-624 (1966).
- [205] Weir, C. E., and Piermarini, G. J., *J. Res. Nat. Bur. Stds.*, **68A**, 105-111 (1964).
- [206] Wentorf, R. H., *J. Chem. Phys.*, **26**, 956 (1957).
- [207] Wentorf, R. H., *J. Chem. Phys.*, **34**, 809-812 (1961).
- [208] Whitney, E. D., and Giesse, R. F., *Nature*, **197**, 1298-1294 (1963).
- [209] Williams, F. V., and Reuhrwein, R. A., *J. Am. Ceram. Soc.*, **82**, 1330 (1960).
- [210] Wyckoff, R. W. G., *Crystal Structures*, 2nd Ed., Vol. 1, 469 pp. Interscience, NY, (1963).
- [210a] Yagi, T., Akimoto, S., *J. Appl. Phys.*, **47**, 3350-4 (1976).
- [211] Yang, W., Schwartz, L. H., and LaMori, P. N., *J. Phys. Chem. Solide*, **29**, 1633-1639 (1968).